Università Degli Studi di Milano-Bicocca

Facoltá di Scienze Matematiche, Fisiche e Naturali

Doctorate in Materials Science

Organic semiconductor rubrene: crystal chemistry of derivatives and high-pressure polymorphism

PhD thesis of:

Stefano Bergantin

Supervisor:

Prof. Massimo Moret

Dean of the Doctorate:

Prof. Gianpaolo Brivio

---

14 January 2014

XXVI Cycle (2010/2013)

Acknowledgements

The research work described in this PhD thesis has been carried out with the contribution of a lot of people. I here would like to gratefully acknowledge them all: Prof. A. Gavezzotti, Prof. M. Moret, Prof. A. Papagni, Prof. A. Sassella, Dr. M. Campione, Dr. F. Fabbiani, Dr. E. Fumagalli, Dr. L. Miozzo, Dr. M. Parravicini, Dr. L. Raimondo, Dr. S. Rizzato, Dr. R. Ruffo, Dr. S. Uttiya, R. Granero-Garcia, A. Gregori, S. Saouane, F. Tosi.

Contents

List of Tables

Acronyms

C-AFM: *Conductive Atomic Force Microscopy.* A variation of atomic force microscopy which uses electrical current to construct the surface profile of the studied sample enabling to correlate spatial features on the sample with its conductivity.

CSD: *Cambridge Structural Database.* A repository for small molecule crystal structures containing more than 600000 structures.

DAC: *Diamond Anvil Cell.* A device used to apply elevated pressure to sub-millimeter sized samples.

DPA: *9,10-diphenylantracene.* A polycyclic aromatic hydrocarbon, used in OLEDs as organic semiconductor.

EoS: *Equation of State.* Within this context, a relationship between the volume of a body and the pressure to which it is subjected.

FP: *Fingerprint Plot.* A 2D plot obtained through the Hirshfeld Surface Analysis, describing intermolecular contacts whithin a crystal structure.

HOMO: *Highest Occupied Molecular Orbital.* For an organic semiconductor, it represents the equivalent of the valence band maximum in an inorganic semiconductor.

HP: *High Pressure.* Experimental conditions realized when the pressure is more than 1 atm.

HS: *Hirshfeld Surface.* A 3D surface enveloping each molecule in a crystal, constructed by partitioning the crystal space into regions of electron distribution of a sum of spherical atoms of the molecule.

LUMO: *Lowest Unoccupied Molecular Orbital.* For an organic semiconductor, it represents the equivalent of the conduction band minimum in an inorganic semiconductor.

PAHs: *Polyciclic Aromatic Hydrocarbons.* Class of organic compounds made of fused aromatic rings, not contain heteroatoms or carrying substituents.

PVT: *Physical Vapor Transport.* Crystal growth technique based on the sublimation of a powdered sample ((either in vacuum or in the presence of an inert gas) and migration of its vapors to a cooler portion of the growth tube.

XRD: *X-Ray Diffraction.* A non-destructive analytical technique which reveal information about the crystal structure, chemical composition, and physical properties of materials and thin films.

Introduction

Electronic devices based on organic molecules, displaying interesting semiconducting properties, have recently become commercially available after being widely studied for more than twenty years. What in the beginning was just an innovative and interesting scientific topic for different research teams all over the world, is nowadays a concrete and commercial working field for many industries and factories. Research in this area gradually moved from the early effort of applying first generation materials to the development of basic working devices, as for example thin film transistors (TFTs) (1–3) or radio frequency identification tags (RF-IDs) (4), to the latest achievement concerning the performance improvement of light emitting diodes (5–8), sensors (9), photovoltaic cells (10–12) and solid state lasers (13), all of them based on organic compounds. The growing importance of organic electronics arises from the possibility to combine the common features of traditional semiconductors, to those of the organic compounds: charge transport and visible-light emission can be obtained with the low-cost processing techniques typical of the plastics industry, with the additional chance to tune the electronic properties of the material by tailoring the molecular structure of the active organic substrate. Crystalline silicon performance is still far from reach by organic counterparts and, on the level of pure semiconducting properties, organic semiconductors will probably be never competitive with traditional semiconductors. Their mechanical properties, nevertheless, definitely allow the use of electronic technologies to a wider range of new possible applications: the concrete possibility to integrate electronics within flexible substrates like plastic, paper and even cloth, constitutes a real technological leap.

A typical organic semiconductor can either be a polymer or a small molecular weight compound, with the capability to delocalize its electronic charge along the molecular structure, thanks to the overlap of π orbitals of adjacent molecules. The focus of this work is on this kind of small molecule organic semiconductors. Indeed, despite the

fact that most organic molecular solids behave like insulating materials, crystals formed by conjugated molecules can show a semiconducting behavior: their charge transport properties can then be evaluated through the mobility μ of the charge carriers involved in the transport process, appearing in the equation for the current density $\mathbf{j}$:

$$\mathbf{j} = -en\mu\mathbf{E} \tag{1}$$

where e is the electron charge, n is the volume density of charge carriers and $\mathbf{E}$ is the electric field. The mobility also depends on the electron charge e, on the charge carrier relaxation time τ and on their mass m, as can be seen in the equation:

$$\mu = -\frac{e\tau}{m} \tag{2}$$

In general, the mechanism behind charge carrier transport in organic semiconductors depends on the quality of the crystal and on its purity, as well as on the intermolecular interactions that define the degree of anisotropy inside it. The *band-like* transport is the typical mechanism of classic inorganic semiconductors and needs a highly ordered and pure crystal to occur, impurities or defects reducing the mobility of charge carriers in the same way as the scattering due to thermal phonons; for this reason, in this case the mobility of charge carriers is inversely proportional to temperature. A second mechanism involves the discontinuous *hopping* of charge carriers from one molecular site to another and is therefore promoted by thermal energy, that is, high temperatures. This process is typical of materials with a highly disordered lattice or containing a high level of impurities and defects, and usually leads to mobility values which are in the 10^{-3} cm^2/Vs range; on the contrary, the charge carrier mobility of *band-like* materials can reach values of tens of cm^2/Vs. In the case of conjugate molecules molecular crystals the charge transport is mainly due to electrons in π orbitals, and this is the main reason for considering crystals of conjugated molecules the most promising materials for organic electronics.

In this field, the molecular class that attracted considerable interest in the last years is represented by polycyclic aromatic hydrocarbons (PAHs)(14); these compounds owe their semiconducting properties to the large conjugated system that constitutes the aromatic core of each single molecule and, in addition, to their particular arrangement in the solid state, realizing a favorable superposition of molecular orbitals. Among

these organic compounds, single crystals of the derivative of tetracene known as rubrene (5,6,11,12-tetraphenyltetracene) have been reported to exhibit, in its orthorhombic crystalline form, the highest charge carrier mobility values among organic semiconductors, up to ~ 40 cm^2/Vs, and comparable to that of amorphous silicon (15, 16). Like most organic semiconductors rubrene is a p-type semiconductor and the reported high mobility values for rubrene refers to hole transport, while electron mobility is smaller by several orders of magnitude. An extremely high photoconductivity has also been measured in rubrene single crystals (17), which can be easily prepared by sublimation methods with a size up to few centimeters (18); on the contrary, the growth of crystalline thin films retaining the same structure of single crystals is really a difficult task (19–21). Despite its interesting semiconducting properties, rubrene shows a low solubility in common organic solvents; moreover, the use of solution techniques for the deposition of thin films or for growth of single crystals is discouraged by the reactivity of rubrene towards molecular oxygen in the presence of light, giving the corresponding endoperoxide and hence hampering its final application for the development of semiconductor devices (22, 23). In the last few years, several synthetic efforts have been directed towards addressing these problems (24–28) and many research teams tried to chemically modify the structure of the original molecule of rubrene, in order to obtain novel derivatives showing improved stability and solubility but unaltered semiconducting properties. The majority of the resulting derivatives exhibit a twisting of the aromatic tetracene core in the solid state, with a consequent negative effect on the charge transport properties. Without a full understanding of the interplay of intermolecular interactions in the solid state, the occurrence of this kind of distortion is unpredictable, as in general it is impossible to predict at the synthetic stage, which crystal structure one derivative will adopt. This means that once a derivative is designed and synthesized, a comparison between the arrangement of the new molecules inside the crystal and the packing motif of the original one is of primary importance to understand the appropriate modifications that must be made to the synthesis, in order to obtain a material whose crystal structure is as similar as possible to the desired one.

The aim of the experimental work described in this thesis has been to relate chemical and electronic properties of rubrene derivatives to their crystal structure, using a crystal engineering approach to design novel molecules with desired features, in order to extend

our knowledge of the charge transport phenomena which are the basis of the interesting properties of rubrene.

In Chapter 1 a general description of rubrene physical and chemical properties is given, focusing on its polymorphism, crystal structure features and main open problems related to this material.

Starting from those rubrene derivatives whose crystal structure has been deposited at the Cambridge Structural Database (CSD), Hirshfeld surface analysis is presented in Chapter 2 as a useful tool which can be used to compare in an objective way the crystal structures of different derivatives, and to evaluate the degree of similarity among them. This tool has been pivotal for the design of the new derivatives further presented in this work. The experimental techniques used for preparation and characterization of the samples studied in the following Chapters are described in Chapter 3.

Chapter 4 is devoted to present a number of new rubrene derivatives, properly tailored and synthesized in order to mimic the crystal structure of orthorhombic rubrene while potentially displaying different chemical and electronic properties, due to the electron withdrawing or donating character of the substituent groups inserted in the molecular structure at the synthetic stage. Single-crystal growth conditions and X-ray diffraction data are discussed, confirming the achieved result of obtaining a selection of derivatives that in the solid state are isostructural among them and also with orthorhombic rubrene. With this series of novel derivatives available, it was finally possible to investigate the properties of the materials while separating the contribution of the crystal packing motif from that of the chemical features of each single molecule.

Aiming at the achievement of a deeper understanding of the interplay of intermolecular interactions inside crystalline rubrene, the application of high pressure on single-crystal samples of different polymorphs of rubrene is described and discussed in Chapter 5. Changes in their intermolecular contacts and in their crystal packing were monitored as a function of the applied pressure and a single-crystal to single-crystal reversible transition was identified between 6.0 and 7.2 GPa for the triclinic polymorph; this new phase was investigated from a crystallographic point of view, with a particular attention to the energetic contribution of short molecular contacts to the packing energy of the crystal, calculated by means of the Coulomb - London - Pauli (CLP) model of intermolecular interaction (29).

In the last Chapter, a short summary of the results presented in this thesis is given, together with a presentation of the future perspectives of this work.

1 | Rubrene

1.1 Chemical and Physical Properties

Rubrene (5,6,11,12-tetraphenyltetracene) has been known since the beginning of the last century (30) and it is considered a classic example of a material with excellent electroluminescence and chemiluminescence properties since the 1960s (31). As a derivative of tetracene, it belongs to the polyciclic aromatic hydrocarbons class of organic compounds, sharing with these systems some of their chemical and electronical characteristics, while standing out from them by displaying some peculiar properties. The

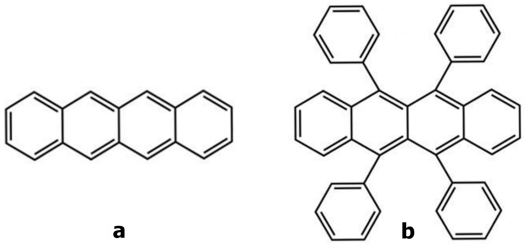

Figure 1.1: Chemical structure of **a**) tetracene and **b**) rubrene.

backbone of the molecule consists of the four linearly fused benzene rings of tetracene (see Figure 1.1); in rubrene, each hydrogen atom of the inner rings has been substituted with an additional phenyl group, which is protruding from the side of the aromatic core almost orthogonally to it. Like many other PAHs, the solubility of this compound in common organic solvents is low: the use of aromatic or halogenated solvents only permits to dissolve few mg/ml of rubrene at room temperature and not even twice the same amount at 60°C (32); in addition, and especially when in solution, rubrene is highly reactive towards molecular oxygen and even the simple exposition to air leads to the formation for the corresponding endoperoxide. This process, which is strongly

enhanced by the presence of light, involves the bonding of an oxygen molecule to one of the inner benzene rings, with the formation of an endoperoxide bridge-bond and the resulting loss of planarity and delocalization of the tetracene core. The optical properties of the molecule are strongly affected by the oxidation: the loss of aromaticity is visually evident from the change in the color of the solution that turns completely colorless from its initial bright reddish color.

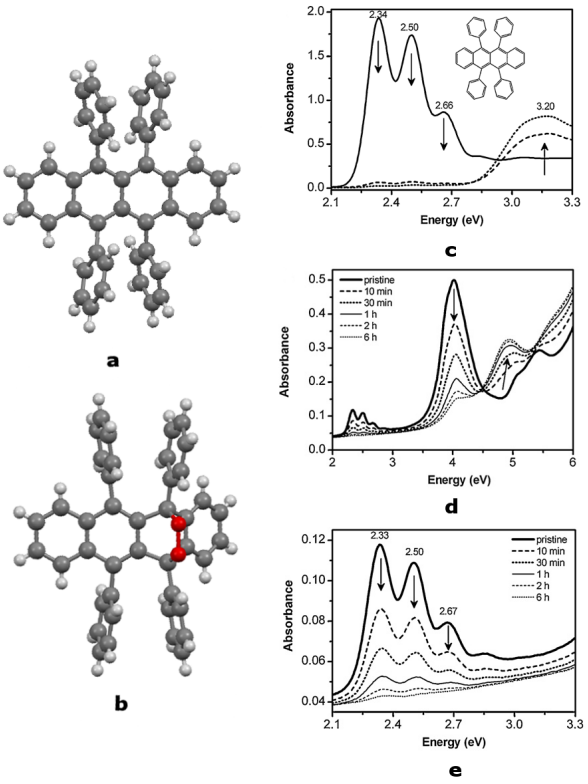

Figure 1.2: Molecular ball-and-stick model of **a**) rubrene and **b**) rubrene endoperoxide; absorption spectra of **c**) a rubrene solution, collected immediately after preparation (solid line), after 20 min (dashed line) and after 40 min (dotted line); a 10 nm thick rubrene film in the **d**) full and **e**) limited spectral range. Exposure time is indicated in figure, from (33).

In the absorption spectrum, shown in Figure 1.2 together with the molecular model of a rubrene molecule and the corresponding endoperoxide, the multiple peaks between 2.3 and 2.7 eV associated with the π-conjugated fused rings of the molecule quickly vanish during the oxidation process, while a new broad absorption band appears around 3.3 eV (33); a similar effect is visible also on the absorption spectra of rubrene thin films exposed to air, reported in figure both for the full spectral range and for an expanded

range. In this case, the absorption band of the endoperoxide appears at higher energy values, close to 5 eV.

1.2 Polymorphism

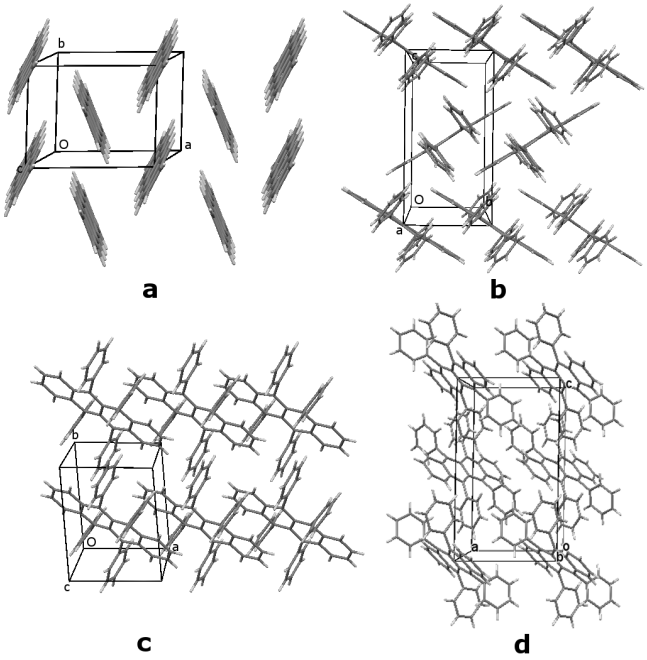

Figure 1.3: Crystal packing of **a**) tetracene and of the **b**) orthorhombic, **c**) triclinic and **d**) monoclinic polymorph of rubrene. Only the layer of molecules closer to the observer is displayed for clarity

Three polymorphs of rubrene are currently reported in the literature, displaying slightly different densities, as reported in Table 1.1, but showing very different features from the point of view of the packing motif inside the crystal (see Figure 1.3):

- in the orthorhombic polymorph (space group *Cmca*) the molecules are arranged in a *herringbone* motif in the (200) layer, with π-stacking in the lattice b direction, while the tetracene cores are planar and perfectly facing each other; along the a direction, instead, the piling scheme can be seen as if every layer were displaced from the previous one, by half a cell parameter either in the b or c direction. With a unit-cell volume of 2756.08 Å^3 and four molecules occupying it (Z), the

Table 1.1: Unit-cell parameters and crystal data for of the three polymorphs of rubrene

Rubrene polymorph	Orthorhombic	Triclinic	Monoclinic
Space group	*Cmca*	$P\bar{1}$	$P2_1/c$
CSD code	QQQCIG07	QQQCIG14	QQQCIG13
T/K	175	173	173
a/Å	26.828(4)	7.0196(4)	8.7397(17)
b/Å	7.1810(10)	8.4532(17)	10.125(2)
c/Å	14.306(2)	11.948(2)	15.635(3)
α/°	90	93.04(3)	90
β/°	90	105.58(3)	90.98(3)
γ/°	90	96.28(3)	90
Volume/Å^3	2756.08	683.50	1383.33
V_{mol}/Å^3	689.02	683.50	691.67
Density/g cm^{-3}	1.284	1.294	1.279
Z	4	1	2
Z'	0.25	0.5	0.5

molecular volume is 689.02 Å^3 and there is only a quarter of a molecule in the asymmetric unit (Z').

- in the packing motif of the triclinic polymorph (space group $P\bar{1}$), the π-stacking of the tetracene cores is occurring in the a direction and is almost unaltered when compared to the orthorhombic polymorph, apart from a small displacement of the aromatic cores towards their short axes, and their non orthogonality with respect to the (001) layer; the *herringbone* arrangement of the molecules, on the contrary, is absent and neither is present the alternate-layer piling scheme. There is now only one molecule in the unit with a molecular volume of 683.50 Å^3, but there is only half a molecule in the asymmetric unit.

- the monoclinic polymorph (space group $P2_1/c$) does not show any π-stacking features at all. There are two molecules in the unit cell, each of them sharing half of the 1383.33 Å^3 unit-cell volume and the asymmetric unit is based on half a molecule.

Single crystals of both the monoclinic and the triclinic polymorph need the use of solution methods to be produced (34), while the growth of single crystals of the orthorhombic

polymorph even with sizes up to centimeters can be quite easily obtained by means of physical vapor transport or by sublimation in vacuum condition: a detailed structural study of orthorhombic rubrene crystals grown by vapor transport was carried out by Jurchescu *et al.* (35) over the temperature range 100 - 300 K, and no phase transition was reported to occur.

1.3 Electrical Properties

Among the three polymorphs, orthorhombic rubrene is obviously the most studied because of its semiconducting behavior; nevertheless, the driving-force of the outstanding semiconducting properties of rubrene as well as the origin of its charge carrier transport phenomena and high mobility values are still far from reach. In particular, the effect of the oxidation on the transport properties of rubrene single crystals is still under discussion and up to now evidence of both an enhancement and a negative effect of the process on the transport properties of rubrene have been reported in the literature, leading to contradicting theories still subject to debate (36–39). Mitrofanov *et al.* (38), as an

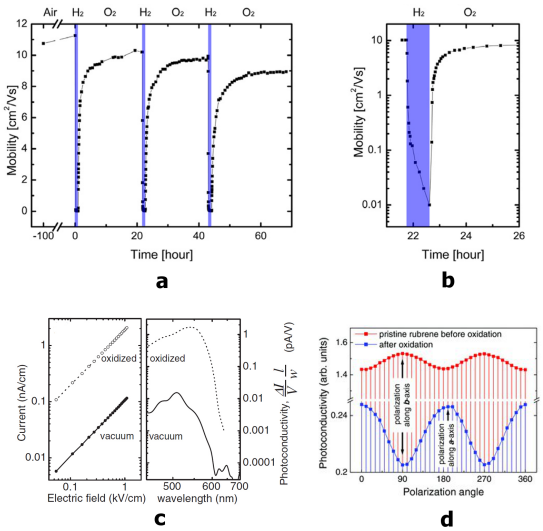

Figure 1.4: **a**) Effective mobility change in H_2 and O_2 in three cycles and **b**) of a single cycle in log scale, from (36); **c**) Dark current-voltage characteristics and photocurrent spectral response of an oxidized rubrene sample and a sample held in vacuum, from (38); **d**) Polarization dependency of the photoconductivity of a rubrene crystal, from (37).

example, documented a huge improvement of both conductivity and photoconductivity

values measured on oxidized single crystals, compared to those measured on pristine rubrene. Some years later, Zhang *et al.* (36) confirmed this behavior, showing how after exposing the surface of rubrene single crystals to pure oxygen, a clear increase in the mobility could be noticed. On the contrary, exposure of the same sample to pure hydrogen gas resulted in a drastic decrease in the mobility until oxygen was reintroduced in the experimental chamber. In total disagreement with this, Najafov *et al.* (37) stated lately that the photoconductivity of single crystals exposed to oxygen and light decreases with increasing oxygen exposure time, due to the diffusion of oxygen inside the crystal, which increases the trap density. Although an unambiguous explanation of the transport phenomena of rubrene has not yet been proposed, the importance of the planarity of the tetracene backbone and of the π-π stacking arrangement of the molecules in the crystal has been clearly underlined by da Silva Filho *et al.* (40): Figure 1.5 shows the shape of the HOMO and LUMO levels calculated for orthorhombic rubrene; in the ground-state neutral geometry, energy levels are very similar to those calculated for tetracene, because the almost complete orthogonality between the phenyl rings and the tetracene backbone in rubrene prevents the mixing of the orbitals of the aromatic core with those of the side groups.

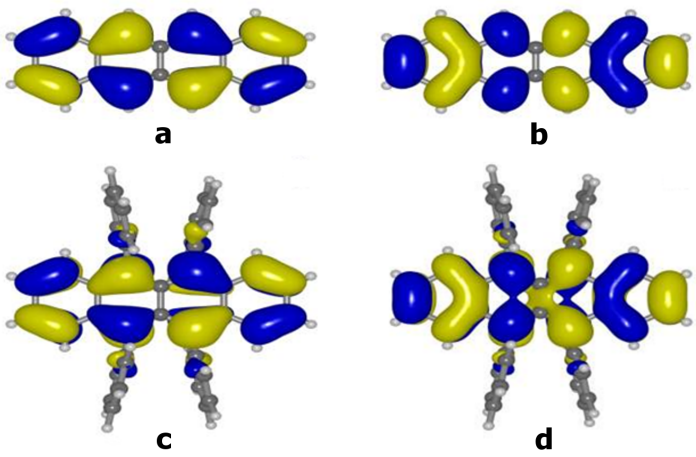

Figure 1.5: Calculated HOMO and LUMO wavefunctions in the neutral ground-state geometry: **a**) tetracene HOMO (-4.87 eV); **b**) tetracene LUMO (-2.09eV); **c**) rubrene HOMO (-4.69 eV); **d**) rubrene LUMO (-2.09 eV). From (40).

The presence of these bulky substituents on the tetracene core, however, modifies the typical arrangement of the molecules that is found in tetracene and in pentacene:

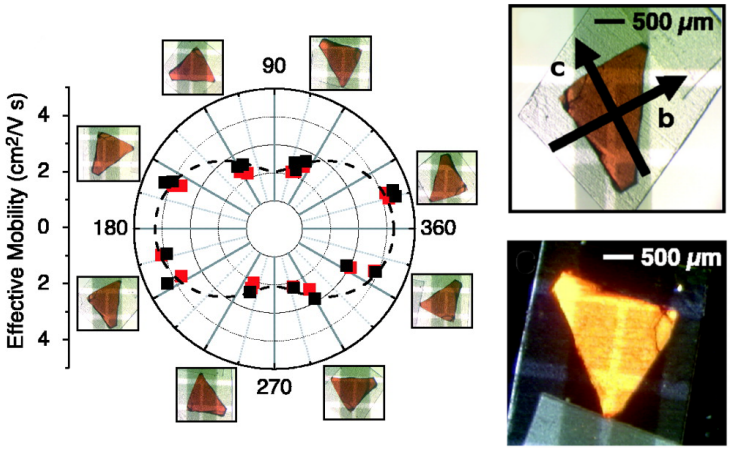

Figure 1.6: Polar plot of the mobility at the *bc* surface: the angle is measured between the *b* axis and the conducting channel (*left*); optical images of the crystal sample used in the experiment, the lower one viewed under cross polarizers (*right*). From (41).

the herringbone in the (001) plane of tetracene and pentacene involves the short axis of the molecules, while in orthorhombic rubrene the herringbone involves the long axis of the tetracene core. As a result, rubrene molecules π-stack in the *b* direction with a distance of 3.74 Å, thus maximizing the value of transfer integral for the HOMO and LUMO levels. This is related to the electronic coupling between adjacent molecules, a key parameter for the description of the transport properties of PAH-based materials.

Along the *b* direction, the value of this parameter is larger than any other direction and this is perfectly matching with the anisotropic character of the charge transport inside the crystal: along this direction charge carrier mobility can reach values which are comparable to those of amorphous silicon, as high as 40 cm^2/Vs. The polar plot of typical mobility values measured on a single crystal of orthorhombic rubrene along different directions in the (*bc*) plane, is reported in Figure 1.6. An additional proof of the pivotal importance of the π-π interaction for the electrical transport properties of orthorhombic rubrene is given by the study of the hydrostatic pressure dependence of charge carrier transport in single-crystal rubrene devices, by Rang *et al.* (42); the authors monitored the mobility inside a sample of orthorhombic rubrene while applying pressure to the crystal and showed how as the π-stacking distance decreases as a result of the applied pressure, an increase in the mobility can be measured. Although π-stacking with a similar stacking distance is found also in the triclinic polymorph of rubrene, the absence of a herringbone disposition of the molecules in the crystal structure, together with a small short-axis displacement results in a poor charge-carrier mobility; this has been evaluated by Matsukawa *et al.* as at least one order of magnitude lower than

that of the orthorhombic polymorph (43): the authors ascribe this evident difference of electrical response between the two polymorphs to the difference in density of π-stacking columns in the plane orthogonal to the direction of conduction, which is lower in the case of triclinic rubrene.

2 | Rubrene derivatives

2.1 Hirshfeld Surface Analysis

Comparing and contrasting different molecular crystal structures, even structures containing the same molecule, may appear as a straightforward task that could be performed at a number of levels, but when the need is to quantify the degree of similarity and difference among them for the purposes of crystal design and crystal engineering, the understanding of a molecular crystal packing suddenly turns out to be a much more difficult activity. This point was emphasized by G. Desiraju (44) when he observed that *"Many will appreciate that the structure of, say, naphthalene resembles that of anthracene more than it resembles benzene. Is it possible to quantify such comparisons? If so, such quantification would amount to pattern matching and becomes important because crystals that are structurally similar are also likely to have similar properties."* This quote seems to perfectly fit to the framework of rubrene and its derivatives, as the preservation of the properties displayed by a crystal structure - that of the orthorhombic phase, indeed - is the final goal of every synthetic effort directed towards producing orthorhombic rubrene-like systems, with better stability and solubility but unaltered electronic and transport properties. In this context, it is mandatory to provide researchers with a tool being capable of identifying and quantifying the analogies and differences not only between polymorphs, but also between structures containing different molecules, as in the case of chemically modified derivatives. This aspect becomes even more important if we consider the impossibility to predict, at the synthetic stage, which crystal structure one derivative will adopt and, as a direct consequence, the need to compare the solid state arrangement of every novel molecule with the packing motif of the original one.

A useful tool that makes it possible to quantify in an objective way the degree of similarity between crystal structures of different molecules and polymorphs is given by the Hirshfeld surface analysis (45). It was originally introduced as an extension of Hirshfeld's stockholder concept (46) which partitioned the electron density of a molecule into continuous atomic fragments: generalizing the concept, overlapping and continuous molecular fragments inside a crystal can be directly extracted from the experimental electron densities, defining a weight function $w(\boldsymbol{r})$:

$$w(\mathbf{r}) = \sum_{A \in molecule} \rho_A(\boldsymbol{r}) / \sum_{A \in crystal} \rho_A(\boldsymbol{r})$$

$$= \rho_{promolecule}(\boldsymbol{r}) / \rho_{crystal}(\boldsymbol{r})$$

Here $\rho_A(\boldsymbol{r})$ is a density function centered on a spherical and non interacting nucleus A, while the promolecule and procrystal are the sums over the atoms belonging to a single molecule and to the rest of the crystal, respectively. Molecular properties were originally obtained by integration over the weighted electron density $w(\boldsymbol{r})\rho_A$, with $0 < w(\boldsymbol{r}) < 1$. Spackman and Byrom, instead, considering the isosurface defined by $w(\boldsymbol{r}) = 0.5$ - the so called Hirshfeld surface (HS) - defined a region inside the HS where the contribution to the electron density of the enveloped molecule (the promolecule) exceeds that of all the neighboring molecules in the crystal (the procrystal). The novelty of this description of a molecule inside a crystal is that it allows to partition the crystal itself into non overlapping, single-molecule regions, as well as intermolecular voids where there is almost total absence of electron density. Like for any other continuous three-dimensional function, it is possible to define for each point of the HS an outward normal given by the gradient $\mathbf{n} = \bigtriangledown w$, together with two principal directions $\boldsymbol{u}$ and $\boldsymbol{v}$, depicted in Figure 2.1. This parameters are related to the principal curvatures of the surface κ_1 and κ_2:

$$\kappa_1 = -\frac{1}{|\mathbf{n}|}\frac{\partial^2 w}{\partial u^2} \qquad \text{and} \qquad \kappa_2 = -\frac{1}{|\mathbf{n}|}\frac{\partial^2 w}{\partial v^2}$$

κ_1 and κ_2 appear in the expressions for the calculation of some properties related to

the shape of the HS, as for example *Curvedness, C* and *Shape index, S*

$$C = (2/\pi)\ln[({\kappa_1}^2 + {\kappa_2}^2)/2]^{1/2}$$

$$S = (2/\pi)\arctan[(\kappa_1 + \kappa_2)/(\kappa_1 - \kappa_2)]$$

whose values can be easily plotted directly on the three-dimensional surface in an intuitive color code, described in the caption of Figure 2.1. The distances d_i and d_e, respectively the distance of a point on the HS from the closest nucleus of the molecule inside the surface, and that from the nearest nucleus of another molecule outside the surface, can also be plotted on the surface, providing a three-dimensional picture of the intermolecular close contacts in the crystal. The limitation of these parameters is that they do not take into account the relative sizes of atoms, so close contacts between larger elements are often not effectively displayed. For this reason a normalized contact distance d_{norm} (47) was defined:

$$d_{norm} = \frac{d_i - {r_i}^{vdW}}{{r_i}^{vdW}} + \frac{d_e - {r_e}^{vdW}}{{r_e}^{vdW}}$$

where r^{vdW} is the van der Waals (vdW) radius of the appropriate atom internal or external to the surface. d_{norm} can either be negative or positive where contacts shorter or greater than vdW separations occur, and is displayed using a red–white–blue color scheme, where red highlights shorter contacts, white is used for contacts around the vdW separation, and blue is for longer contacts. In this way, because of the symmetry in d_e and d_i of d_{norm}, any close intermolecular contact will be highlighted by two identical red spots, brighter and larger as internuclear separations decrease.

A further improvement of the method consists in the construction of the so called 2D fingerprint plot (FP): as every point on a HS is associated to a pair of distances d_e and d_i, it is possible to create a 2D-graph where every pixel represents a bin of width 0.01 Å in these two distances. The color of each pixel is a function of the fraction of surface points in that bin, ranging from blue (relatively few points) through green (moderate fraction) to red (many points). The resulting 2D-graph is a grid of colored points, usually over the range 0.4–2.6 Å in d_e and d_i. The most obvious characteristics of these plots are their pseudo-symmetry about the diagonal where $d_e = d_i$ and the relatively

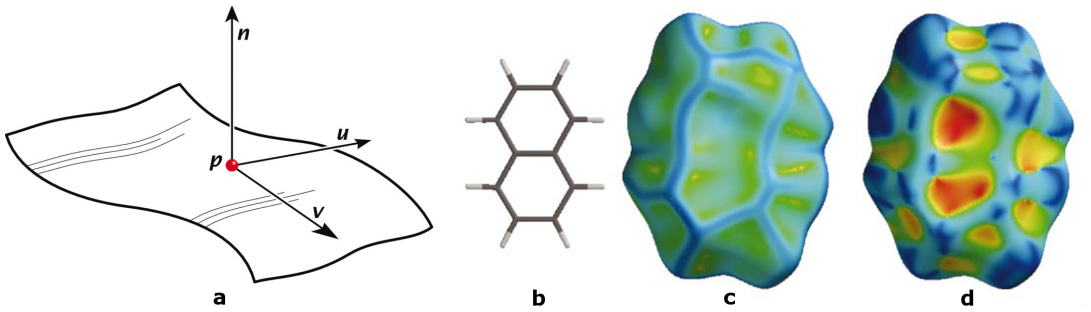

Figure 2.1: **a**) Schematic diagram of $\boldsymbol{n}$, $\boldsymbol{u}$ and $\boldsymbol{v}$ for a model surface; **b**) molecular structure of naphtalene, with the corresponding **c**) curvedness, C, and **d**) shape index, S, mapped on the HS. C is mapped from -4.0 (flat;red) $\Rightarrow$ 0.0 (unit sphere; cyan-green) $\Rightarrow$ +0.4 (edge; blue); S is mapped from -1.0 (concave umbilic; red) $\Rightarrow$ 0.0 (minimal saddle; green) $\Rightarrow$ +1.0 (convex umbilic; blue) as from (48).

limited range of the points (none are found at very long or very short distances), plus a number of additional features that are typical of the crystal structure under examination and of the intermolecular contacts inside it; these features have been assigned to real atom-atom interactions and listed in detail by Spackman and McKinnon (49). The pseudo-symmetry of the plot is a direct consequence of the close packing of the Hirshfeld surfaces, which guarantees that where surfaces touch one-another (and provided that there is only one molecule in the asymmetric unit) both of the points (d_i, d_e) and (d_e, d_i) will appear on the 2D fingerprint plot. The use of d_{norm} also makes it possible to isolate the contribution of a single type of atom-atom interaction from the general description of intermolecular contacts, both for HSs and for FPs; this allows to plot, either on the three-dimensional surface or on the 2D-plot, only those regions associated with a particular type of interaction and giving its corresponding percentage of occurrence with respect to the totality of the interactions. An example of the distance d_{norm} plotted on the HS of naphtalene and the corresponding FP are shown in Figure 2.2.

2.2 Rubrene Polymorphs

The first step of this thesis work consisted in analyzing the FP generated from the HS of the three known rubrene polymorphs, looking for the typical features indicating the presence of a herringbone π-stacking arrangement of the molecules inside the crystal: the main purpose of this preliminary check, was to identify these features in order to be

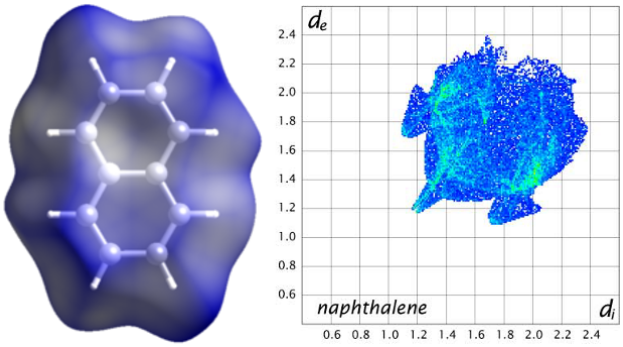

Figure 2.2: (left) d_{norm} HS for naphtalene, where the capped-stick model of the molecule is visible below the transparent surface. The almost totally blue color of the HS well describes the absence of any contact shorter than vdW separation; (right) the corresponding fingerprint plot.

able to recognize their occurrence also in the structure of rubrene derivatives; both HSs and FPs were produced with Crystal Explorer 3.0 (50), a program specifically designed for the Hirshfeld surface analysis, following the color code already described above. For a proper comparison of the polymorphic structures of rubrene, it was necessary to separate any variation of the intermolecular contacts due to differences in the packing features inside the crystal, from those related to the reduction of the unit-cell parameters caused by the temperature: for this reason the data chosen for the comparison are the closest in temperature and the corresponding CSD code of every crystal structure is always specified.

As shown in Figure 2.3, red regions on the d_{norm} HS for the orthorhombic polymorph of rubrene result almost only from H$\cdots$H close contacts between tetracenic hydrogens and hydrogens bound to the peripheral phenyls; both for the monoclinic and triclinic polymorphs, instead, there are also prominent C-H$\cdots\pi$ close contacts between the hydrogens of the peripheral rings and tetracenic carbons. The main feature of the d_{norm} surfaces for orthorhombic and triclinic rubrene is a large and flat light blue colored region over the acenic core of the molecules, corresponding to the π-stacking of the tetracene units, which is totally absent in the structure of monoclinic rubrene, as evidenced in Figure 2.3. In the π-stacking of the triclinic polymorph, moreover, a slight displacement along the short axis of the tetracene does occur. The absence of a mirror plane orthogonal to the tetracene core and parallel to its major axis on the d_{norm} surface, which is present instead in the orthorhombic polymorph, is the manifestation of this offset. The differences among the three rubrene polymorphs are even more evident if we compare their FP: both for orthorhombic and triclinic rubrene, the π-stacking of the tetracene units is confirmed by the presence of a green-yellow area between 1.8 and

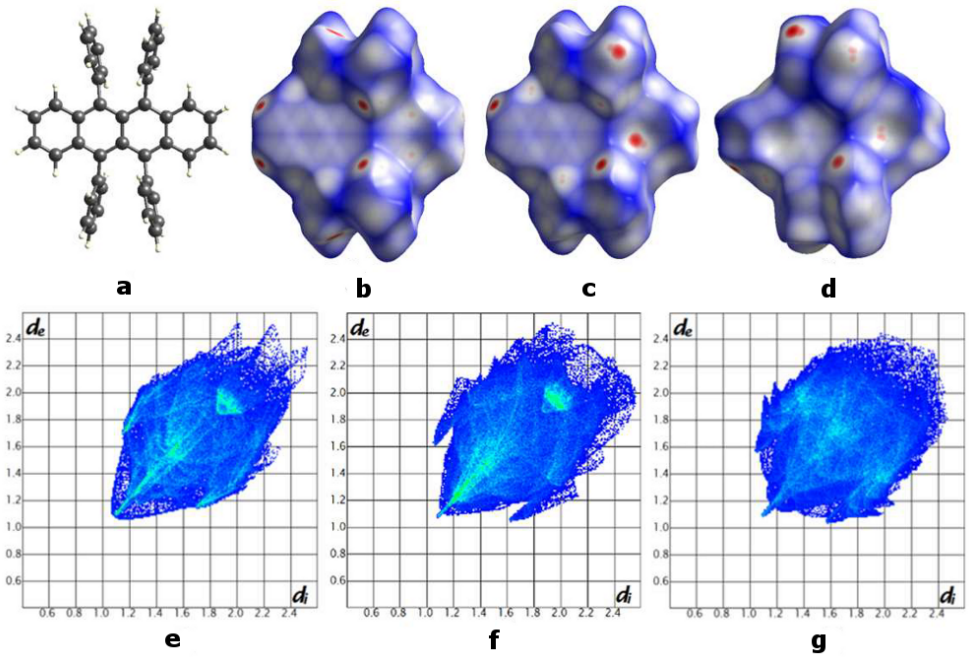

Figure 2.3: **a**) Ball-and-stick model for rubrene; d_{norm} HS for **b**) orthorhombic (QQQCIG07), **c**) triclinic (QQQCIG14), and **d**) monoclinic rubrene (QQQCIG13); corresponding fingerprint plot for **e**) orthorhombic, **f**) triclinic, and **g**) monoclinic rubrene.

2.0 Å (see Figure 2.3e and Figure 2.3f), a distance close to the vdW radius of carbon. Once again, this feature is totally absent for the triclinic polymorph, which shows, however, a distinct saw-tooth shape of the lower right side of the plot (partially present also in the plot for the monoclinic polymorph) corresponding to the C-H$\cdots\pi$ interactions previously found as red dots on the d_{norm} surfaces (49). Selective highlighting of C$\ldots$C contacts (i.e., $\pi\cdots\pi$) permitted to quantify the occurrence of the π-stacking motif as 6.3% for orthorhombic rubrene and 7.3% for triclinic rubrene at 175 K.

2.3 Rubrene Derivatives in the CSD

This analysis was extended to those rubrene derivatives whose crystal structure is available for a comparison with that of orthorhombic rubrene; these crystal structures were obtained from the CSD (v. 5.34) (51) by means of ConQuest 1.15 with the following filters applied: 3D coordinates determined, no ions, no powder structures, only organics. Solvate structures were not taken into account. Once again, all the comparisons between rubrene and its derivatives have been made by using the data set of orthorhombic rubrene that was closest in temperature to the data set of the derivative, in order to separate any variation of the intermolecular contacts due to differences in the packing features inside the crystal, from those related to the reduction of the unit-cell parameters caused by lowering of the temperature. For a clearer understanding of the whole analysis, the examined rubrene derivatives have been numbered and the most important details of their crystal structures are summarized in Table 2.1. In particular, the percentage of occurring C$\cdots$C contacts is reported, together with the effective surface area of the HS ($A_{\pi-\pi}$, in Å^2) involved in the $\pi\cdots\pi$ interaction.

The easiest comparison we can make is between rubrene and 5,12-bis(4-fluorophenyl)-6,11-diphenyltetracene (26) (CSD Refcode: TOMVUN, **2**); this derivative is in fact isomorphous and isostructural with orthorhombic rubrene, with only small differences among their cell parameters due to the presence of the two fluorine atoms which are disordered by symmetry, with occupancy 0.50. As expected, the two d_{norm} surfaces are visually identical, except for the red dots resulting from the contacts among the substituted hydrogens. In the same manner, the FP for the two surfaces is almost completely superimposable, if we exclude the fluorine contacts effects (Figure 2.4a). Selective highlighting of C$\cdots$C contacts, both on the d_{norm} surface and on the FP,

Table 2.1: Intermolecular C$\cdots$C contacts calculated by means of Hirshfeld surface analysis for rubrene polymorphs and derivatives

	Compound	Space group	CSD code	T(K)	$\%_{C\cdots C}$	$A_{\pi-\pi}$ (Å^2)
1	orthorhombic rubrene	*Cmca*	QQQCIG11	RT	6.1	31.99
			QQQCIG07	175	6.3	32.92
			QQQCIG05	125	6.4	33.34
1	monoclinic rubrene	$P2_1/c$	QQQCIG13	173	-	-
1	triclinic rubrene	$P\bar{1}$	QQQCIG14	173	7.3	37.81
2	5,12-bis(4-fluorophenyl)-6,11-diphenyltetracene	*Cmca*	TOMVUN	120	6.2	33.15
3	2,8-difluoro-5,11-bis(4-fluorophenyl)-6,12-diphenyltetracene	$P2_1/c$	AXIDER	RT	-	-
4	5,12-bis(4-fluorophenyl)-6-phenyl-11-(4-methoxyphenyl)tetracene	$P2_1/n$	TOMWAU	120	1.6	9.04
5	5,12-bis(4-methoxyphenyl)-6,11-diphenyltetracene	*Pbca*	TOMVOH	120	3.6	21.03
6	5,12-bis(4-tert-butylphenyl)-6,11-diphenyltetracene	*Pnma*	PIFHIW	RT	4.9	31.83
7	5,11-bis(4-tert-butylphenyl)-6,12-diphenyltetracene	$P2_1/c$	PIFHOC	RT	-	-

is very useful to show that for this derivative not only the occurrence of the C$\cdots$C contacts is comparable with the total percentage for orthorhombic rubrene at the same temperature (6.2% for the fluorine derivative at 120 K, 6.4% for orthorhombic rubrene at 125 K), but also that the region involved in the π-stacking is exactly the same (Figure 2.5).

In a similar way, derivative 2,8-difluoro-5,11-bis(4-fluorophenyl)-6,12-diphenyl-tetracene (24) (CSD Refcode: AXIDER, **3**) is isomorphous and isostructural with the monoclinic polymorph of rubrene and the small differences among their cell parameters do not significantly affect the packing motif. The HS of derivative **3** (Figure 2.4b) is superimposable to that of monoclinic rubrene, does not display any evidence of π-stacking of the tetracene units and also the FP confirms the almost total absence of C$\cdots$C contacts. The distinct saw tooth shape associated to C-H$\cdots\pi$ contacts on the FP of monoclinic rubrene is still present in **3**; the disappearance of the small red dots on both sides of the tetracenic core of monoclinic rubrene, and associated with this kind of interactions, can be related to the higher temperature of the data collection available for derivative **3** (room temperature), compared to that available for monoclinic rubrene (173 K). The contact between the fluorine atoms bound directly to the tetracene unit is evident from the red dots on the HS, but the total percentage of F$\cdots$F interactions is only 1.6%. Much larger is the percentage of occurrence of F$\cdots$H interactions (23.2%), where the closest contacts are those between a tetracenic fluorine and an *ortho*-hydrogen on the substituted peripheral phenyl of a molecule translated a unit cell in the *b* direction, as well as between the same fluorine and a *meta*-hydrogen on an unsubstituted phenyl ring on the molecule generated by the screw symmetry operator parallel to *b* (-x, 1/2+y, 1/2-z). These interactions generate, in the lower left part of the FP, a typical double spike shape which is the main difference between the FP of this derivative and that of the monoclinic polymorph of rubrene.

The effect of substituting a *para*-hydrogen on a peripheral phenyl ring of derivative **2** with a more bulky group, as we can see in the case of 5,12-bis(4-fluorophenyl)-6-phenyl-11-(4-methoxyphenyl)-tetracene (26) (CSD Refcode: TOMWAU, **4**), is dramatic: the monoclinic crystal structure of this derivative is totally different from the previous ones, the presence of the methoxy group resulting in the loss of planarity for the tetracene core that becomes twisted (the torsion angle among the two external bonds C5-C6$\cdots$C14-C15, defining the short edges of the tetracene backbone, is 35.2°) and is no longer

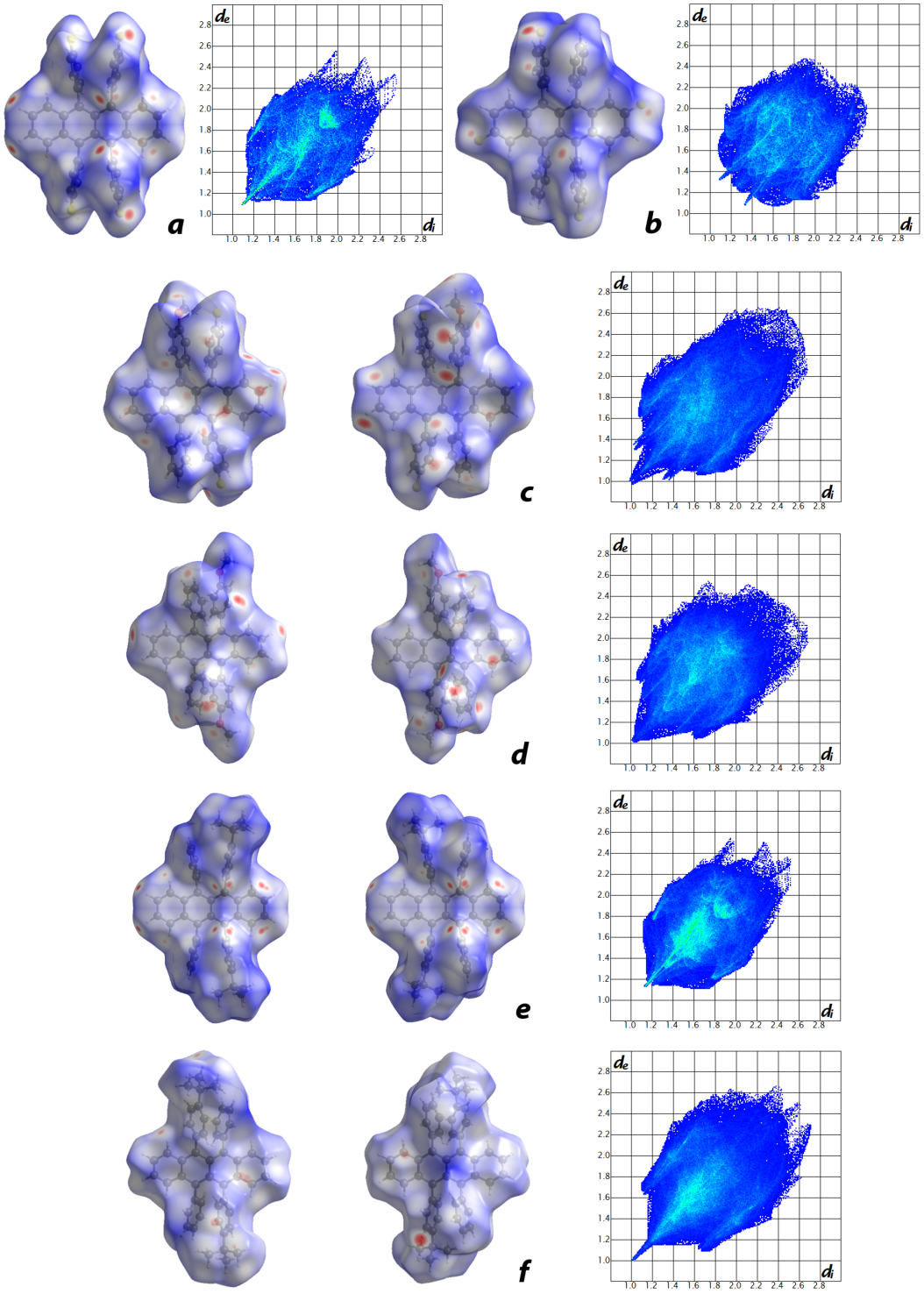

Figure 2.4: d_{norm} HS and Fingerprint plots of rubrene derivatives: **a**) TOMVUN, **2**; **b**) AXIDER, **3**; **c**) TOMWAU, **4**; **d**) TOMVOH, **5**; **e**) PIFHIW, **6**; **f**) PIFHOC, **7**.

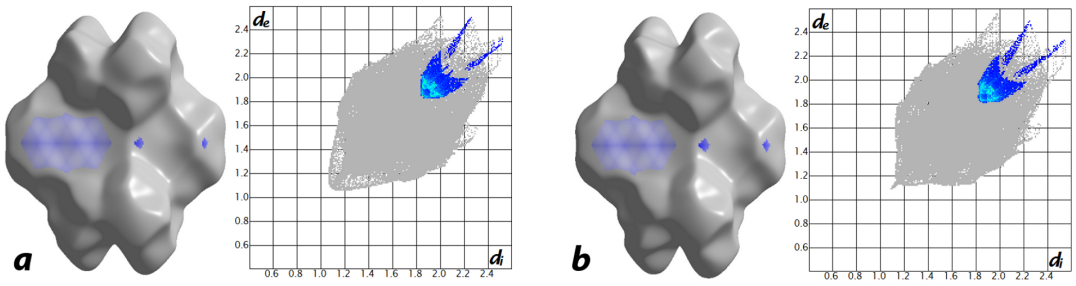

Figure 2.5: C···C contacts selective highlighting on d_{norm} surfaces and fingerprint plots of **a**) Orthorhombic rubrene at 125K (QQQCIG05) and **b**) TOMVUN, **2**.

arranged in π-stacks. The structure displays, in fact, couples of twisted molecules that are able to face one another only with a small portion of their tetracene core. The distinctive light blue flat region on the d_{norm} surface for derivative **4** is now drastically reduced and confined to only one side of it (see the right HS in Figure 2.4c). In addition to the previously mentioned H···H interactions, the closest contacts highlighted by the red dots on the HS are H···F interactions between a fluorine and a phenylic hydrogen next to the methoxy group situated on the adjacent molecule generated by the glide symmetry operator (1/2+x, 1/2-y, 1/2+z); O···H close contacts involving a tetracenic hydrogen generated by the inversion symmetry (-x, -y, -z) are also present. On the FP, the C···C contacts region is now colored in blue and shifted between 2.0 and 2.2 Å (Figure 2.4c), corresponding to a less relevant percentage of occurrence of only 1.6%.

Surprisingly, in the case of 5,12-bis(4-methoxyphenyl)-6,11-diphenyltetracene (26) (CSD Refcode: TOMVOH, **5**), where the fluorine atoms are not present and there is one more methoxy group with respect to derivative **4**, the molecules inside the crystal are still able to arrange in π-stacks, with a stacking distance of 3.73 Å, very close to that of orthorhombic rubrene. The disposition of molecules in the (001) plane of this orthorhombic cell is close to orthorhombic rubrene in the (100) plane, but the presence of bulky substituents is associated to tetracenic cores adopting a twisted shape, with a torsion angle among the two external bonds C14-C15···C31-C30 of 43.9°. Unlike orthorhombic rubrene, the molecules of this derivative do not occupy any special position inside the unit cell: according to the site symmetry of the molecule itself, this results in a d_{norm} surface that is not symmetric with respect to the two sides of the tetracene core. The percentage of occurrence of the C···C contacts on the HS raises to 3.6% compared

to **4** as evidenced by the greenish color of the FP region between 1.8 and 2.0 Å (Figure 2.4d). The closest hetero-contacts highlighted on the surface are C-H$\cdots\pi$ interactions involving an unsubstituted phenyl ring and a hydrogen ortho to the methoxy group of the adjacent molecule generated by the glide symmetry operator perpendicular to *a* (1/2-x, 1/2+y, z), as well as a tetracenic hydrogen and the portion of tetracene not involved in the π-stacking, on the molecule generated by the 2_1 symmetry operator parallel to *b* (-x, 1/2+y, 1/2-z). Also O$\cdots$H contacts are visible and occur between an oxygen atom and a hydrogen on an unsubstituted phenyl ring of a molecule generated by the 2_1 symmetry operator parallel to *c* (1/2-x, -y, 1/2+z); the second oxygen atom, instead, is close contacting on one side with a hydrogen on an unsubstituted phenyl ring generated by the glide symmetry operator perpendicular to *c* (1/2+x, y, 1/2 -z) and on the other side with the hydrogen next to the methoxy group of the molecule generated by the glide symmetry operator perpendicular to *b* (x, 1/2-y, 1/2+z).

The effect of a bulky group on the planarity of the tetracene core of a rubrene derivative is not necessarily negative and related with a torsion; in the case of 5,12-bis(4-tert-butylphenyl)-6,11-diphenyltetracene (28) (CSD Refcode: PIFHIW, **6**), the presence of two bulky tert-butyl moieties do not induce any twisting on the tetracene, thus allowing the existence of π-stacking inside the crystal. The herringbone disposition of the molecules in the (010) plane of the orthorhombic cell of this derivative is once more very close to the (100) plane of orthorhombic rubrene, with only a small difference in the herringbone angle (62.3° for orthorhombic rubrene and 59.1° for derivative **6**) and a short stacking distance for adjacent molecules of 3.55 Å. This feature becomes evident by analyzing the d_{norm} surface for **6**, displaying the typical light blue colored flat region over both sides of the tetracene unit, resulting again in a greenish region of the FP between 1.8 and 2.0 Å (Figure 2.4e). All the red dots on the surface are the consequence of H$\cdots$H close contacts, without involving in any way the tert-butylic groups that fit with the adjacent (010) layer. Therefore, also for this derivative, selective highlighting of C$\cdots$C contacts clearly shows that the region involved in the π-stacking is exactly the same found for orthorhombic rubrene at the same temperature (Figure 2.6), with an occurrence of C$\cdots$C interactions slightly lower than rubrene (4.9% for the tert-butylic derivative, 6.1% for orthorhombic rubrene, both at RT). Nevertheless, considering the larger surface area corresponding to the HS of derivative **6** compared to that calculated for the HS of orthorhombic rubrene, the absolute area of the π-stacking

region is essentially identical (31.83 Å^2 for the tert-butylic derivative, 31.99 Å^2 for orthorhombic rubrene).

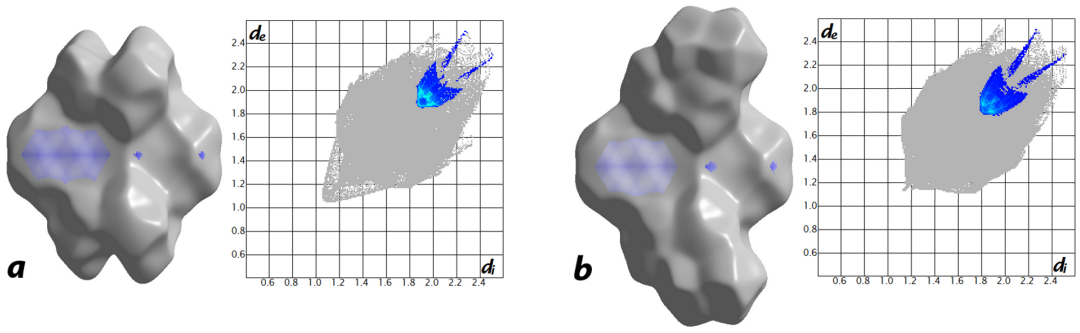

Figure 2.6: C···C contacts selective highlighting on d_{norm} surfaces and fingerprint plots of **a**) Orthorhombic rubrene at RT (QQQCIG11) and **b**) PIFHIW, **6**.

When the two tert-butylic groups are bound to the peripheral phenyl rings in 5,11-position (28), instead of the previous 5,12-position, the effect of the substitution on the packing motif of the derivative 5,11-bis(4-tert-butylphenyl)-6,12-diphenyltetracene (CSD Refcode: PIFHOC, **7**) is again dramatic; its monoclinic crystal structure shows no π-stacking or herringbone disposition of the molecules. The tetracene cores are twisted (the torsion angle among the two external bonds C1-C2···C18-C17 is 42.4°) and, despite the molecule itself could suggest the presence of a 2-fold rotation axis passing through the centroid of the tetracene unit, there is no such a symmetry element. On the d_{norm} surface for **7**, C-H···π close contacts are present between a hydrogen atom on an unsubstituted phenyl and the tetracene of an adjacent molecule generated by the glide symmetry operator (x, 1/2-y, 1/2+z), as well as between a hydrogen next to the tert-butylic group and the tetracene of the same molecule a unit cell far away in the b direction. The closest contacts are however H···H interactions involving the other hydrogen next to the tert-butylic group and one of the hydrogens of the tert-butyl of the molecule generated by the 2-fold screw symmetry operator (-x, 1/2+y, 1/2-z). On the FP there is no region corresponding to the C···C contacts of π-stacking (Figure 2.4f). The full structure of a second polymorph of this derivative has not been completely determined because of the thinness of the crystals, even though the (00l) reflections indicate a molecular packing possibly analogous to the 5,12 constitutional isomer (28): the in-plane hole mobility of 12 cm^2/V·s measured on single-crystal field-effect transistors (FETs) built with the second polymorph of compound **7** was just as

high as in rubrene crystals. Although no similar measurement has been reported for derivative **6**, this is a further proof of the fact that neither the size of the substituent nor the choice of the ring on which the substitution does occur is necessarily associated with a twisted conformation of the tetracene core in the solid state implying the loss of $\pi \cdots \pi$ interactions. Analogously, the favorable herringbone disposition of the molecules observed in orthorhombic rubrene, with the tetracene cores arranged in π-stacks, can occur also for derivatives bearing substitutents on the *para* position of their peripheral phenyls. In such cases, since the monomolecular layer extracted from the d_{200} slice of orthorhombic rubrene is preserved, similar electronic properties could be observed.

2.4 Conclusions

Aiming at a deeper understanding of the semiconducting behavior of orthorhombic rubrene and to a possible improvement of its stability and solubility by means of chemical modification, all the known structures of derivatives of rubrene have been systematically analyzed. Although this class of compounds is still poorly represented and no general trend has emerged, it is interesting to note that a twisting of the tetracene core of the molecules occurs in some but not all of the cases. In some of the studied structures, despite the presence of bulky groups on 4-position of phenyl groups, it is still possible to observe the herringbone disposition of molecules typical orthorhombic rubrene. This means at least the (100) layer of orthorhombic rubrene, considered responsible for its high mobility due to the presence of the peculiar π-stacking motif within the d_{200} slice, can be preserved in other derivatives. This particular position for substitution, useful for imparting improved stability and solubility, seems to have high tolerance for allowing confinement of bulky groups at the surfaces of the (200) layer, while preserving at the same time the favorable $\pi \cdots \pi$ interactions of orthorhombic rubrene. This suggests the possibility to introduce different chemical modifications in the rubrene molecule in order to obtain more stable and/or more soluble derivatives, without significantly affecting the intermolecular contacts between first neighbors molecules, thus allowing to increase the ensemble of rubrene derivatives suitable for a full physical characterization.

3 | Experimental Methods

3.1 Single-Crystal Growth

The crystal growth techniques described in this section have been optimized to obtain single-crystalline individuals suitable for X-ray diffraction experiments. Typical promising crystals are transparent and sharp edged, as much free of macroscopic defects as possible and with preferred dimensions between 0.1 to 0.4 mm: growing single crystals of this size, in at least two of the three dimensions and a minimum thickness of 50 μm, ensures to have a sufficient crystal volume for diffraction. Whichever crystallization technique is chosen, supersaturation must be obtained, as nucleation occurs only if the system is out of its thermodynamic equilibrium. When the material of interest displays good solubility in a suitable solvent, it is possible to grow crystals by solution methods: supersaturation conditions can be reached either *via* evaporation of the solvent or *via* cooling of the solution, as schematically described in the diagram of Figure 3.1.

In the first scenario (*isothermal slow evaporation from a saturated solution*), a sample vial is left in open air (or in a inert atmosphere if the solution is not oxygen-stable): the volatility of the solvent, the temperature, the area of the solution surface exposed and the width of the opening of the vial itself, are experimental variables that define the rate of evaporation of the solution. The second strategy (*cooling of a supersaturated solution*) is preferred when less soluble systems are employed, and nucleation is triggered by gradually decreasing the temperature of a previously heated solution, within a sealed vial: when the amount of material dissolved at higher temperature exceeds the concentration at the saturation point at lower temperature, the system enters a supersaturation state and nucleation is possible. Both the above techniques may also be improved by changing the solvent or by the choice of a solvent mixture: different

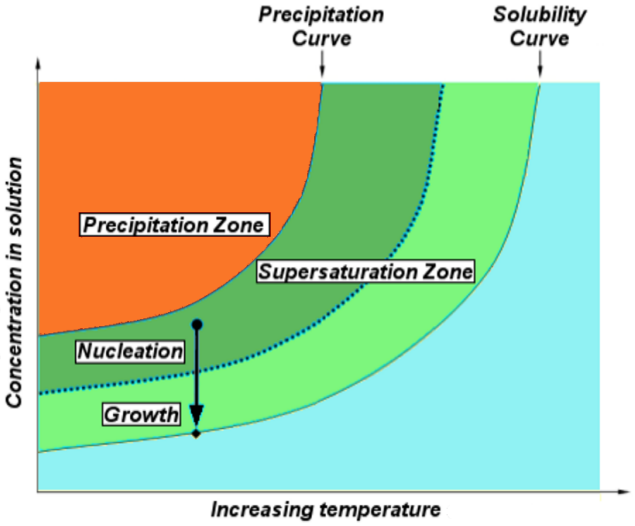

Figure 3.1: Schematic diagram of crystallization. Nucleation needs a superasaturated solution to occur; growth stops when the solubility limit is reached and the crystal is in equilibrium with the surrounding solution.

solute-solvent interactions, in fact, could inhibit or promote growth of particular crystal faces and hence yield crystals of suitable morphology. An efficient method to grow organic molecular crystals of oligoacenes such as rubrene and tetracene is the *physical vapor transport* (PVT) method (52, 53), schematically depicted in Figure 3.2: a crucible containing the starting material is placed at one end of a quartz tube and heated to the sublimation point of the compound, either in a vertical or horizontal configuration. By means of a smaller tube inserted in the larger one, an inert gas flux is conveyed towards the crucible and then expelled from the opposite opening of the quartz tube. Due to a properly chosen temperature gradient established along the tube, the sublimated molecules are transported by the gas and deposited on the inner walls of the tubes, leading to the formation of crystals whose size and shape will depend on the growth conditions, *i.e.* temperature profile and gas flux.

Within this work, the rubrene derivatives of interest appeared incompatible with this technique, because they proved to degrade before reaching the sublimation temperature at ambient pressure; a *reduced pressure sublimation* was then performed. Instead of an inert gas line, the quartz tube was connected to a vacuum pump used to reduce the pressure inside the tube, in order to decrease the temperature needed for the compound to sublimate and thus avoid its degradation. In the experimental configuration, the molecules heated above their sublimation point (T2), move along the tube following the temperature gradient properly established (T1-T3), until they reach a condensation zone where a lower temperature allows crystals to nucleate and grow on the walls of

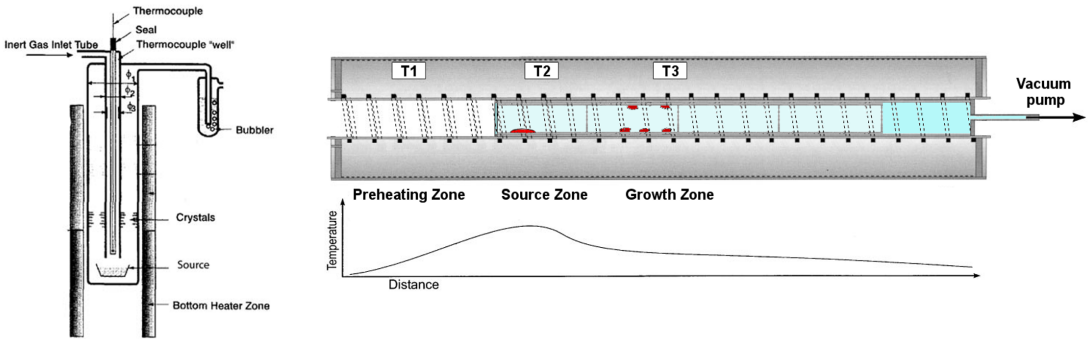

Figure 3.2: (*left*) Illustration of the vertical PVT growth technique, from (52); (*right*) horizontal configuration of the reduced pressure sublimation apparatus used within this work, with the three set temperatures T1 > T2 > T3.

the tube (T3): nucleation and growth rate can once again be tailored by modifying the temperature profile or the pressure inside the quartz tube (see Figure 3.2). To facilitate the harvesting process of the grown crystals, a series of short glass cylinders fitting within the quartz tube was lined up inside it, in order to provide an easily-removable substrate where the nucleation and growth of the crystalline individuals could occur.

3.2 X-Ray Single-Crystal Diffraction

X-ray diffraction (XRD) is the most definitive technique to obtain, at the atomic level, a detailed three-dimensional picture of the contents of a crystalline solid, defined as a three-dimensional array of identical unit cells with long range order and translational symmetry. This periodicity is the basis of a XRD experiment, as diffraction arises from the interference (both constructive and destructive) of scattered photons, produced by the elastic interaction of an incident electromagnetic radiation with the electron density of atoms within a crystal structure. As the wavelength of X-ray radiation is comparable with interatomic distances in solids (typically of the order of a few Ångstroms), the interference of photons, scattered by different atoms within the structure, results in a diffraction pattern, from which it is possible to determine precisely the positions of individual atoms and their arrangement within the solid. As a consequence, also interatomic distances, bond angles and other features of the molecular geometry of interest such as the planarity of a particular group of atoms or angles between planes, can be obtained, thus extending our understanding of interactions between molecules.

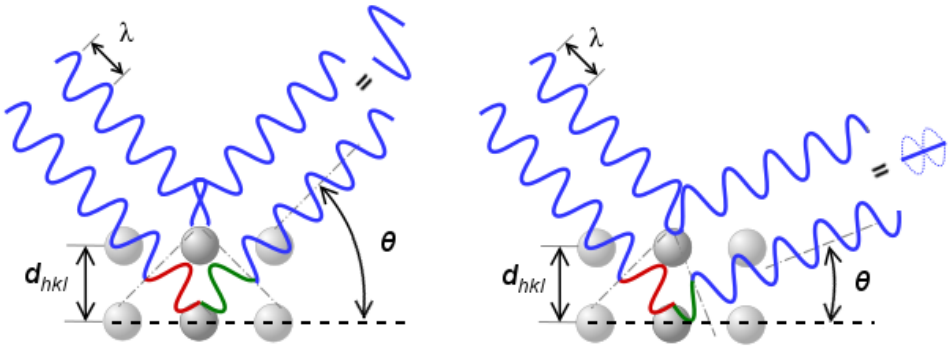

Figure 3.3: The Bragg construction for diffraction by a three-dimensional crystal lattice. In this scheme the incident X-rays (blue) are diffracted by two separate crystal planes, separated by a distance, d_{hkl}. For constructive interference to occur, the path difference between two diffracted beams should be an integer multiple of their wavelength (*left*). This situation arises only at certain scattering angles (θ); at all other angles the beams will interfere destructively (*right*)

The condition for having constructive interference of scattered radiation, given its wavelength λ, is that the path difference of two X-ray waves must be a multiple integer of the wavelength itself, that is $n\lambda$. This path difference can be expressed in terms of the interplanar spacing between the lattice planes, and in terms of the angle of incidence of the radiation, as demonstrated by Bragg (54) and depicted in Figure 3.3: constructive interference occurs when two X-rays are in phase, *i.e.* for

$$n\lambda = 2d_{hkl}\sin\theta \tag{3.1}$$

where n is an integer, d_{hkl} is the spacing between the family of planes identified by the reciprocal space vector of components *hkl*, and θ is the angle of incidence of the radiation. At other angles of incidence or interplanar spacings, the scattered X-rays will be partly or completely out of phase (destructive interference). Observed intensities in the diffraction pattern provide information about the amplitudes of the scattered waves and this information is enough to index the unit cell (from the relative positions of the diffracted peaks) and sometimes also to determine the space group of the crystal, but it is not sufficient to reconstruct its content; both the amplitudes $|F(hkl)|$ and the phases ϕ of the scattered X-rays are required, in fact, to represent the electron density $\rho(xyz)$ of the atoms that interacted with the radiation:

$$\rho(xyz) = \frac{1}{V}\sum_{hkl}|F(hkl)|\exp[i\phi(hkl)]\exp[-2\pi i(hx+ky+lz)] \tag{3.2}$$

In an optical microscope, the visible light scattered by an object is recombined by the objective lens system so that the relationship between the phases of the scattered waves is maintained: in a similar way, X-rays are scattered by the electrons of atoms but, unlike visible light, these X-rays can not be recombined by any presently known experimental technique and every information about phases is lost during the diffraction process. In fact, the relationship between the diffracted intensities and the so-called *structure factor, F(hkl)*, involves only its amplitude part and gives no information about the phase part:

$$F(hkl) = |F(hkl)| \cdot \exp[i\phi(hkl)] \tag{3.3}$$

$$I(hkl) = |F(hkl)|^2 \cdot A \cdot LP \tag{3.4}$$

here LP is a combined geometry and polarization factor which depends on the particular experimental setup and A is an absorption correction factor. The structure factor can be seen as the sum of the contributions to each scattered wave, from each atom i of the structure independently, taking appropriate account of differences in the phase angle of each wave.

$$F(hkl) = \sum_i f_i \cdot \exp[2\pi i(hx_i + ky_i + lz_i)] \tag{3.5}$$

The *atomic scattering factor* of an atom, f_i, represents its scattering power and can be computed from quantum mechanics: it is higher for heavier atoms, decreases with increasing scattering angle and it depends also on thermal vibrations. The possibility to accurately calculate atomic scattering factors for all the elements permits to estimate the phases from the observed X-ray intensities of the measured diffraction peaks, by means of a statistical analysis.

3.3 Diamond-Anvil Cells

High-pressure X-ray diffraction analyses presented in Chapter 5 were performed using a diamond-anvil cell (DAC). This kind of device is built on a relatively simple concept:

a sample can be pressurized between the faces (culets) of two opposing diamonds, when a force pushes them together. Behind this basic principle there is more than half a century of technology development and experimental efforts: the original idea was introduced by Lawson and Tang in 1950 (55) and the work by Merrill and Bassett in 1974 (56) is recognized worldwide for its fundamental contribution to the modern concept of a DAC. In more recent years, DACs have been widely used to study a variety of samples, including condensed gases, amino acids, proteins, pharmaceutical compounds and organometallic compounds, allowing researchers to perform a number of different measurements such as spectroscopy, magnetism and diffraction (57–59). For the purposes of single-crystal diffraction, the Merrill-Bassett DAC probably represents the best choice, mainly because of its small size and ease of use, together with the possibility of mounting it on a goniometer head: the cell consists of two small-sized triangular steel platens ($\sim$ 5 cm) that are pulled together by three screws, as schematically depicted in Figure 3.4.

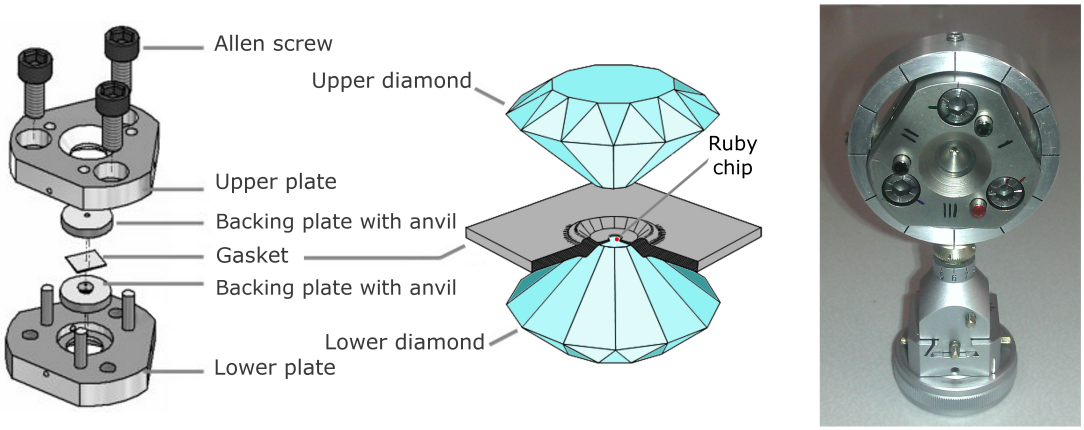

Figure 3.4: A Merril-Bassett DAC divided in its basic components (*left*, from (60)) and a real picture of one of the DACs used within this work, mounted on a goniometer head (*right*).

In the original design, on each platen, a beryllium backing seat is used to support the diamonds and act as an X-ray window, providing tensile strength and good transparency to X-rays: apart from the toxicity of beryllium, the contamination of the diffraction image by powder rings arising from X-ray scattering from the polycrystalline metal, may be accounted as the only disadvantage of this design, especially when synchrotron X-ray beams are employed and the beryllium lines become more intense and more

textured in appearance (60). Steel or tungsten carbide (WC) backing seats provide now an alternative. These materials are opaque to X-rays and therefore, in practice, large conical holes are required to maintain the opening angle of the pressure cell, as opposed to the smaller optical hole needed for beryllium seats and for the same anvil mounting design. This implies that larger anvils, which are not only more expensive but also more absorbing, need to be employed so that the diamonds have proper support while sitting on the backing plates. A recent design of anvil and backing seat (the Boehler-Almax design) (61, 62), where the diamond anvils are embedded in a WC backing seat, provides conical support to the anvils without loss of pressure range and sample volume, while the sizes of the conical anvils used are much smaller than those used with conventional WC backing seats. This construction allows the full opening angle of the steel platens (*ca.* 80°, depending on the cell design) to be utilized, while still ensuring the anvils are adequately supported for applications at very high pressures (see Figure 3.5). In this work, a modification of the DAC described by Moggach *et al.* (60) was used, where Boehler-Almax diamonds embedded in WC backing seats within a triangular DAC, with wider conical openings (85°).

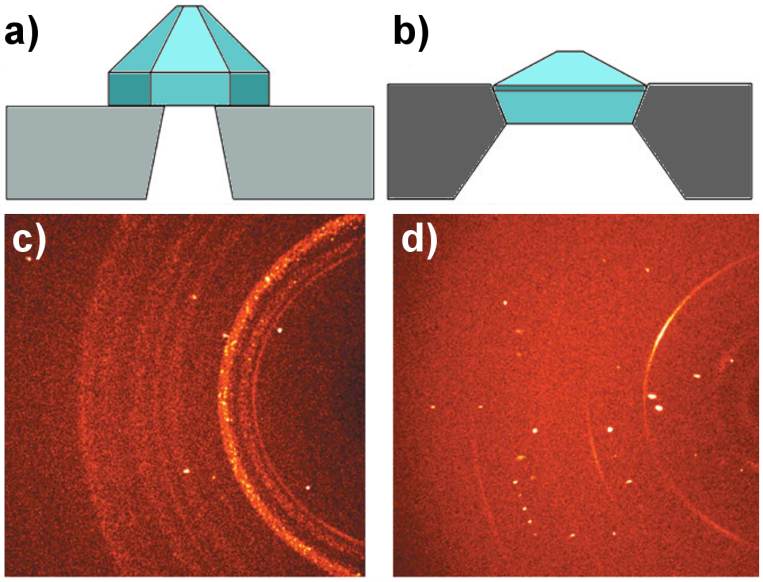

Figure 3.5: Comparison of the effect different backing plates have on the quality of the diffraction data: Be-backed diamond (*a*) and corresponding diffraction image with beryllium rings (*c*); plates and diamonds of the Boehler-Almax design (*b*) and corresponding diffraction image with only gasket rings visible (*d*). From (60).

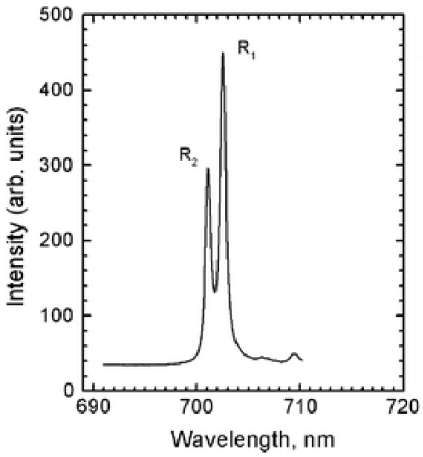

Figure 3.6: The typical R_1-R_2 high-pressure fluorescence signal of a ruby sphere, used to monitor the pressure inside the DAC.

The pressure chamber, where the sample can be loaded, consists of a metal gasket that has been drilled, in order to obtain a cylindrical hole, in the center of that portion of the gasket, which is sandwiched between the diamonds culets: typical materials of choice include steel, inconel (a Ni, Cr and Fe alloy) or tungsten and display high mechanical strength. In order to minimize the risk of gasket failure, the diameter of the hole must not exceed half the size of the diamond culets. The size of the gasket hole determines the maximum value of the pressure that can be reached and, at the same time, also the maximum size of the crystal to be measured within the DAC: a well-considered choice of the gasket diameter is, therefore, fundamental. The decrease of the volume of the chamber that is needed for the pressure to increase, is gained through the reduction of the thickness of the gasket during the experiment. A useful procedure commonly used to stabilize the diamond anvils before drilling the gasket hole, is the pre-indentation of the gasket, realized through a carefully controlled compression of the metal gasket between the diamonds culets: by flowing around the diamonds, the extruded material will offer a better support to the anvils and the gained hardness of the walls of the pressure chamber will reduce the risk of gasket failure. The pressure inside the experimental chamber of the DAC can be monitored by means of a ruby sphere (Al_2O_3:Cr^{3+}), used as pressure sensor (63): the R_1 and R_2 electronic transitions excited by laser-induced fluorescence and depicted in Figure 3.6, undergo a pronounced red-shift with applied pressure. At ambient temperature, this dependence is linear up to at least 20 GPa, while at elevated temperatures the fluorescence signal undergoes significant broadening and it becomes difficult to obtain a reliable measure of sample pressure. The R_1-R_2 separation is also

a useful indicator of the hydrostatic conditions within the sample chamber: whenever the ruby chip is experiencing a non-hydrostatic regime, these spectral lines overlap, increasing the uncertainty in the pressure measurement. Within this work, the ruby fluorescence was excited with a 532 nm laser and collected by means of a in-house built kit with a typical precision of ±0.05 GPa. The details for each high-pressure experiment will be reported in the relevant sections.

3.4 High-Pressure Single-Crystal X-Ray Diffraction

Collecting X-ray diffraction data from a single-crystal sample within a DAC presents three main challenges arising directly from the interaction of the components of the pressure cell with the X-ray radiation:

- the steel body of the cell severely reduces the amount of accessible reciprocal space, if compared to that sampled by a classic *in-air* data collection (see Figure 3.7).
- contamination of the diffraction pattern due to the two diamond anvils.
- contamination of the diffraction pattern due to the gasket and to Be backing plates, when used, as described earlier.

At the data-collection stage, only the first issue can be addressed. By using a proper data-collection strategy, completeness of high-pressure diffraction data can be optimized (57); moreover, additional completeness can be gained by repeating once or twice the same data-collection, by rotating the cell in the beam, either manually on a 3-circle diffractometer, or by choosing different values of the χ angle on a 4-circle diffractometer. Subsequently, an optimization of the methods for for indexing and integrating the diffraction intensities is needed. For instance, the program SAINT (64) used for integration and global-cell refinement provides advanced options to take into account the opening angle of the DAC, among the integration variables. If needed, a set of dynamic masks can be applied in order to address the shading of large sections of the detector during data collection (57); powder rings from the gasket or from Be can be removed from the collected frames in the same way. Absorption and systematic errors are treated by a two-stage procedure: first, the program SHADE (65) is used to reject

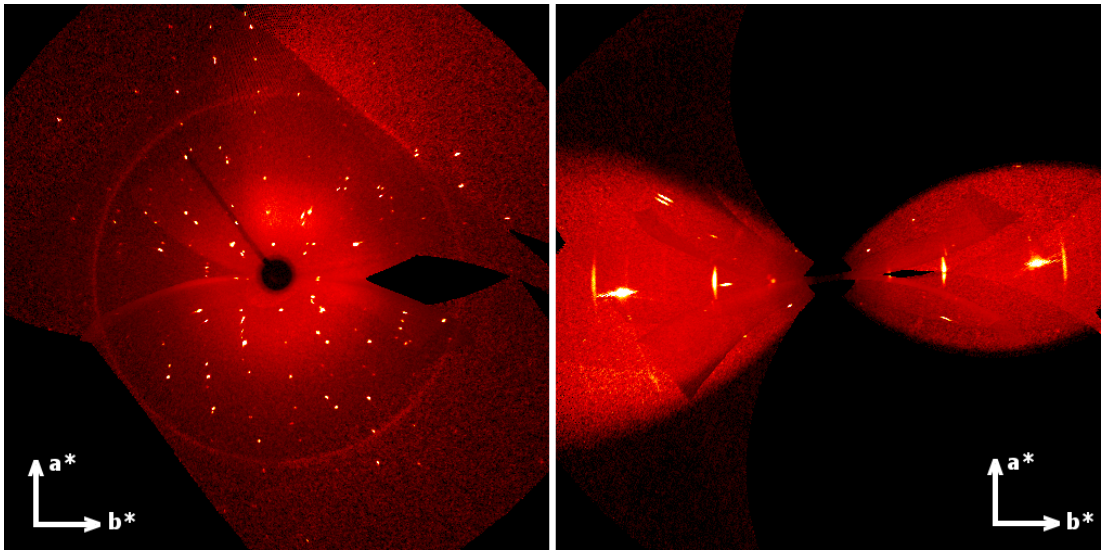

Figure 3.7: Comparison of the precession image of the *hk0* zone calculated through the APEX-II program, for an ambient pressure data collection (*left*) and for a high-pressure data set (*right*).

reflections that lie within 2° of the DAC opening angle and have poorly-resolved peak profiles; then, differences in the X-ray path length arising from the different orientations of the crystal during data-collection are corrected with the program SADABS (66). Its equivalent for twinned samples, TWINABS, (67) proved to be fundamental for the treatment of the synchrotron data of the triclinic polymorph of rubrene, as discussed in Section 5.3.

3.5 Laboratory and Synchrotron X-ray Sources

Ambient pressure X-ray diffraction experiments are in general performed using the monochromatic X-ray radiation produced by the common laboratory sealed tubes, where electrons, accelerated through an electric field, hit a metal target (usually copper or molybdenum) that produces radiation of the wavelength corresponding to the excited transition (K_α = 1.5418 Å for Cu and K_α = 0.7107 Å for Mo). At its specific wavelength, each source is capable of providing enough intensity to obtain good quality data from a classical diffraction experiment. Although high-pressure experiments on small-molecule crystals are routinely and successfully carried out using home source, the use of synchrotron radiation enables to overcome the issues of low completeness and absorption associated with the DAC. Aside from increased diffraction intensity and

hence better data resolution, the wavelength of synchrotron radiation is usually tunable: the limited portion of reciprocal space available through the opening angle of the DAC can be better accessed with a shorter wavelength. For these reason, synchrotron radiation has been essential in obtaining high-resolution single-crystal diffraction data, for the high-pressure investigation of the polymorphs of rubrene described within this work. The weak diffraction power of the investigated organic samples, in fact, limited the possibility to obtain good-quality data with a DAC. As high pressures can be reached only by using a sample chamber with the smallest possible volume, the size of the crystals to be loaded was correspondingly limited: synchrotron radiation has been thus vital for the solution and refinement of the structures of the weakly diffracting crystals contained in the DAC. These measurements were carried out at the ANKA synchrotron facility of the Karlsruhe Institute of Technology (Karlsruhe, Germany), using a 0.66100 Å wavelength.

4 | New Rubrene Derivatives

4.1 Synthesis and Chemical Properties

Following the conclusions of Chapter 2, in the frame of the research project n. 2009/2551 funded by Fondazione Cariplo, a synthetic protocol was developed to synthesize a series of novel rubrene derivatives (5,6,11,12-tetraaryltetracenes) bearing electron-withdrawing and electron-donating substituents. Our idea to take advantage of the favorable 4-position of the phenyl groups of a rubrene molecule, functionalizing it while preserving the packing motif of the orthorhombic polymorph in the solid state, is perfectly compatible with the synthetic strategy used to prepare commercial rubrene: this straightforward synthesis is based on the dimerization of 1,1,3-triaryl-3-chloro-allene (allene = propan-1,2-diene) by simple heating, as described for the first time in the 1920's and rationalized in the 1970's by Rigaudy (68). The allene is obtained from the corresponding triaryl-propargyl alcohol which can be alternatively prepared by addition of a proper organometallic reagent (*e.g.* a Grignard reagent of a arylacetylide or a lithium acetylide) on diarylketones (such as benzophenone) or by Sonogashira reaction between a 1,1-diaryl-propargyl alcohol and a halogenated aromatic compound. Both the above protocols were followed in order to minimize the chance of formation of a bis-alkylidenecyclobutene, as the dimerization of chloroallenes is always in competition with the formation of this compound.

As reported in Figure 4.1, four different derivatives were prepared following this synthetic strategy: derivatives 5,11-bis(4-nitrophenyl)-6,12-biphenyltetracene (Rub-NO_2), 5,11-bis(4-trifluoromethylphenyl)-6,12-biphenyltetracene (Rub-CF_3) and 5,11-bis(4-benzonitryl)-6,12-biphenyltetracene (Rub-CN) bear electron-withdrawing groups, while derivative 5,11-bis(3-thienyl)-6,12-biphenyltetracene (Rub-Thio) bears two electron-donating thienyl-rings. In order to study the effect of the different functionalizations on

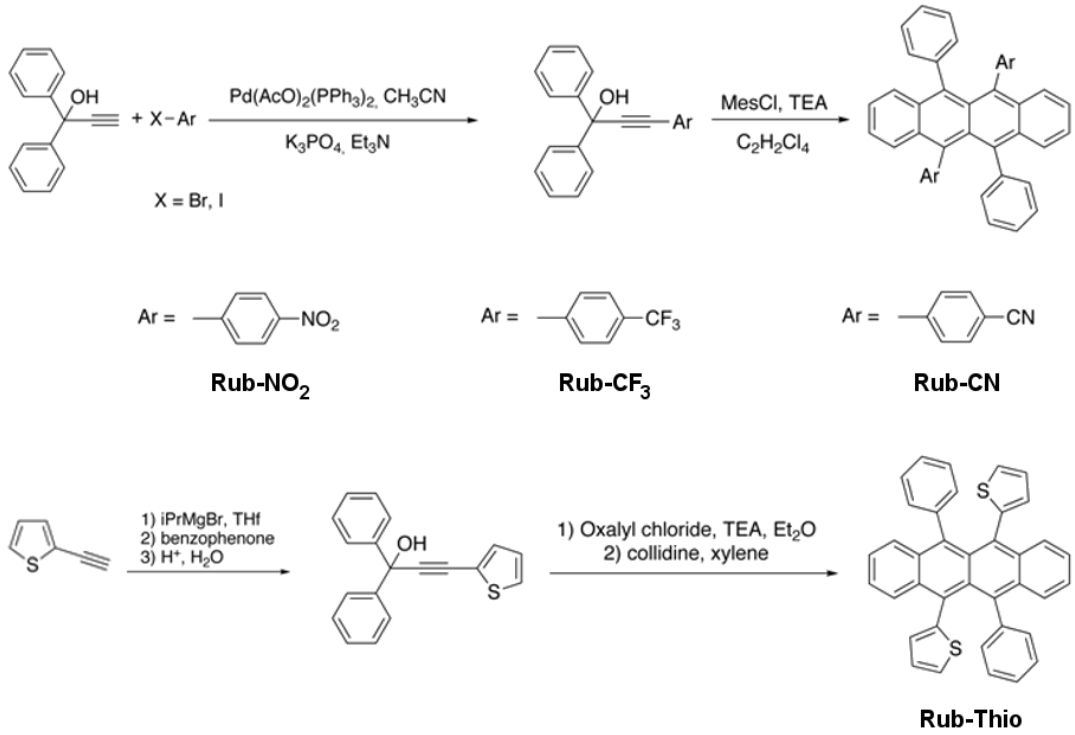

Figure 4.1: Synthesis of 5,6,11,12-tetraaryltetracenes.

the oxidation rate of the molecules, an analysis of the photooxidation of rubrene and its derivatives, in solution, was performed; due to the different electron withdrawing or donating strength of the various substituents, the reactivity toward oxygen of these molecules should vary with respect to that of rubrene. Each of the four rubrene derivatives was thus dissolved in 1,1,2,2-tetrachloro-ethane at a concentration of 2.2×10^{-4} M, and the absorption spectra in the spectral range from 2.1 to 3.6 eV were collected over several hours. The changes in the features of the absorption spectra of rubrene, during the oxidation process, have already been described in Chapter 1: the gradual reduction of the area of the multiple peaks in the 2.1 - 2.8 eV region for pristine rubrene, was similarly noticed also for the synthesized derivatives and the spectra of derivative Rub-NO_2 is reported in Figure 4.2a for a comparison with that of rubrene (see Figure 1.2e). In order to carry out a quantitative comparison, the integral area reduction was monitored as a function of exposure time; in Figure 4.2b the results of this analysis are reported for all the compounds and compared to the corresponding rubrene data. The reference value 100% represents the initial integral area, collected immediately after preparation of the solutions. The experiment was performed during a 10 h interval, that is until the percentage of relative integral area for all molecules decreases to zero. While the rubrene solution becomes colorless in less than 1 h, a

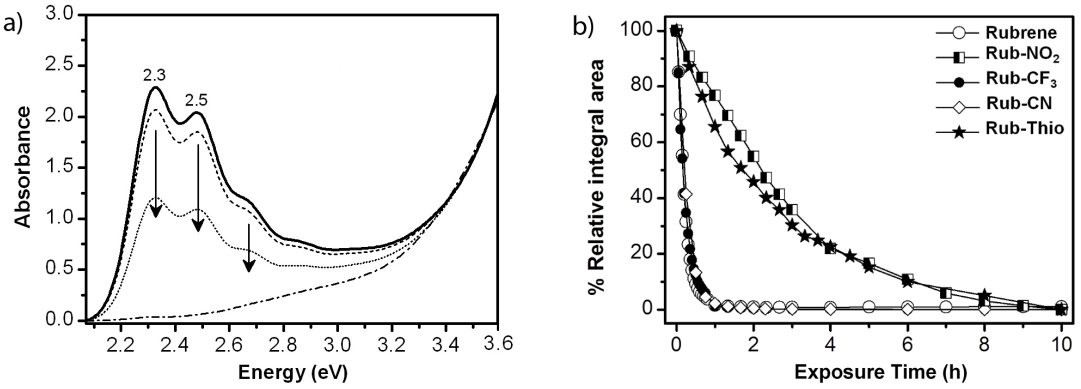

Figure 4.2: (a) Absorption spectra of a 2.2×10^{-4} M solution of Rub-NO_2 taken just after preparation (continuous line), after 20 min (dashed line), after 2 h (dotted line) and after 6 h (dashed-dotted line) of exposition to air and light. (b) Relative percentage of the area of the absorption band from 2.1 to 2.8 eV of all the solutions as a function of exposure time to air and light.

period of time from 2 to 10 h is required for all the other compounds to fully degrade,

clearly demonstrating the stabilizing effect of the substituents. The introduction of electron withdrawing groups decreases, in fact, the reactivity of aromatic compounds against electrophiles such as $^1O_2$. This common trend is maintained for all compounds bearing electron-withdrawing groups, with the highest stabilization toward oxidation observed in the case of Rub-NO_2, according to the strong electron-withdrawing character of 4-nitrophenyl groups. The behavior of Rub-Thio represents, instead, a surprising exception: its degradation rate is comparable with that of Rub-NO_2, although thiophene is usually considered an electron-donating group. For this reason, on the basis of standard models describing the reactivity of aromatic compounds, Rub-Thio should have a reactivity against $^1O_2$ even higher than rubrene: its unexpected behavior can not be rationalized in terms of electronic effects of this substituent on reactivity. An explanation can be found in a possible twisted conformation of the molecules, when in solution: these twisted isomers (69) are known to be more stable against oxidation (70), because of the loss of molecular planarity, which is related to the aromatic character of the molecule and thus with its reactivity with oxygen. A deeper insight into the reactivity toward oxygen of these novel rubrene derivatives was provided by an electrochemical characterization of the compounds in solution; cyclic voltammetry (CV) and differential pulse voltammetry (DPV) were carried out for all the synthesized molecules, since this kind of measurements give information both on oxidation potential and on the position of the HOMO level of a molecule. The oxidation potential obtained from the DPV current peak position and the HOMO values calculated by using a vacuum level of 5.23 V for the Ferrocene/Ferrocenium (Fc/Fc^+) redox couple (71) are reported in Figure 4.3 with the corresponding plot.

Once again, the values found for each of the three electron-withdrawing derivatives are in good agreement with that of pristine rubrene, also in good accordance with previously reported values in similar electrolyte solution (72): the nitro, trifluoromethyl, and nitrile derivatives display higher oxidation potential and lower-energy HOMO level than rubrene itself. Although this is perfectly expected from the electron-withdrawing character of the three compounds, the high oxidation potential of Rub-CF_3 and Rub-CN corresponds to a reactivity toward oxygen which is more similar to that of rubrene than that of Rub-NO_2 (see Figure 4.2b); therefore, the comparison between electrochemical and photooxidation reactivity clearly demonstrates that these two parameters are not correlated. A further proof of this claim is the even more surprising behavior of

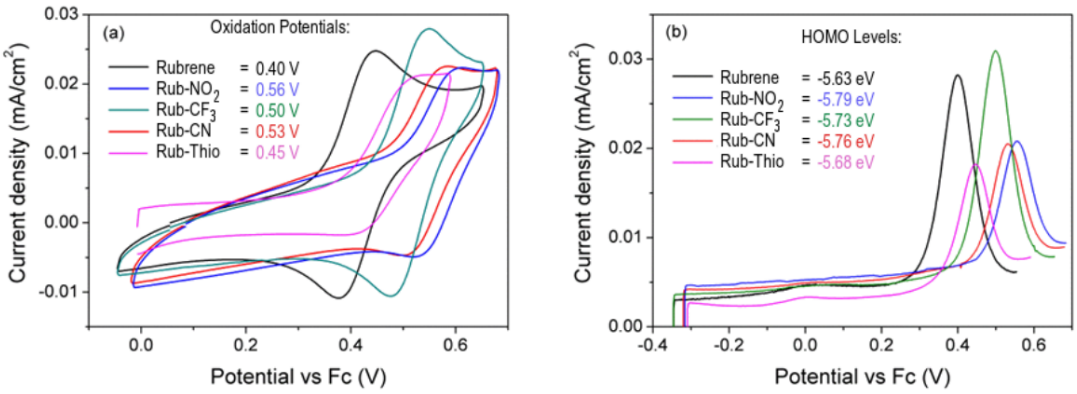

Figure 4.3: CV traces with corresponding oxidation potentials (*left*) and DPV curves with corresponding HOMO levels (*right*) of the different rubrene derivatives dissolved (concentration about 10^{-4} M) in the supporting electrolyte, a 0.1 M solution of tetrabutylammonium perchlorate ($TBAClO_4$) in a 2:1 mixture of dichloromethane and acetonitrile

Rub-Thio: this derivative also has an oxidation potential slightly higher than pristine rubrene, despite the donor character of the electron rich heteroaromatic ring. A corresponding higher HOMO level should be thus expected, if compared with that of rubrene (-5.63 eV), while a HOMO level of -5.68 eV is found. This behavior could be explained considering that both rubrene and thiophene are good donor systems and an internal charge transfer process can not be excluded in solution. In this case, the thiophene molecular orbital may contribute to the molecular HOMO orbital and the resulting oxidation potential would be increased to an intermediate value between the oxidation potentials of rubrene and thiophene itself, around 1.2 V vs. ferrocene. In order to verify this hypothesis and the possibility to have a stabilizing effect toward oxidation originated from the twisting of the molecules of Rub-Thio in solution, HOMO/LUMO wavefunction and molecular dynamics calculations of the isolated molecule conformations are needed for all the synthesized rubrene derivatives.

4.2 Crystal Structures of Rubrene Derivatives

This selection of rubrene derivatives, displaying different stability and reactivity toward oxygen, provided the opportunity to test the dependence of rubrene transport properties on the chemical properties of the single molecule. The preservation of the packing motif of orthorhombic rubrene in the solid state is mandatory for the coher-

ence of this analysis, therefore it was necessary to grow single crystals from the whole series of rubrene derivatives in order to check their crystal structure. All data collections were performed on a Rigaku R-Axis II diffractometer equipped with a SHINE graphite monochromator (MoKα radiation λ= 0.71075 Å) and a curved image plate detector. The collected intensities were corrected for Lorentz, polarization factors and absorption using CrystalClear-SM Expert 2.0 suite of programs. The structures were solved by direct methods using SHELXS (73) and refined by full-matrix least-squares against F_o^2 using the ShelXle graphical user interface for SHELXL-2013 (74). Crystals growth conditions and crystallographic data will be reported here for each compound in an independent subsection. Because of the almost total isostructurality of the crystal structures of interest, a more exhaustive comparison of the whole set of derivatives crystal structures will be reported separately in Section 4.3. For each of them, those structural parameters which have a fundamental relationship with the transport properties of the material and whose importance has been already stressed in Chapter 1 for orthorhombic rubrene, will be explicitly taken into account and compared within that section.

4.2.1 Rub-NO_2 (5,11-bis(4-nitrophenyl)-6,12-biphenyltetracene)

The excellent stability of Rub-NO_2 toward oxidation and its improved solubility in common organic solvent with respect to rubrene, suggested the possibility to grow single crystals of proper dimensions by means of solution methods. For this reason, a series of test-crystallization experiments was performed, exploring the effect that different solvents - displaying thus different volatility, polarity and solvation power - have on the growth process. Saturated solutions of Rub-NO_2 in a number of solvents were prepared, and slow evaporation experiments were carried out in isothermal conditions. Red-colored crystals were grown from pure dichloromethane and acetone; some single crystals were selected and measured. The crystal structure of the parallelogram-shaped crystals grown from CH_2Cl_2 is reported in Figure 4.4a: a solvate was obtained, where eight molecules of Rub-NO_2 share the unit cell with four molecules of solvent.

The same solvate structure was obtained also from the needle-like crystals grown from acetone: this second structure, depicted in Figure 4.4b, is in fact perfectly superimposable with the previous one. In these two structures, a single molecule of solvent (either CH_2Cl_2 or acetone) shares the asymmetric unit with two molecules of Rub-NO_2,

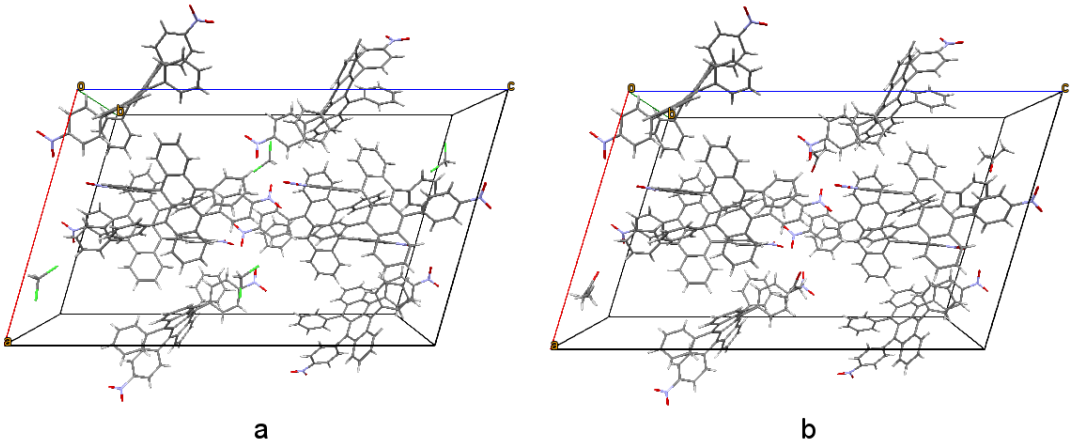

Figure 4.4: Perspective view of the crystal structure of the Rub-$NO_2 \cdot {}^1/_2(CH_2Cl_2)$ solvate (*a*) and of the the Rub-$NO_2 \cdot {}^1/_2$(acetone) solvate (*b*).

displaying a huge twisting of the tetracene core. The torsion angle among the two external C-C bonds that define the short edges of the tetracene and describes the twisting, is not the same for the two independent molecule: in one case the torsion angle is *ca.* 35°, while in the other is *ca.* 46°, although the light red color of the crystal suggests that the delocalization of the system is preserved. This phenomenon was already reported to occur for some of the rubrene derivatives described in Chapter 2 and the solvate structures here described seem to support the idea that rubrene molecules assume twisted conformations when in solution, in some of the cases maintaining this conformation also in the solid state (26). Detailed structural parameters are reported for the two collected structures in Table 4.1. Within the aim of this work, the obtained solvate structures are of scarce interest and for this reason only a preliminary data collection was performed on the crystals obtained.

By reducing the evaporation rate of the acetone solution, red-colored, pseudo-hexagonal shaped crystals were obtained, displaying the same crystal habit experimentally found for orthorhombic rubrene (75). The corresponding crystal structure (space group $P2_1/c$) is depicted in Figure 4.5: acetone molecules are no longer included in the structure and the tetracene cores of Rub-NO_2 moieties are perfectly planar. The same monoclinic structure was also found measuring single crystals grown by reduced pressure sublimation, choosing a pressure of $5.5{\times}10^{-2}$ mbar and the following set of temperatures (see Figure 3.2): T1 = 300 °C, T2 = 280 °C, T3 = 220 °C.

Table 4.1: Unit-cell parameters and crystal data for the two solvate structures of rubrene derivative Rub-NO_2

	Dichloromethane solvate	Acetone solvate
Moiety formula	$(C_{42}H_{26}N_2O_4)\cdot(C_{0.5}HCl)$	$(C_{42}H_{26}N_2O_4)\cdot(CH_3C_{0.5}O_{0.5})$
Cell setting	Monoclinic	Monoclinic
Space group	$P2_1/c$	$P2_1/c$
a/Å	19.4515(5)	19.6269(6)
b/Å	10.8544(2)	11.0823(3)
c/Å	31.503(1)	31.648(1)
β/°	105.975(1)	106.817(1)
Volume/Å^3	6394.5(3)	6589.4(3)
Z	8	8
Z'	2	2
Crystal color/shape	Light red parallelogram	Light red needle
Size/mm^3	0.05×0.20×0.20	0.4×0.12×0.23
T/K	130	273
$R[F^2>2\sigma(F^2)]$	0.162	0.226

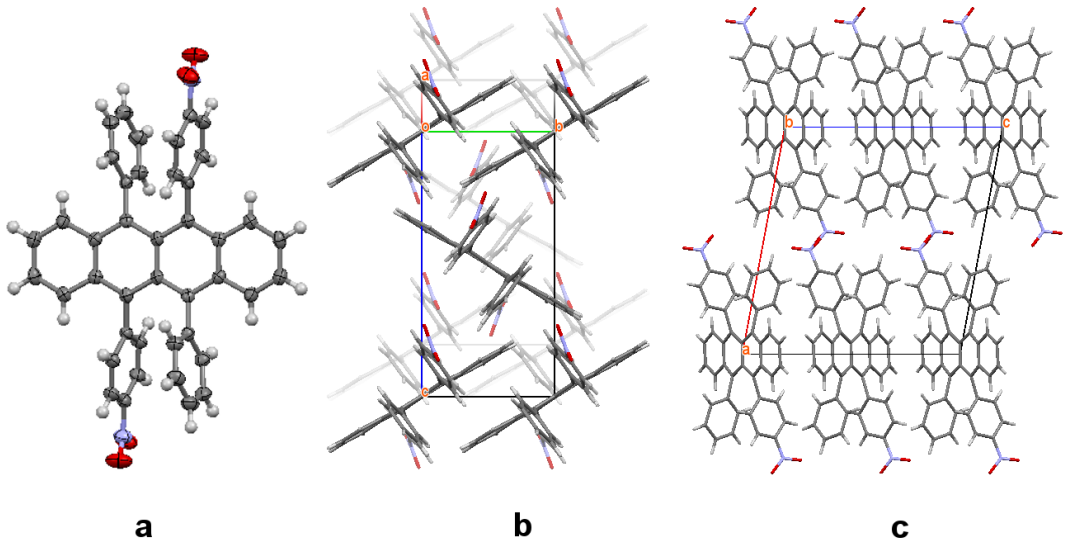

Figure 4.5: ORTEP model of derivative Rub-NO_2 (a) and crystal structure of its monoclinic polymorph, viewed perpendicularly to (100) plane (b) and along [001] (c).

Single crystals of a second triclinic polymorph were obtained by using the same method, but applying a different temperature gradient: T1 = 320 °C, T2 = 280 °C, T3 = 195 °C. The corresponding crystal structure (space group $P\bar{1}$) is depicted in Figure 4.6 while detailed structural parameters of both the identified polymorphs are reported in Table 4.2.

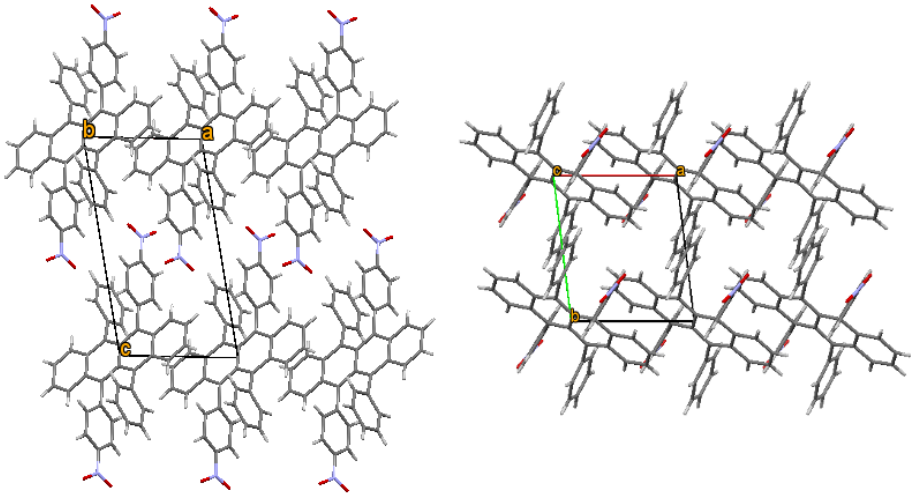

Figure 4.6: Crystal structure of the triclinic polymorph of Rub-NO_2, viewed along [010] (*left*) and [001] (*right*).

4.2.2 Rub-CF_3 (5,11-bis(4-trifluoromethylphenyl)-6,12-biphenyltetracene)

Rub-CF_3 displays, as already mentioned, a stability toward oxidation only slightly superior to that of rubrene; in addition, the introduced functionalities do not seem to have have significantly improved the solubility of the molecule in common organic solvents. For this reason solution methods proved to be inadequate to grow good quality single crystals, yielding mainly amorphous material and colorless oxidized polycrystalline powder, regardless of the choice of the solvent. By reduced pressure sublimation, it was instead possible to obtain a few good quality orange crystals, displaying the same pseudo-hexagonal crystal habit already seen for the Rub-NO_2 crystals grown with the same technique. The optimized growth conditions were found at a pressure 4.0×10^{-2} mbar, for the following set of temperatures: T1 = 280 °C, T2 = 250 °C, T3 = 210 °C. The corresponding crystal structure (space group $P2_1/c$) is depicted in Figure 4.7.

Table 4.2: Unit-cell parameters and crystal data for the structures of the two polymorphs of rubrene derivative Rub-NO_2

Rub-NO_2	Polymorph I	Polymorph II
Moiety formula	$C_{42}H_{26}N_2O_4$	$C_{42}H_{26}N_2O_4$
Molecular weight	622.65	622.65
Cell setting	Monoclinic	Triclinic
Space group	$P2_1/c$	$P\bar{1}$
a/Å	15.0983(3)	7.1523(2)
b/Å	7.1706(2)	8.3744(3)
c/Å	14.2489(5)	13.2765(4)
α/°	90	88.418(6)
β/°	100.616(1)	79.243(5)
γ/°	90	82.808(5)
Volume/Å^3	1516.24(1)	775.08(4)
V_{mol}/Å^3	758.12	775.08
Density/g cm^{-3}	1.364	1.334
Z	2	1
Z'	0.5	0.5
Crystal color/shape	Pseudo-hexagonal red platelet	Red parallelogram
Size/mm^3	0.25×0.20×0.12	0.20×0.20×0.20
T/K	153	293
$R[F^2>2\sigma(F^2)]$	0.0673	0.0964

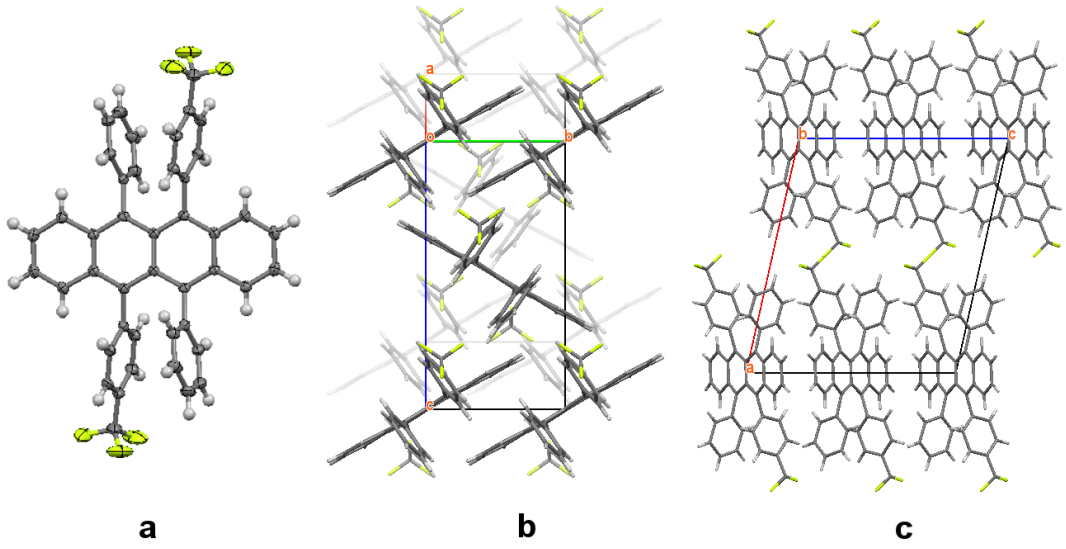

Figure 4.7: ORTEP model of derivative Rub-CF_3 (a) and crystal structure of its monoclinic polymorph, viewed perpendicularly to (100) plane (b) and along [001] (c).

Also in this case, single crystals of a second triclinic polymorph were obtained by using the same method and modifying the applied temperature gradient: T1 = 280 °C, T2 = 200 °C, T3 = 160 °C. The corresponding crystal structure (space group $P\bar{1}$) is depicted in Figure 4.8: the trifluoromethyl groups appear disordered over two positions, with site occupancies 0.52/0.48(1). Detailed structural parameters of both the identified polymorphs are reported in Table 4.3.

4.2.3 Rub-CN (5,11-bis(4-benzonitryl)-6,12-biphenyltetracene

Similarly to Rub-CF_3, Rub-CN is expected to oxidize with a rate comparable to that of pristine rubrene on the basis of the previous characterizations, but, unlikely the trifluoromethyl derivative, the solubility displayed by Rub-CN seems to be improved by the presence of the two nitrile groups. It was hence possible to grow single crystals by slow evaporation of saturated acetone solution properly maintained in dark conditions, in order to reduce the oxidation rate of the solution itself. Dark-red crystals with a pseudo-hexagonal habit were selected and measured: the corresponding crystal structure (space group $P2_1/c$) is depicted in Figure 4.9 and does not display any solvent inclusion.

In order to obtain better quality crystals, reduced pressure sublimation experiments were also performed and the optimized conditions that yield to the growth of the most

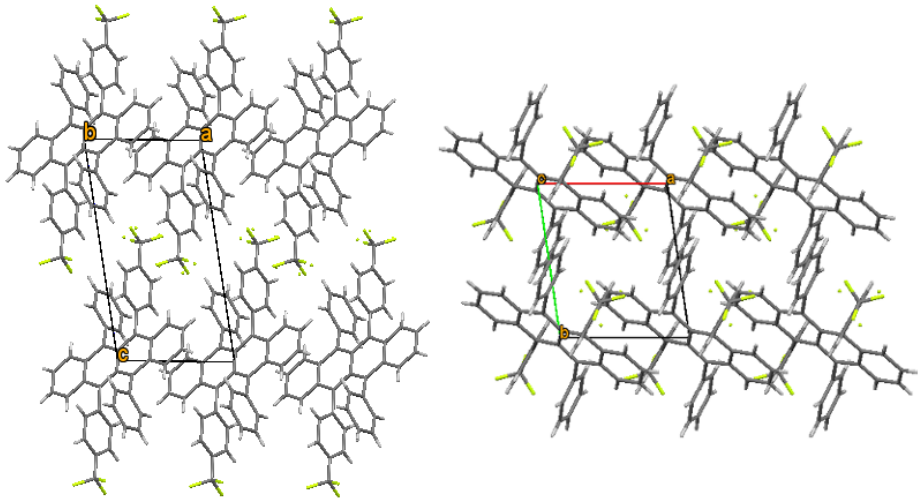

Figure 4.8: Crystal structure of the triclinic polymorph of Rub-CF_3, viewed along [010] (*left*) and [001] (*right*).

Table 4.3: Unit-cell parameters and crystal data for the structures of the two polymorphs of rubrene derivative Rub-CF_3

Rub-CF_3	Polymorph I	Polymorph II
Moiety formula	$C_{44}H_{26}F_6$	$C_{44}H_{26}F_6$
Molecular weight	668.65	668.65
Cell setting	Monoclinic	Triclinic
Space group	$P2_1/c$	$P\bar{1}$
a/Å	15.9782(6)	7.0901(2)
b/Å	7.2762(2)	8.4050(4)
c/Å	13.9814(6)	13.4466(7)
α/°	90	88.303(8)
β/°	102.701(2)	80.563(7)
γ/°	90	81.540(6)
Volume/Å^3	1585.7(1)	781.86(6)
V_{mol}/Å^3	792.85	781.86
Density/g cm^{-3}	1.400	1.420
Z	2	1
Z'	0.5	0.5
Crystal color/shape	Pseudo-hexagonal orange platelet	Orange parallelogram
Size/mm^3	0.35×0.28×0.10	0.40×0.10×0.10
T/K	123	123
$R[F^2>2\sigma(F^2)]$	0.0659	0.0937

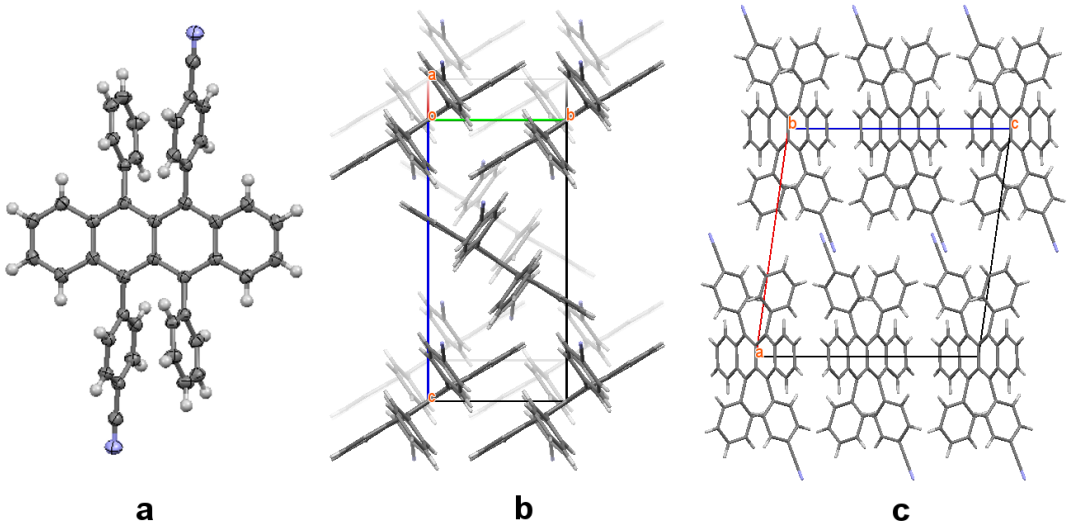

Figure 4.9: ORTEP model of derivative Rub-CN (*a*) and correspondent crystal structure, viewed perpendicularly to (100) plane (*b*) and along [001] (*c*).

promising crystalline individuals are the following: T1 = 280 °C, T2 = 250 °C, T3 = 220 °C, with a pressure of 3.0×10^{-2} mbar. Unlike the previously described rubrene derivatives, for Rub-CN it was not possible to identify the growth conditions of any other polymorph, apart from the described monoclinic one, whose detailed structural parameters are reported in the first column of Table 4.4.

4.2.4 Rub-Thio (5,11-bis(3-thienyl)-6,12-biphenyltetracene

During the preliminary purification of Rub-Thio by column chromatography, several single crystals with different colors and habits were obtained, by slow evaporation of a hexane/ethyl acetate 9:1 solution. Single-crystal X-ray diffraction data collections performed on these samples revealed, in addition to the presence of cyclobutene, the formation of a number of additional side-products: thanks to the identification of these compounds, it was possible to update the reaction mechanism proposed by Rigaudy (68). An improved version of this reaction mechanism, accounting for the formation of the identified compounds, is reported in Appendix A, together with crystallographic data for each of them, in Table A.1. Light red pseudo-hexagonal crystals were separated from the others by hand and cleared from impurities by dissolution and recrystallization, by slow evaporation from an acetone solution. Finally, good quality single crystals were

isolated and measured: the corresponding crystal structure (space group $P2_1/c$) is depicted in Figure 4.10 and does not display any solvent inclusion. The who thienyl rings appear disordered over to positions, with occupancies 0.784/0.216(3).

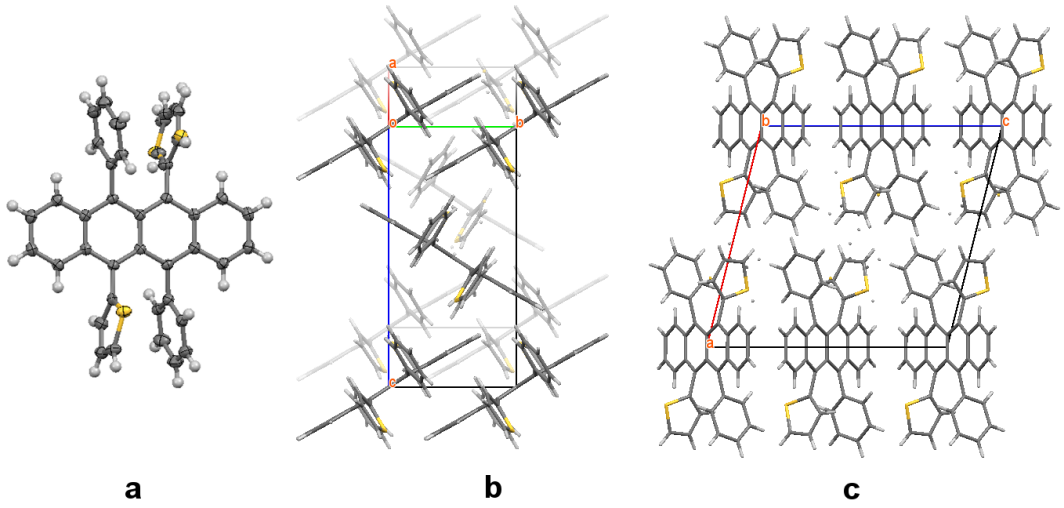

Figure 4.10: ORTEP model of derivative Rub-Thio (a) and correspondent crystal structure, viewed perpendicularly to (100) plane (b) and along [001] (c).

Detailed structural parameters are reported in the second column of Table 4.4. Any attempt to grow single crystals of the proper size and quality by reduced pressure sublimation was unsuccessful.

4.3 Structure Comparisons

Focusing on the aim of this work - verifying the possibility to obtain new rubrene derivatives with improved chemical properties and unaltered crystal packing in the solid state - the obtained monoclinic structures have been compared in detail. The four structures appear visually identical, displaying the same crystallographic symmetry and adopting the space group $P2_1/c$; this allows an easy comparison of all the individual structural parameters. The most important feature of all these crystal structures is the herringbone disposition of the molecules in the (100) layer, involving the long axis of the tetracene: the aromatic cores of adjacent molecules are facing each other and π-stacking along the b direction of the monoclinic cell, without any evidence of a short

Table 4.4: Unit-cell parameters and crystal data for the structures of rubrene derivatives Rub-CN and Rub-Thio

	Rub-CN	Rub-Thio
Moiety formula	$C_{44}H_{26}N_2$	$C_{38}H_{24}S_2$
Molecular weight	582.67	544.71
Cell setting	Monoclinic	Monoclinic
Space group	$P2_1/c$	$P2_1/c$
a/Å	14.9125(6)	13.5679(5)
b/Å	7.1151(2)	7.0143(2)
c/Å	14.4263(4)	14.3020(7)
β/°	98.099(2)	103.954(2)
Volume/Å^3	1515.42(9)	1320.94(9)
V_{mol}/Å^3	757.71	660.47
Density/g cm^{-3}	1.277	1.370
Z	2	2
Z'	0.5	0.5
Crystal color/shape	Pseudo-hexagonal dark red platelet	Pseudo-hexagonal red platelet
Size/mm^3	0.34×0.34×0.06	0.35×0.14×0.10
T/K	123	123
$R[F^2>2\sigma(F^2)]$	0.0665	0.0687

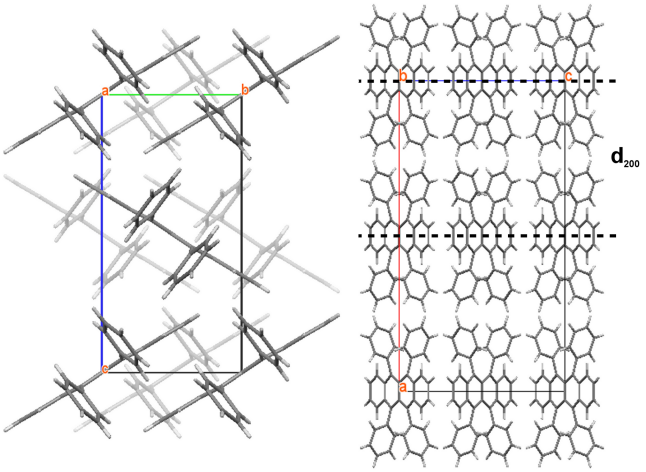

Figure 4.11: [100] view (*left*) and [010] view (*right*) of the packing motif of orthorhombic rubrene: the thickness of the d_{200} is reported for clarity.

axis displacement. This packing motif is identical to the one found in the (200) layer of orthorhombic rubrene, which is depicted in Figure 4.11: this means that the different chemical modifications, introduced on 4-position of two of the phenyl groups in the rubrene molecule, leave almost unaltered the favorable $\pi - \pi$ in-plane intermolecular contacts, allowing confinement of the substituents at both surfaces of the (100) layer.

Analysis of inter- and intra-molecular parameters of the derivatives, reported in Table 4.5, evidences that the packing features closely resemble those of orthorhombic rubrene. The parameters of orthorhombic rubrene are also reported in the first column of Table 4.5 for the data set closest in temperature (CSD Refcode: QQQCIG05), so that a more accurate comparison can be made. In the orthorhombic structure of rubrene, the $\pi - \pi$ stacking distance among the tetracene cores of adjacent molecules is 3.67 Å, with a herringbone angle of 61.49°. For all our derivatives, both the $\pi - \pi$ stacking distance and the width of the herringbone angle are slightly smaller than in rubrene. While in rubrene the herringbone layer is d_{200} and corresponds to half the a cell parameter, with a thickness of 13.39 Å (see Figure 4.11), the elementary layer for the monoclinic structures of all derivatives is d_{100}.

As depicted in Figure 4.12, the thickness of d_{100} changes with the nature of the substituents since it must accommodate the protruding moieties, sandwiching them between adjacent layers. The smallest value for d_{100}, even smaller than in rubrene, is displayed by derivative Rub-Thio, owing to the presence of the small five-membered thienyl rings: for this derivative, in fact, the unit-cell volume is sensibly lower than for the others. On the contrary, to accommodate the bulky trifluoromethyl substituent of

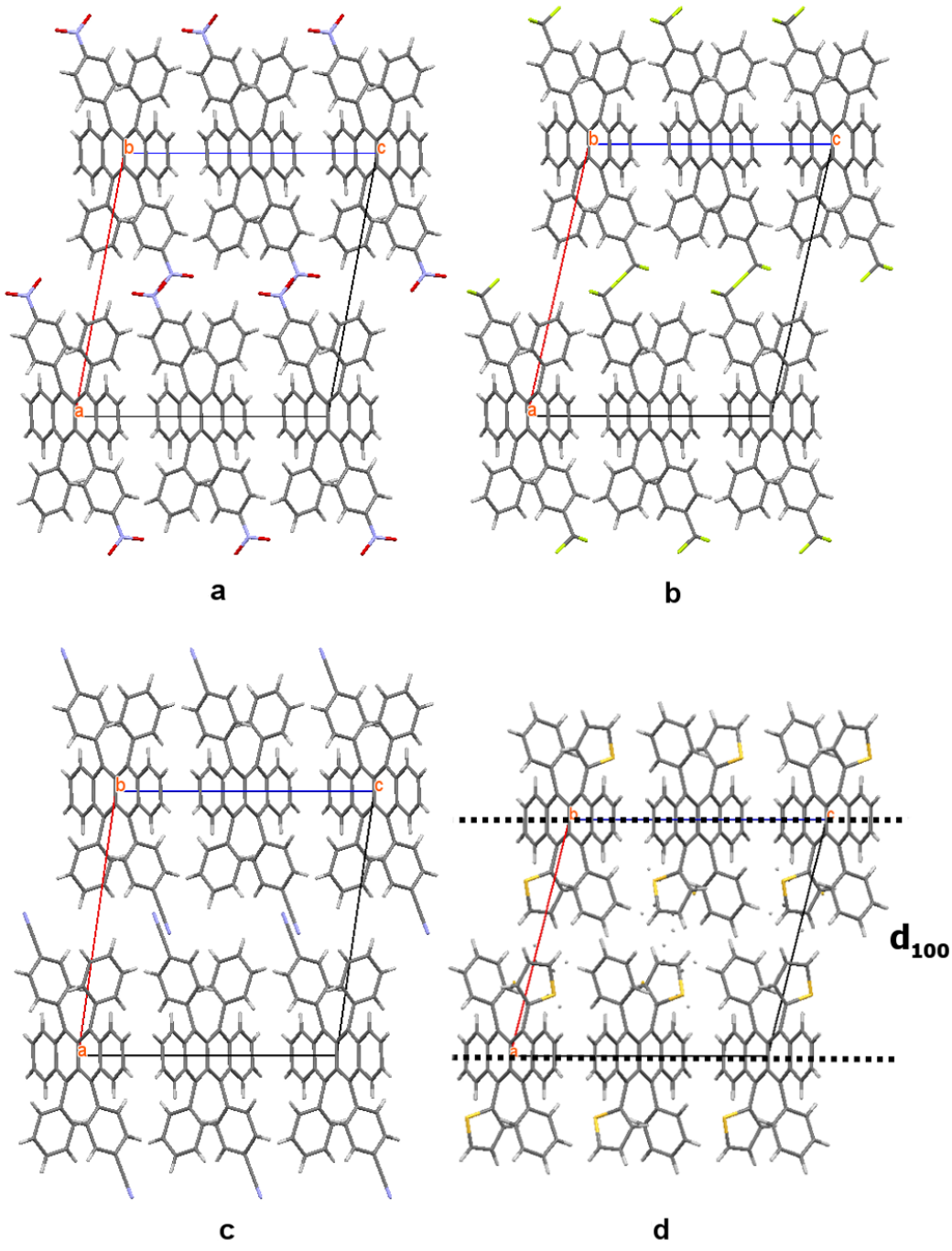

Figure 4.12: Packing motif of tetraaryltetracenes viewed along [010]: Rub-NO_2 (*a*), Rub-CF_3 (*b*), Rub-CN (*c*) and Rub-Thio (*d*); the thickness of the d_{100} layer is reported for clarity only for Rub-Thio.

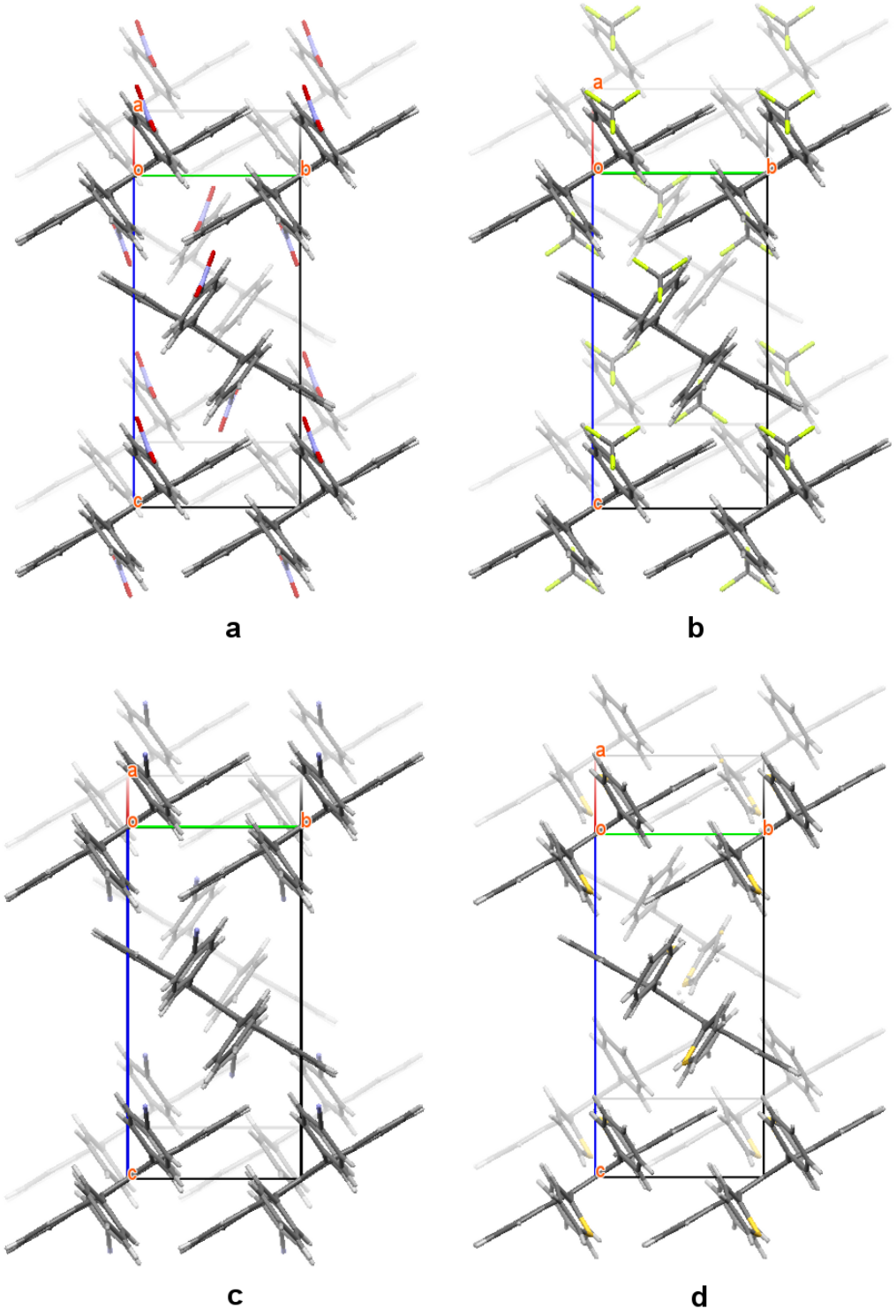

Figure 4.13: Packing motif of tetraaryltetracenes viewed along [100]: Rub-NO_2 (*a*), Rub-CF_3 (*b*), Rub-CN (*c*) and Rub-Thio (*d*).

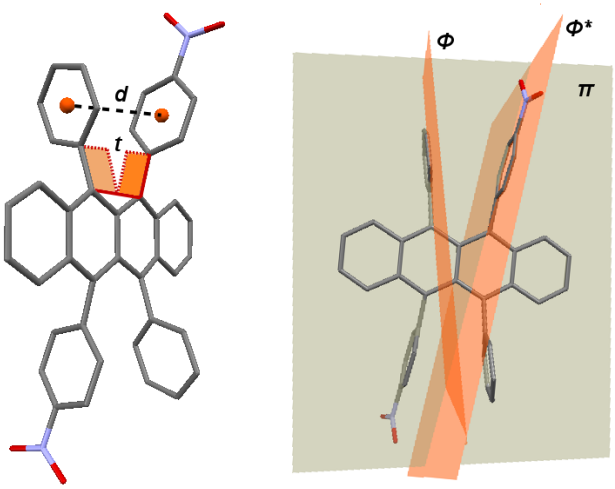

Figure 4.14: Description of the calculated intramolecular parameters: centroid distance d, phenyls torsion angle t, tetracene plane π, phenyl plane ϕ and substituted phenyl plane ϕ^*.

derivative Rub-CF_3, the widest separation of adjacent layers in the series is observed. Also the monoclinic β angle is affected by the nature of the substituents, since β is determined by the shift occurring along the c axis, necessary for the stacking of adjacent d_{100} layers, depicted in Figure 4.13; in orthorhombic rubrene such a shift occurs along the b axis and corresponds to half the unit-cell parameter. The length of the b and c axes of our derivatives are, instead, much more similar to each other and to those of orthorhombic rubrene. Calculation of selected intramolecular geometrical parameters has been performed for all derivatives, in order to verify any relationships with the electron withdrawing or donating character of the substituted rings. With this aim, we report in Table 4.5 the width of the dihedral angle between the planes of the substituted phenyl ring and that of the adjacent unsubstituted one, the torsion angle among the C-C *peri*-bonds connecting each of the two phenyls to the tetracene unit, the distance among their centroids, and the dihedral angle described by each plane with the plane of the tetracene; the values of these parameters were also compared to the corresponding ones for orthorhombic rubrene (a graphical description of the selected parameters is reported in Figure 4.14 for clarity). It was not possible to relate any of these parameters with the electron withdrawing or donating character of the substituted ring, nor to recognize evidence of any other trend ruling the series of derivatives: this suggests that the variation of these parameters is probably related to intermolecular steric effects, originating from the crystal packing. Moreover, the introduction of the different functionalities does not seem to affect the planarity of the tetracene cores (also reported in Table 4.5 as the

Root Mean Square - RMS - deviation from planarity of the 18 atoms comprising the tetracene), comparable to that of rubrene. This is expected since the tight herringbone packing is quite demanding in terms of close contacts between adjacent tetracene cores.

For Rub-NO_2 and Rub-CF_3, the structure of the obtained triclinic crystals show the same level of similarity with the structure of the triclinc polymorph of rubrene. Given the limited amount of information available in the literature for the properties of this polymorph, a full structural and electrical characterization of the obtained crystals has not been performed and represents one of the possible future development of the present work.

4.3.1 Hirshfeld Surface Analysis

In order to quantify the degree of similarity between the orthorhombic structure of pristine rubrene and the monoclinic structures of the synthesized rubrene derivatives, the Hirshfeld surface analysis presented in Chapter 2 and already performed on the polymorphs of rubrene and on its available derivatives, was extended to our novel derivatives. For each of them, the normalized contact distance d_{norm}, defined in Section 2.1, is plotted onto the corresponding HS and depicted in Figure 4.15. Some minor differences among them are clearly visible, for example in the shape assumed by the HS around each kind of substituent on the phenyl rings, or in the position of the short-contacts involving their atoms; however, it is also evident that the flat blueish region, corresponding to the π-stacking of the tetracene cores of the molecules, is always present with small differences.

The 2D-fingerprint plot was also calculated for every single derivative and it is depicted in Figure 4.16. Here again, each of them displays unique features, due to the different contacts in the region of the 4-position substituents which involve, respectively, nitrogen and oxygen atoms in Rub-NO_2, carbon e fluorine atoms in Rub-CF_3, carbon and nitrogen atoms in Rub-CN and the sulfur atoms of the thienyl rings of Rub-Thio. In the bottom left corner of the plot, for example, where the closest intermolecular contacts are located, it is possible to distinguish the single central spike corresponding to $H\cdots H$ short contacts, between one of the hydrogens on the short edge of the tetracene and one of the *ortho*-hydrogen atoms of the unsubstituted phenyl ring. The interaction between the *para*-hydrogen atom of an unsubstituted phenyl ring and one of the oxygen atoms of Rub-NO_2 - or one of the nitrogen atoms of Rub-CN - is described on the plot by a

Table 4.5: Comparison between the structural parameters of rubrene and of all the derivatives

	Rubrene (QQQCIG05)	Rub-NO_2	Rub-CF_3	Rub-CN	Rub-Thio
T/K	125	150	120	253	253
Cell setting	Orthorhombic	Monoclinic	Monoclinic	Monoclinic	Monoclinic
Space group	*Cmca*	$P2_1/c$	$P2_1/c$	$P2_1/c$	$P2_1/c$
a/Å	26.789(4)	15.0983(3)	15.9782(6)	14.9125(6)	13.5689(5)
b/Å	7.173(1)	7.1706(2)	7.2762(2)	7.1151(2)	7.0143(2)
c/Å	14.246(2)	14.2489(5)	13.9814(6)	14.4263(4)	14.3020(7)
β/ °	-	100.616(1)	102.701(2)	98.099(2)	103.954(2)
Volume/Å^3	2737.48	1516.24(1)	1585.71(1)	1515.42(9)	1320.94(9)
Z/Z'	4/0.25	2/0.5	2/0.5	2/0.5	2/0.5
d_{100} thickness†/Å	13.39	14.84	15.59	14.76	13.17
$d_{\pi-\pi}$ stacking†/Å	3.67	3.58	3.53	3.63	3.53
Herringbone angle/°	61.49	59.97(2)	58.04(1)	61.35(1)	60.46(2)
Planarity RMS	0.033	0.036(2)	0.036(2)	0.034(2)	0.034(2)
$\phi - \phi^*$ Torsion angle†/°	24.65	27.5	26.3	26.6	21.8
$\phi - \phi^*$ Opening angle/°	25.36	19.39(4)	20.27(4)	18.98(4)	22.43(2)
$\phi - \phi^*$ Centroids distance†/Å	3.545	3.477	3.479	3.471	3.513
$\phi - \pi$ Dihedral angle/°	80.30	81.90(2)	81.76(2)	84.47(2)	85.67(6)
$\phi^* - \pi$ Dihedral angle/°	80.30	83.21(2)	82.35(2)	84.35(2)	87.3(3)

† esd are not given for the value of the parameters calculated by means of the Mercury 3.1 software.

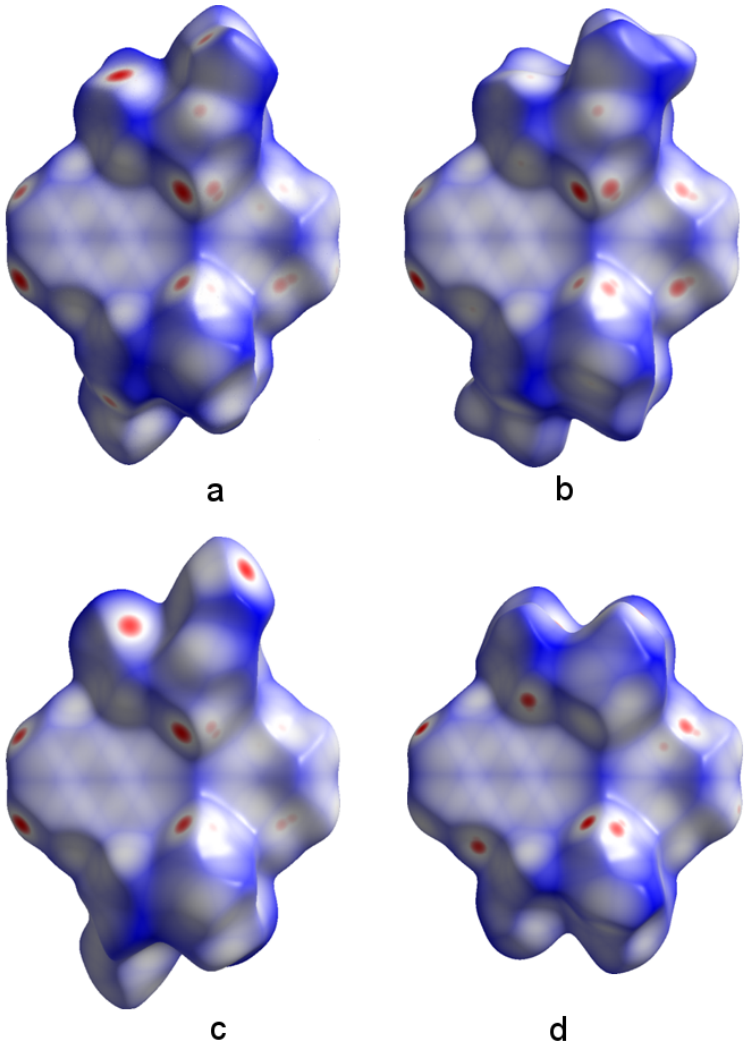

Figure 4.15: Normalized contact distance d_{norm}, plotted on the HS of Rub-NO_2 (a), Rub-CF_3 (b), Rub-CN (c) and Rub-Thio (d)

Table 4.6: Comparison between the C-C contacts area percentage and corresponding HS area involved in the $\pi \cdots \pi$ interaction, for all the derivatives

	Rub-NO_2	Rub-CF_3	Rub-CN	Rub-Thio
C-C %	5.7	5.4	6.1	6.9
$A_{\pi-\pi}$/ Å^3	32.53	32.06	34.93	35.28

couple of symmetric spikes on both sides of the central one at low d_i, d_e values, which are absent in the FP for Rub-CF_3 and Rub-Thio. Between 1.8 and 2.0 Å, however, the central green colored area present in the FP of every derivative, is the typical feature indicating a $\pi \cdots \pi$ interaction. As our analysis needs to be focused on C$\cdots$C contacts, which are associated to the π-stacking of the tetracene cores of the molecules within each structure, a necessary condition for the semiconducting properties of the material (40), C$\cdots$C contacts have been isolated and highlighted in Figure 4.17, both on the HSs and on the FPs. All the derivatives display the same highlighted region in correspondence with the portion of the tetracene core, involved in the π-stacking.

The corresponding percentage of C$\cdots$C contacts is reported for each derivative in Table 4.6, together with the effective surface area involved in the $\pi \cdots \pi$ interactions ($A_{\pi-\pi}$, in Å^3). A quick comparison with the values reported in the last two columns of Table 2.1, referring to the structure of orthorhombic rubrene, suggests that the important features of its crystal packing have been fully preserved, thus confirming our crystal-engineering approach. A recent work published by McGarry *et al.* (76) further contributes to underline this aspect, as the rubrene derivatives synthesized by the authors display the structural features of orthorhombic rubrene only for two molecules out of the six presented within their work, and only when the functionalization was inserted in the 4-position of the phenyl rings.

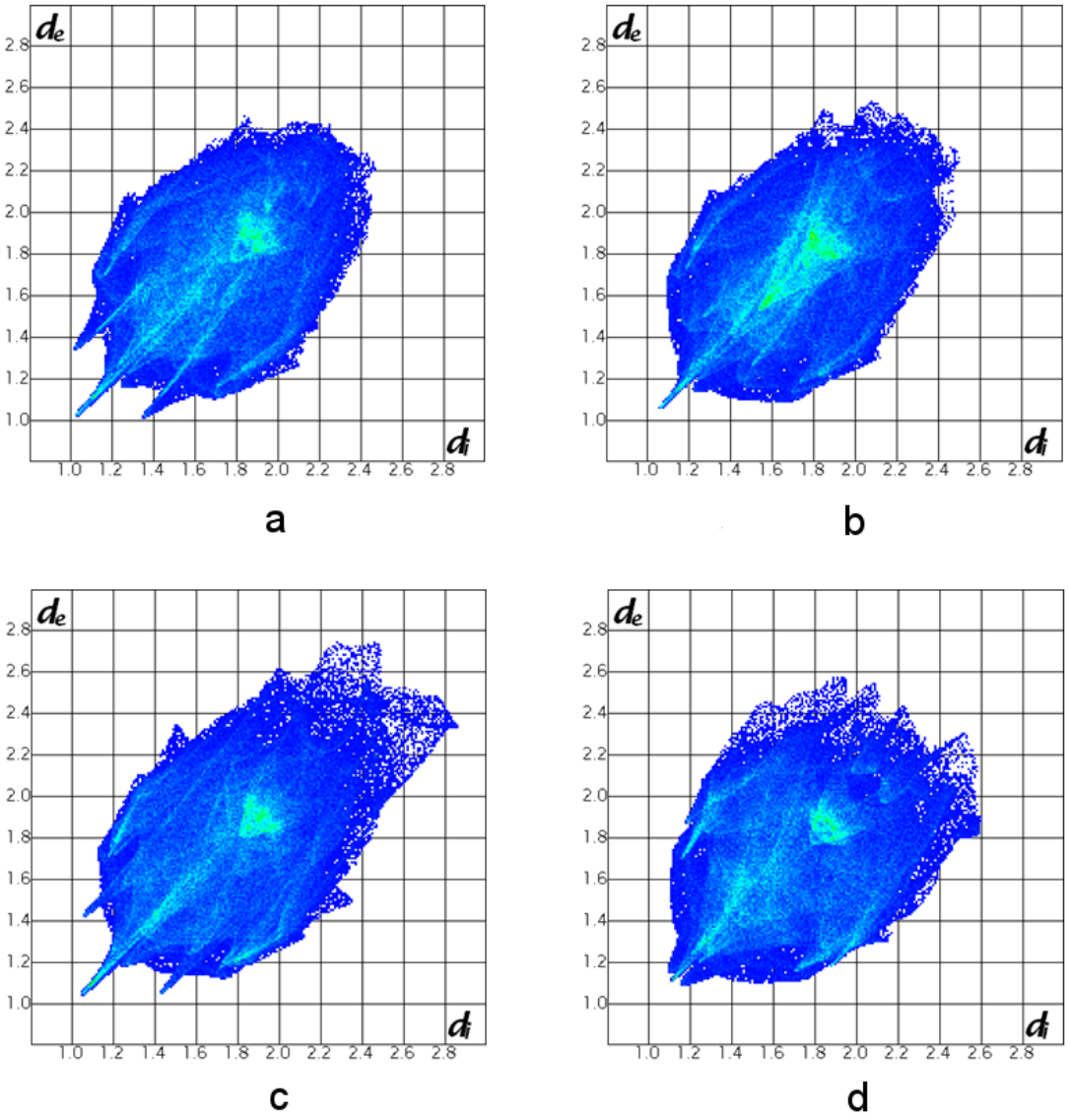

Figure 4.16: Fingerprint plot for Rub-NO_2 (*a*), Rub-CF_3 (*b*), Rub-CN (*c*) and Rub-Thio (*d*)

Figure 4.17: C···C contacts highlighted on the HS and FP of Rub-NO_2 (*a*), Rub-CF_3 (*b*), Rub-CN (*c*) and Rub-Thio (*d*).

4.4 Transport Properties

Once the monoclinic structures of the synthesized rubrene derivatives were proved to be isostructural with orthorhombic rubrene, a preliminary electrical characterization of the obtained crystal was performed. When possible, crystals grown from reduced pressure sublimation were preferred to those grown by solution methods, in order to minimize surface contamination possibly coming from impurities present in the solvent used for the crystallization. Given the small size of the selected crystals (reported in Tables 4.2 - 4.4), the study of charge transport in the solid state was performed by Conductive Atomic Force Microscopy (C-AFM). This is a contact mode AFM technique in which a conductive tip is used as an electrode, in order to apply a bias to the sample and to measure the current passing through it. C-AFM is particularly suited to study transport properties over micrometer sized crystals or smaller, even if absolute charge carrier mobility are hard to be derived (77); nonetheless, the same experimental conditions and measurement geometry was used for all the samples, so that the results for different crystals can be directly compared. The measurements are carried out keeping the tip fixed on a point on the surface of the sample: I-V curves are collected measuring the current while sweeping the potential. Given the position of the second electrode, two different configurations can be used: the vertical one, in which the electrode is placed on the back of the sample and the current thus flows in the vertical direction, and the horizontal one, in which the electrode is placed on top of the sample surface, thus probing conduction along the sample surface. This second configuration allowed us to probe the transport properties of the sample material along the b direction of the crystal structure, which corresponds both to the direction of maximum mobility for rubrene and to the direction in which π-stacking occurs for all the derivatives. The tip used for these measurements is entirely made of platinum and the second electrode has been fabricated by depositing colloidal graphite paint - known to provide particularly low contact resistance with rubrene (78) - next to one of the opposite edges and along the b lattice direction of the crystals (see Figure 4.18). This operation was carried out under an optical microscope, in order to be sure that the contact area was the same for all the samples. For all the four derivative and for an orthorhombic rubrene crystal, C-AFM has been used to collect I-V curves in the maximum bias range allowed by the instrument, i.e. from -10 to +10 V, with steps of $\sim$0.02 V. The tip was placed at a distance of

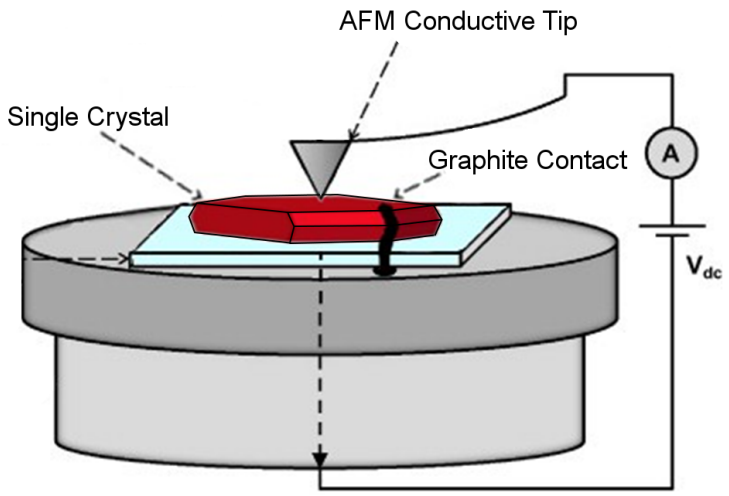

Figure 4.18: Sketch of the C-AFM apparatus, used for the measurement of the transport properties of rubrene derivatives.

$\sim$100 μm from the edge of the graphite electrode along the b direction; in order to have the same tip contact area for all the samples, the tip load was kept constant for all the measurements. The results, reported in the topmost part of Figure 4.19, show that, in the explored bias range, no measurable current can be detected for Rub-NO_2, Rub-CF_3 and Rub-CN. Non-zero current can be measured only in the case of rubrene and of derivative Rub-Thio: both of them display an asymmetric curve, due to the asymmetry between the two electrodes and to the unipolar nature of rubrenes. In particular, the larger currents measured for negative bias indicate that the tip is injecting holes into the semiconducting crystals. Maximum current values larger than 300 pA have been measured for both the semiconducting samples at -10 V bias voltage, indicating that these two materials possess similar transport properties, with much larger conductivity than the other derivatives. In the lower part of Figure 4.19 the I-V curves in log scale for rubrene and Rub-Thio are depicted: the current onset is clearly visible at about -0.5 V bias, in good agreement with the estimated values of the work function for the platinum and graphite electrodes, and for the HOMO level of rubrene and Rub-Thio.

Comparing this trend with the results of the CV measurements previously presented in Figure 4.3, a correlation between transport properties of the derivatives and their oxidation potential is clearly evident: Rub-NO_2, Rub-CF_3 and Rub-CN, which have large oxidation potential, show no current at all, while Rub-Thio, whose oxidation potential is closer to that of rubrene, shows current values comparable to those of

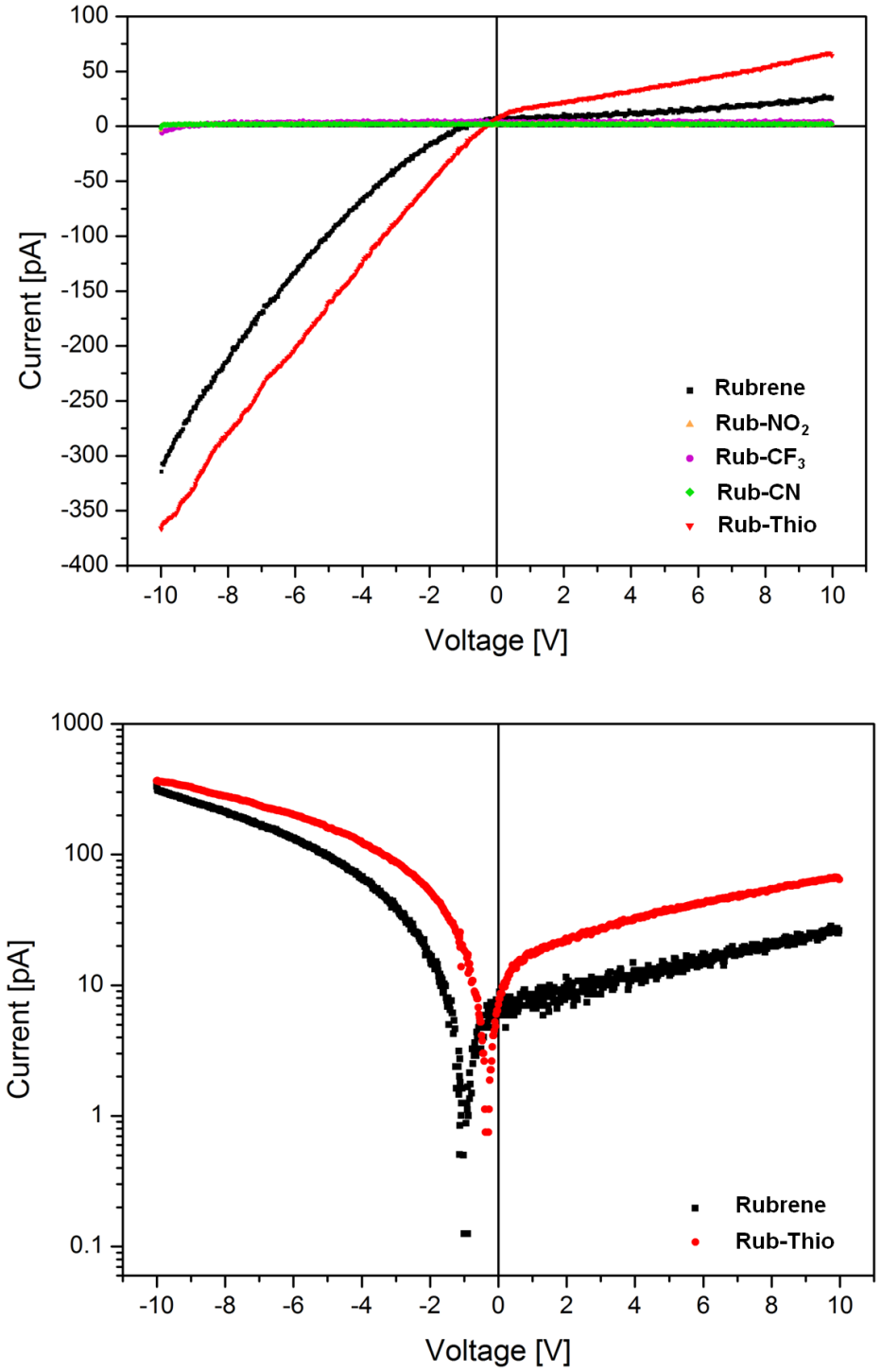

Figure 4.19: I-V curves measured by C-AFM along the *b* axis direction of rubrene and all rubrene derivatives single crystals (*top*) and curves in log scale for rubrene and Rub-Thio (*bottom*).

rubrene itself. A correlation between the C-AFM measurements and the evolution of the absorption spectra of the derivatives, instead, is not clear: if Rub-NO_2 and Rub-Thio seem to have a similar stability towards oxidation, their electrical behavior is opposite.

4.5 Conclusions

The analysis performed in Chapter 2 suggested the possibility to take advantage of the 4-position of the peripheral phenyl rings of the rubrene molecule to introduce different chemical modifications in the molecule itself, in order to impart improved stability and solubility, while preserving the crystal packing of the orthorhombic polymorph of rubrene in the solid state. This "crystal engineering" approach proved to be correct: for all the monoclinic crystals of the synthesized derivatives, bearing both electron withdrawing and donating substituents, the introduced functionalities were confined at the surfaces of the (100) layer, without significantly affect the intermolecular contacts of the peculiar herringbone π-stacking motif. In their recently published work (76), McGarry *et al.* obtained similar results only for two additional rubrene derivatives bearing a functionalizing group in the 4-position, while for all the other synthesized derivatives, carrying substituents in a different position, the orthorhombic-like crystal packing motif was systematically lost.

Both chemical characterization of the derivatives in solution and electrical characterization of their crystals showed very different behaviors. The reactivity of the different moieties with oxygen, in particular, was not proved to be directly correlated with the oxidation potential of the material nor with the electron withdrawing strength of the substituents. Holding the perfect isomorphism among the analyzed structures, a role played by rubrene endoperoxide in the enhancement of transport properties of rubrene in the presence of oxygen is therefore to be excluded, because the oxidation process probed by the evolution of the absorption spectra is not compatible with the transport properties displayed by our derivatives. Some other oxygen-related process must be responsible for the improvement of charge carrier transport: in the case of the photoconductivity of rubrene, an interaction between rubrene molecules and interstitial molecular oxygen has already been proposed by Maliakal *et al.* (39). The authors carried out electron paramagnetic resonance (EPR) measurements, which indicated the presence in the rubrene crystals of radical cation and superoxide radical anion pairs,

during the irradiation of the samples in an oxygen atmosphere. An electron transfer process between the excited state of rubrene molecules and adjacent oxygen molecules was proposed, leading to the formation of the couple of free charge carriers, detected in their experiment after being separated by the application of the electric field. A similar process could play a role also in the case of dark conductivity and our results seems to be compatible with this theory.

5 | High-Pressure Studies

5.1 Introduction

High-pressure (HP) investigation of solids was pioneered by Bridgman in the first decades of the last century (79). As the main interest in this field was focused on basic and applied problems of physics, geology, mineralogy and materials sciences, involving metals, elements, simple molecules, ices, minerals and inorganic compounds, such studies on organic materials were rather rare. In the last decades, the number of structural studies regarding the effects of hydrostatic pressure on small-molecule organic crystals, in the range 0.1–10 GPa, began to rapidly grow, following the huge development of HP technologies that allowed to overcome the technical difficulties. The interest in this field is due the high efficiency displayed by pressure in generating phase transitions and new phases, triggering new chemical reactions, conformational and structural transformations of molecules, polymerization, phase transitions and polymorphism, as well as elucidating structure–property relationship: all these topics are, of course, of interest to chemists and physicists. For the purposes of the present work, the application of high pressure represents a powerful method for both exploring the polymorphic behaviour of molecular compounds and for modifying and tuning intermolecular interactions (80–82); HP structure elucidation by single-crystal diffraction in the diamond-anvil cell (DAC) is the selected method for a direct quantitative comparison of the effects of pressure on individual intermolecular contacts. A number of PAHs have already been investigated in this way (83–85): it was shown, for example, that compression of naphthalene to 2.1 GPa results in a density increase of ca. 18%, associated with smaller void regions and tightening of the herringbone structural motif. In addition, the HP polymorphs of pyrene and phenanthrene, obtained by means of *in-situ* HP crystallization, showed significant $\pi - \pi$ stacking interactions in contrast to the ambient-pressure forms; structural

phase transitions may also result in a change in electronic and optical properties, as in the case of fluorene (86). More in general, the response of the material to the applied pressure can provide useful experimental data for the validation of *ab initio* calculations. The polymorphic behavior of rubrene at ambient conditions makes it an ideal candidate for studying the response of intermolecular interactions to the application of high pressure and for obtaining new crystal forms under these conditions. These studies have been performed in collaboration with the Emmy Noether Reasearch Group of Dr. Francesca Fabbiani at the GZG, Abteilung Kristallographie of the Georg-August-Universität of Göttingen, in Germany.

5.1.1 HP *in-situ* Growth and Compression Studies

When the material of interest is a small molecule solid sample, as underlined by E. Boldyreva in her review (81), there are two main ways to carry out a HP study:

- HP crystallization from solutions (87): new phases are formed in a more straightforward way at low pressures and solvates formation can also be explored.
- Studies of the effect of pressure on solids immersed in hydrostatic media: phase transitions, chemical transformations and information about bulk compressibility, anisotropy of strain and changes in the conformation of the molecules in general, can be obtained in this way.

Crystals of organic molecular compounds may be obtained under HP conditions by *in-situ* crystallization: similarly to when compounds are crystallized on cooling or on evaporation, the decrease in the solubility of the material with increasing pressure can be used to trigger nucleation and crystal growth. This can be done within a DAC, by loading a solution of the compound of interest in a proper solvent, and by cycling the temperature of the polycrystalline material that is in general obtained after sealing and pressurizing the DAC: a single crystalline individual can be saved from complete dissolution and further grown by means of pressure and temperature control. An example of the process is visible in Figure 5.1, where a sequence of optical microscopy images of the crystallization experiment described in Section 5.2 is reported.

In this context, the choice of the solvent is fundamental: the maximum size of the crystal that can be obtained, and thus the quality of the subsequent data collection,

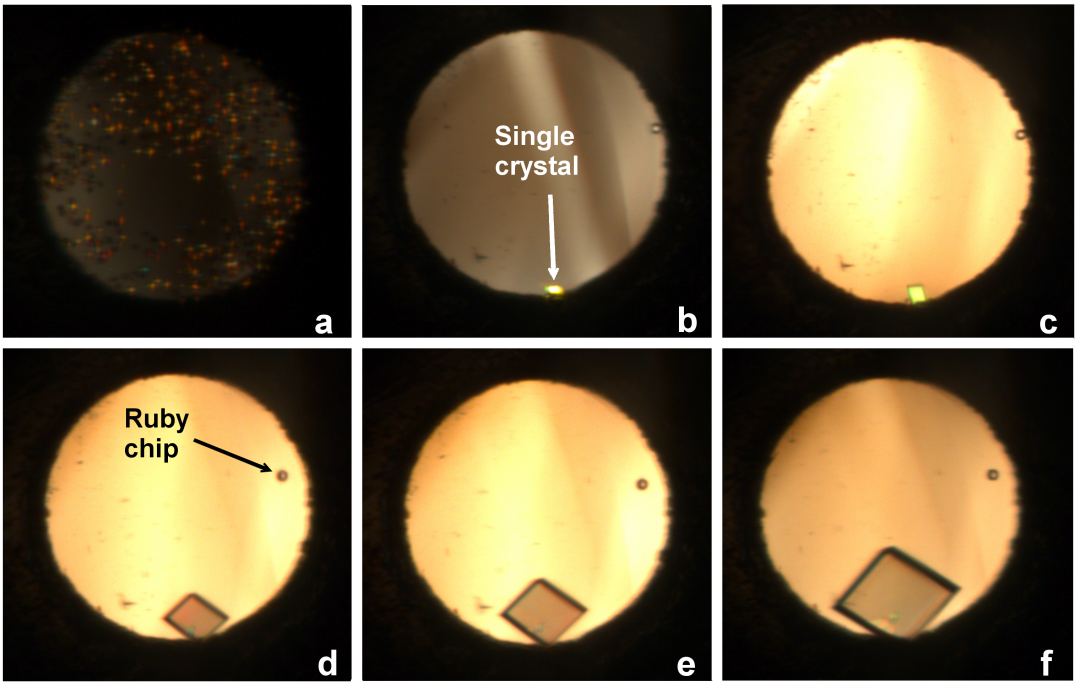

Figure 5.1: Optical microscopy images sequence of an *in-situ* HP crystallization experiment, as viewed directly through the diamonds of the DAC: precipitation of polycrystalline material (*a*), dissolution of all the crystalline individuals except one (*b*) and gradual growth of the single crystal at 0.5 GPa by cycling temperature and pressure (*c-d*).

is strongly related to the amount of material that can be dissolved in the solution to be loaded. The solubility of the compound in the chosen solvent and its temperature dependence are therefore of primary importance. At the same time, the freezing point of the solvent with respect to the applied pressure, or the value of pressure at which the hydrostaticity of the solvent is lost, must be carefully taken into account. The crystals obtained in this way may belong, in principle, to a crystalline phase different from that usually obtained at ambient conditions, as the crystals within the DAC experience HP conditions already at the nucleation stage. Within this thesis work, this technique was first tested on 9,10-diphenylanthracene (chosen as a trial parent-system of rubrene), before being applied to rubrene, as it will be discussed in Section 5.2. Alternatively, and complementarily to this kind of experiments, a direct compression study of a crystalline sample can be performed, by immersing the solid of interest in a hydrostatic pressure-transmitting medium: apart from possibly induced phase transitions, rarely occurring from single-crystal to single-crystal, this approach offers the opportunity to monitor a number of different structural parameters as a function of the applied pressure. Here again, the choice of the proper medium is extremely important: in order to achieve completely hydrostatic compression, the medium must display hydrostatic behavior throughout the pressure regime of interest, while not not dissolving or reacting with the sample being studied. The hydrostatic limit of a range of different media have been investigated by various groups: in particular, the 4:1 mixture of methanol:ethanol used within this work, has been shown to remain hydrostatic up to $\sim$ 9.8 GPa by Angel *et al.* (88). Both diphenylantracene and rubrene single crystals have been the subject of hydrostatic compression studies in the frame of this thesis work, as it will be discussed in the next Sections.

5.2 The case of 9,10-diphenylanthracene (DPA)

9,10-diphenylanthracene (DPA) is a derivative of anthracene were the two central hydrogen atoms have been substituted by two phenyl groups. The compound is an interesting example of organic semiconductor with high electron and hole mobilities, probably resulting from an effective intermolecular linking between successive layers inside the crystal, via the anthracene-backbone-phenyl-groups (89): the two phenyl groups of a

DPA molecule are, in fact, almost orthogonal to the anthracene backbone (the $\phi - \pi$ dihedral angle is *ca.* 67.8°) as depicted in Figure 5.2.

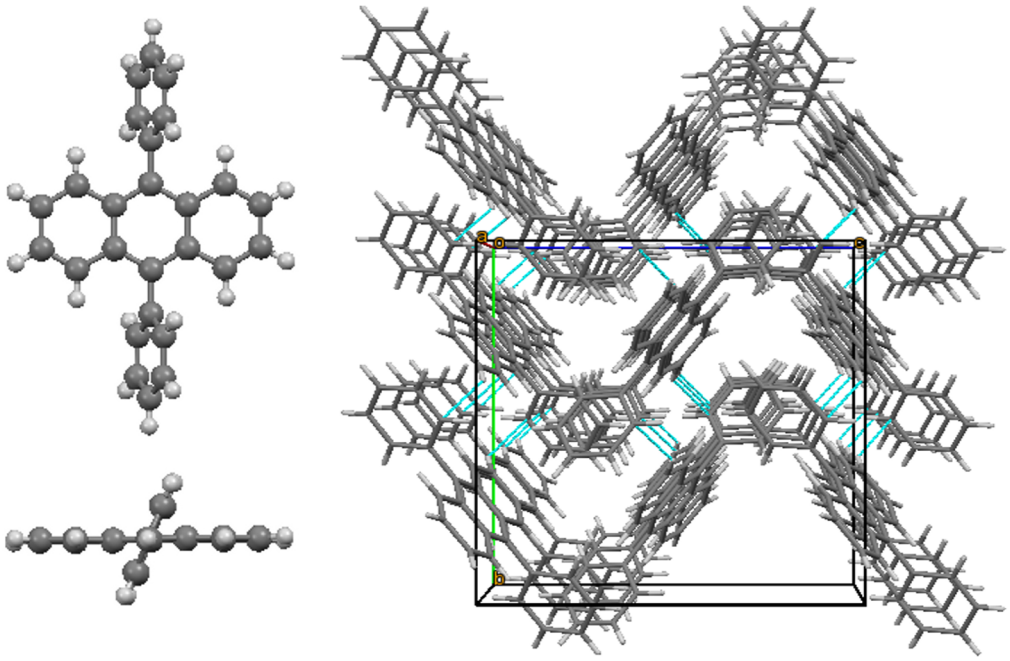

Figure 5.2: Ball-and-stick model of a DPA molecule for the structure reported in literature, view perpendicularly and along the edge of the tetracene backbone (*left*) and perspective view of its packing motif (*right*).

In the literature, only one crystalline form of the pure compound has been reported (90), although some solvated forms of the molecule are also known (91); the structural parameters of the crystal structure of DPA at room temperature (CSD Refcode: DPANTR01) are reported in the first column of Table 5.1. This compound was selected as a trial system for HP *in-situ* crystallization experiments within a DAC because of its structural similarity with the molecule of rubrene. In contrast to rubrene, the good solubility of DPA in common organic solvents and its stability towards oxidation, permit an easy manipulation of the solution throughout the whole loading process of the DAC; this allowed also the screening of an additional number of solvents, whose behavior in HP condition was not reported in the literature. Solutions of DPA in toluene, xylenes (*ortho-*, *meta-* and *para-* isomers) and dichloromethane were individually loaded in the DAC and gradually pressurized, yielding either a polycrystalline material which could

not be dissolved by increasing the temperature, or single crystalline individuals belonging to the same phase existing at ambient conditions. Loading a saturated solution of DPA in 1,1,2,2-tetrachloroethane (TCLE) and gradual pressurization to $\sim$ 0.5 GPa, resulted instead in the formation of a novel 1:1 solvate form of the compound, whose crystal structure is reported in Figure 5.3: in this new structure, the torsion angle between the two phenyl groups and the anthracene backbone ($\phi - \pi$ dihedral angle) is *ca.* 83° and the intermolecular interaction link between successive layers of DPA molecules is no longer present.

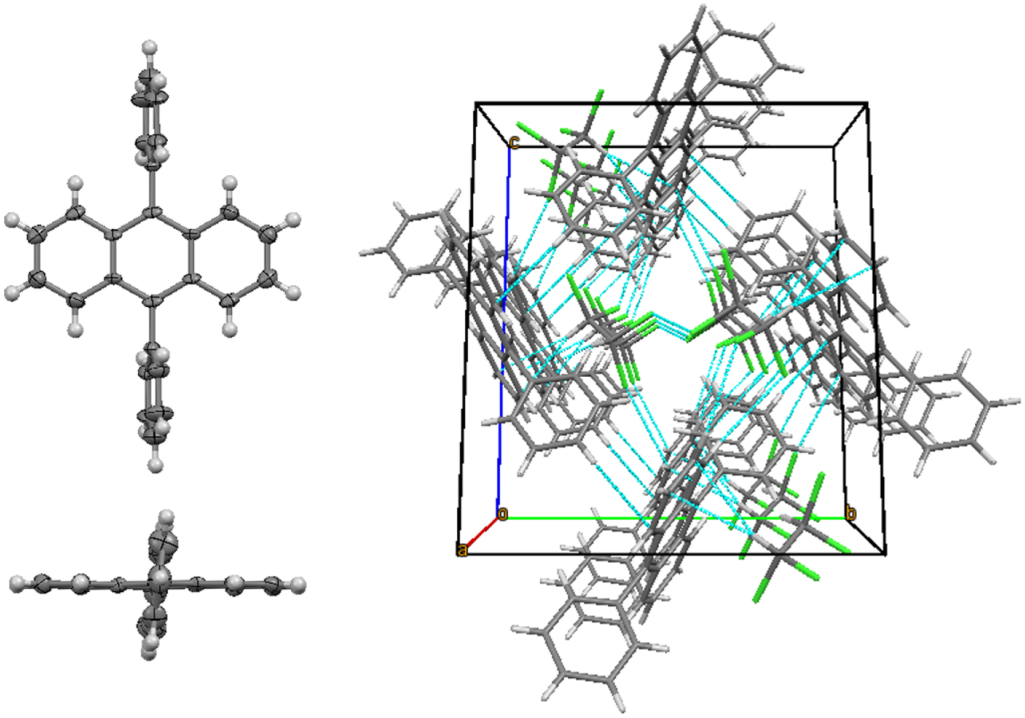

Figure 5.3: ORTEP model of a DPA molecule for the TCLE solvate structure, view perpendicularly and along the edge of the tetracene backbone (*left*) and perspective view of its packing motif (*right).*

This feature is replaced by a three dimensional network of CH$\cdots\pi$ interactions that link together *para*-hydrogens on the phenyl rings of each molecule with the external anthracene ring of an adjacent one. The result is the formation of hosting channels extending in the direction of the *a*-axis, occupied by ordered TCLE molecules. The structural parameters of this novel solvate-structure are reported in the second column

Table 5.1: Comparison between the structural parameters of the obtained structures of DPA

	DPA (DPANTR01)	DPA·TCLE	DPA 0.5 GPa	DPA 3.0 GPa
Moiety formula	$C_{26}H_{18}$	$C_{26}H_{18}{\cdot}2C_2H_2Cl_4$	$C_{26}H_{18}$	$C_{26}H_{18}$
Molecular weight	330.40	666.07	330.40	330.40
Cell setting	Monoclinic	Monoclinic	Monoclinic	Monoclinic
Space group	$C2/c$	$P2_1/c$	$C2/c$	$C2/c$
a/Å	10.683(4)	8.7874(3)	10.4695(5)	10.029(2)
b/Å	13.552(2)	12.0308(7)	13.3911(5)	13.150(2)
c/Å	12.257(2)	13.8215(8)	12.0144(6)	11.390(2)
β/ °	90.54(2)	104.964(3)	89.953(4)	88.524(18)
Volume/Å^3	1774.44	1411.65	1684.40(13)	1501.7(5)
Density/g cm^{-3}	1.237	1.567	1.303	1.461
Z/Z'	4/0.5	2/0.5	4/0.5	4/0.5
$\phi - \pi$ dihedral angle/°	67.79	82.98	65.83	62.31
$R[F^2{>}2\sigma(F^2)]$	-	0.0546	0.0399	0.0514

of Table 5.1.

In order to compare the crystal packing features of the solvate with those of the unsolvated structure of DPA, and at the same time verify the possible occurrence of a phase transition above 0.5 GPa, a sublimated single crystal of the pure compound was loaded in the DAC for a direct compression experiment. Pressure was gradually increased up to 3.0 GPa, using a 4:1 mixture of methanol:ethanol as a pressure-transmitting medium: discontinuous changes in the unit-cell parameters, suggesting a phase transition, were were not evidenced. For this reason full data collections were performed only at 0.5 and 3.0 GPa; the correspondent structural parameters of the crystal structure of DPA at HP conditions, as resulting from the experiment, are reported in the last two columns of Table 5.1. Slow-evaporation experiments have been also performed at ambient conditions on the same solution used for the *in-situ* crystallization growth. These experiments always yield crystals of the ambient phase as well as subsequent flash-cooling experiments performed directly immerging a capillary filled with the solution, in liquid nitrogen. These results suggest that the formation of the TCLE·DPA solvate is unique of HP conditions.

5.3 Rubrene Polymorphs at High Pressure

The possibility to apply to the rubrene molecule the *in-situ* HP crystallization technique is strongly limited by the intrinsic properties of the compound. It was not possible to identify any pure solvent, or any mixture of solvents, capable of dissolving an amount of rubrene compatible with the experimental requirements; it was thus not possible to obtain a concentrated enough solution, so that precipitation of polycrystalline material could be triggered by increasing the applied pressure, before the freezing point of the solution itself was reached. In addition, the extremely intense fluorescence displayed by the whole set of tested solutions, did not allow the use of the ruby fluorescence method for the measurement of the pressure. The signal of the ruby sphere was, in fact, systematically covered by the emission signal of the rubrene solution, similarly excited by the incident laser beam. The use of other pressure calibration standards, *e.g.* monitoring of the lattice constants of quartz by single-crystal XRD, was deemed unpractical and time consuming for the *in-situ* crystallisation stage. As an unreliable reading of the value of the pressure inside the DAC could have dramatic consequences on the DAC components - the worst of them being the possible failure of the diamond anvils - this strategy for the investigation of the HP behavior of rubrene was abandoned, in favor of a direct compression of rubrene single crystals of different polymorphs.

Given the profoundly different crystal packing exhibited by the monoclinic form, this polymorph was excluded from our analysis. High-pressure experiments were conducted on orthorhombic and triclinic crystals obtained by reduced pressure sublimation and by slow evaporation of a rubrene solution in 1,1,2,2-tetrachloroethane, respectively. Preliminary XRD screening of the samples revealed that all the obtained triclinic crystals were twinned. Both orthorhombic and triclinic crystals were independently transferred in the DAC equipped with 600 μm culet diamonds and a tungsten gasket, loaded with a 4:1 methanol:ethanol solution as hydrostatic medium. The pressure applied to both the samples was gradually increased up to $\sim$ 7.5 GPa at $\sim$ 1.2 GPa intervals and monitored with the ruby fluorescence method with an accuracy of 0.05 GPa; in the case of the triclinic polymorph, three different crystals were used to cover the entire pressure range, due to gasket failing at high pressure. For both polymorphs upon increasing pressure, a progressive darkening of the crystals was evident, indicating that a red shift occurs in the absorption spectrum of the material as pressure is increased, as depicted

in Figure 5.4. A gradual quenching of the fluorescence of the crystal irradiated by the

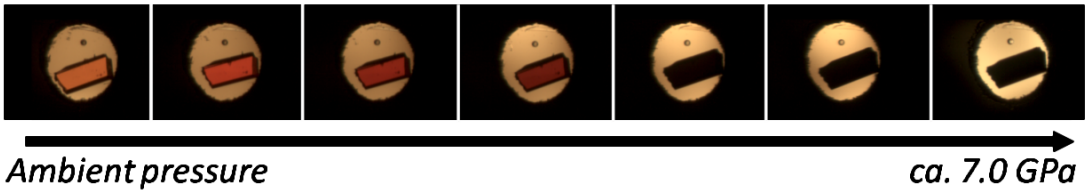

Figure 5.4: Optical microscopy images of a rubrene triclinic single crystal in the DAC, taken from ca. 0.1 to ca. 7.2 GPa at regular pressure intervals of ca. 1.2 GPa; the gradual darkening of the crystal as the pressure is increased suggest a change in the solid-state absorption spectrum of the material.

laser beam used for the pressure monitoring was also observed; the occurrence of both phenomena for rubrene under high-pressure condition was previously documented in the literature (92) and was not further investigated. Single-crystal data were collected on beamline SCD at the ANKA synchrotron radiation facility of the Karlsrhue Institute of Technology, using a wavelength of 0.66 Å. The greater brightness of synchrotron radiation together with the relatively short wavelength, at least when compared to a standard MoKα home laboratory source, enabled to obtain better quality data from the small-sized crystals selected for the experiment. The use of a small volume pressure chamber is mandatory for reaching pressures above 5 GPa.

5.3.1 Orthorhombic Rubrene

The structural data for the compression study of the orthorhombic crystal are reported in Table 5.2. No phase transition was identified in the investigated pressure range, although a strong anisotropy in the response of the material to the applied pressure is evident. As depicted in Figure 5.5, the unit cell is compressed up to almost the 75% of its original volume as a result of the reduction in the length of the cell axes, around 5% for a and b, close to 15% for the c-axis. This results in a progressive reduction of the herringbone angle and of the π-stacking distance of the tetracene cores facing each other. As a consequence, the percentage of C$\cdots$C contacts calculated by means of the Hirshfeld surface analysis gradually increases from 6.1% to 8.7%, while the percentage of C$\cdots$H contacts also increases, from 19.1% to 28.2% and the percentage of H$\cdots$H contacts decreases from 74.8% to 63.1%. The plot of the normalized distance d_{norm} on the Hirshfeld surface, the corresponding FP plot and a graphical representation of the

Table 5.2: Comparison between the structural parameters of the orthorhombic rubrene crystal throughout the compression study

	Ambient pressure (QQQCIG11)	0.15 GPa	1.20 GPa	2.41 GPa	3.51 GPa	4.79 GPa	5.83 GPa	7.50 GPa
Space group	*Cmca*	*Cmca*	*Cmca*	*Cmca*	*Cmca*	*Cmca*	*Cmca*	*Cmca*
a/Å	26.86(1)	26.903(1)	26.3195(9)	26.0382(9)	25.856(1)	25.714(2)	25.603(2)	25.491(1)
b/Å	7.193(3)	7.1895(3)	7.0464(2)	6.9599(3)	6.9005(3)	6.8447(8)	6.7946(4)	6.7389(3)
c/Å	14.433(5)	14.448(2)	13.702(2)	13.266(2)	12.959(3)	12.747(7)	12.523(4)	12.291(3)
Volume/Å^3	2788.51	2794.5(4)	2541.1(4)	2404.1(4)	2312.1(5)	2243.5(1)	2178.52(8)	2111.3(6)
Density/g cm^{-3}	1.269	1.266	1.392	1.472	1.530	1.577	1.624	1.676
herringbone angle/°	63.38	62.32(9)	59.25(5)	57.43(5)	56.36(4)	55.50(6)	54.83(6)	54.05(7)
$d_{\pi-\pi}$ stacking†/Å	3.721	3.715	3.483	3.344	3.259	3.178	3.129	3.061
$\phi - \phi'$ Torsion angle†/°	25.00	26.11	25.78	25.88	25.94	25.77	25.95	26.40
$\phi - \phi'$ Opening angle/°	25.15	24.6(4)	25.5(2)	24.9(2)	24.1(2)	23.1(2)	22.2(2)	20.6(3)
$\phi - \pi$ Dihedral angle/°	80.76	80.5(2)	77.58(9)	75.53(8)	73.99(8)	72.75(9)	71.3(1)	70.0(1)
$R[F^2 > 2\sigma(F^2)]$	-	0.0471	0.0438	0.0417	0.0456	0.0452	0.0449	0.0428

† esd are not given for the value of the parameters calculated by means of the Mercury 3.1 software.

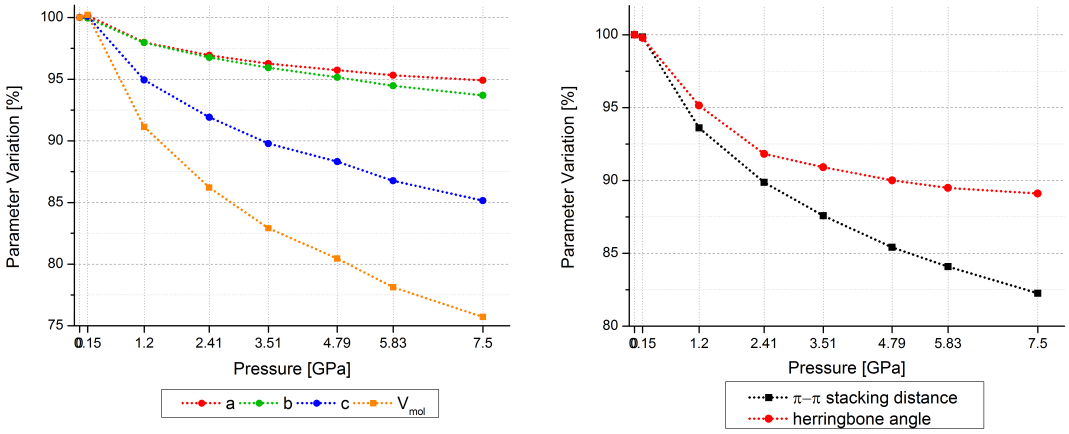

Figure 5.5: Variation of the unit-cell parameters (*left*) and of selected intermolecular parameters (*right*) of orthorhombic rubrene as a function of the applied pressure. The dotted lines are guides to the eye.

relative percentage of short-contacts for the structures obtained at every pressure point, are reported in Figure 5.6. In contrast to this, it was not possible to identify a clear trend for the changes occurring to the intramolecular parameters of the orthorhombic rubrene molecule: the width of the dihedral angle between the planes of the phenyl rings ($\phi - \phi'$ opening angle), the torsion angle among the C-C bonds connecting each of the two phenyls to the tetracene unit ($\phi - \phi'$ torsion angle), the distance among their centroids, and the width of the dihedral angle described by the phenyl plane with the tetracene plane ($\phi - \pi$ dihedral angle) were calculated by means of the same approach used for the rubrene derivatives, described in Chapter 4 and depicted in Figure 4.14. By means of the PASCal web tool for Principal Axis Strain Calculations (93), the directions of the principal axes of the strain tensor with respect to the crystallographic axes, *i.e.* the directions of the minimum, medium, and maximum compression of the structure, have also been calculated and graphically reported in Figure 5.7, together with the median principal compressibility values obtained over the whole pressure data set. For an orthorhombic system, these directions coincide with the crystallographic axes: the direction of maximum compressibility is along the *c*-axis while the minimum one is along *a*, *i.e.* along the short molecular axis of the tetracene units. The volume variation of the material as a function of pressure can be used to give an Equation of State (EoS), usually parameterized in terms of bulk modulus $B_0 = -V\partial P/\partial V$ and its pressure derivative $B' = \partial B/\partial P$. Several EoS are available for volume fits; the

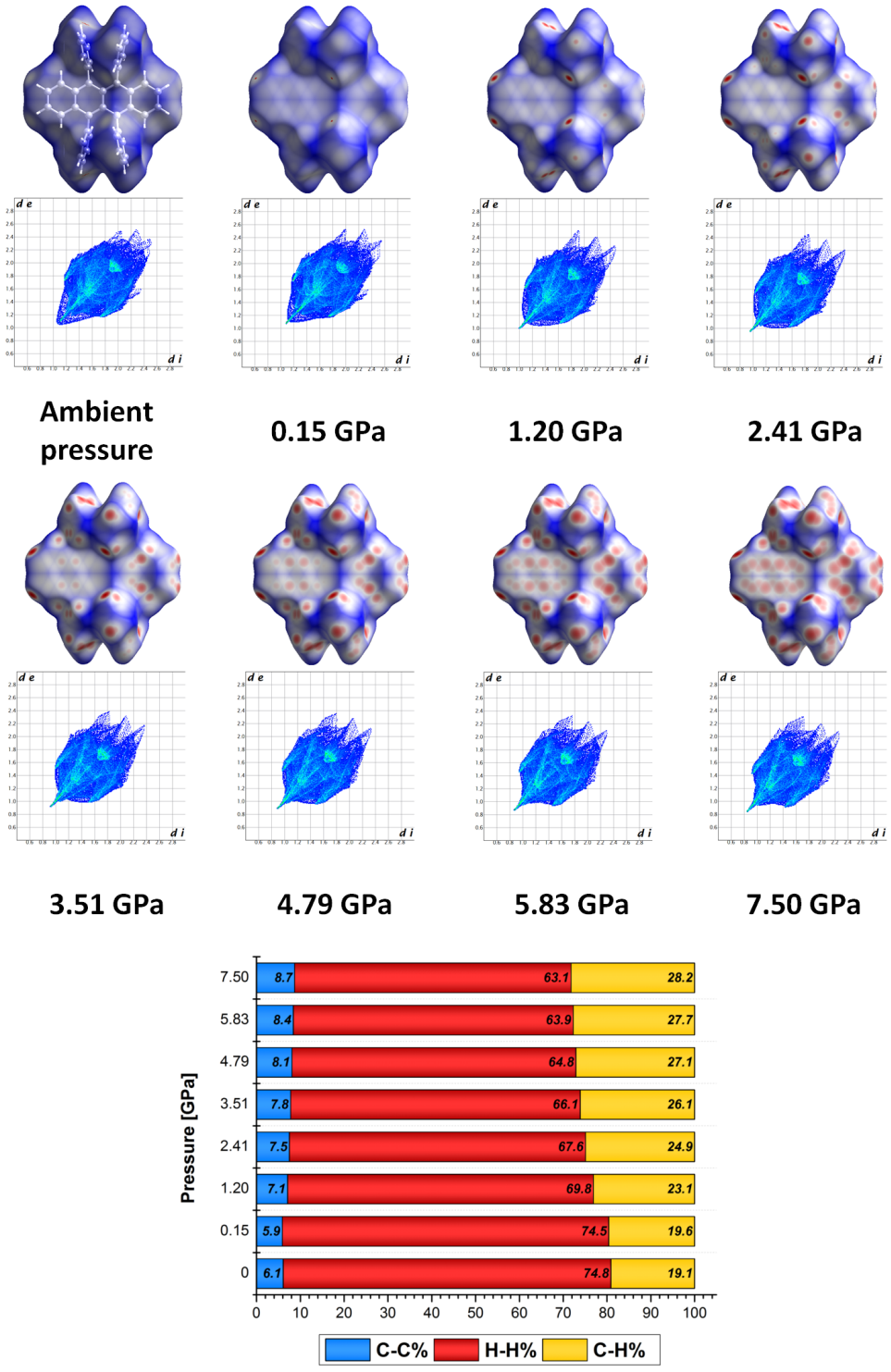

Figure 5.6: d_{norm} HS and FP for the structure of orthorhombic rubrene at every pressure step (*top*) and corresponding fingerprint breakdown into the single atom-type contributions (*bottom*).

Murnaghan-type EoS (94) has been already used to describe the behavior of molecular solids displaying a large volume reduction when subjected to compression (95, 96), and was therefore selected to determine B_0 and B', by means of a least-squares fit of the PV data using the program EoSFit v5.2 (97). The obtained values are 9.17 ± 0.43 GPa and 6.47 ± 0.29, respectively, in good agreement with those reported in literature for similar compounds (98), such as anthracene (8.4 ± 0.6 GPa and 6.3 ± 0.4), tetracene (9.0 ± 2.0 GPa and 7.9 ± 1.2) and pentacene (9.6 ± 1.0 GPa and 6.4 ± 0.5).

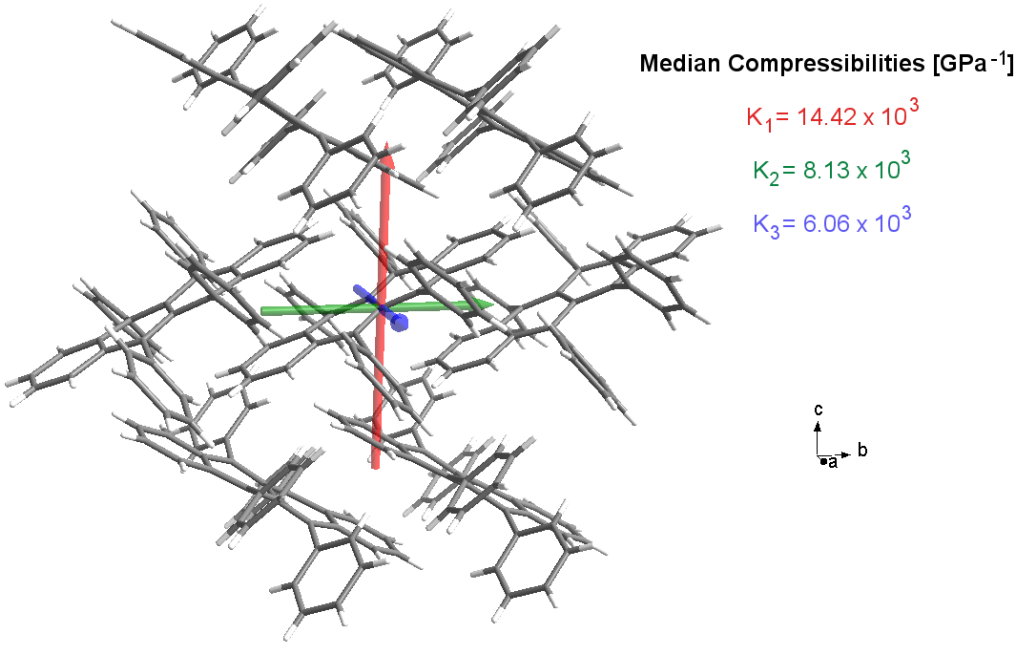

Figure 5.7: Directions of maximum (red), medium (green) and minimum (blue) compressibility and median compressibility values for orthorhombic rubrene, throughout the compression study.

5.3.2 Triclinic Rubrene

The structural data for the compression study of the triclinic crystal are reported in Table 5.3. Below $\sim$ 6.0 GPa, the effect of the applied pressure on the unit-cell parameters primarily affects the $\pi - \pi$ stacking layer of the tetracene cores, leaving almost unaltered the piling of these layers. Interaxial angles variation across the pressure range is modest: the β and γ angles are only slightly affected by the compression and α is gradually reduced by up to 6% of its original value. Similarly, whilst the length of the a and c axes are subject to very similar reductions (ca. 7.5 %), the compression of the b axis is substantially larger (ca. 11%), as depicted in Figure 5.8. As a result of compression, the volume available for each molecule is reduced by up to 21% at 5.91 GPa: this corresponds to a gradual reduction of the $\pi-$stacking distance and of the distance between the centroids of adjacent molecules. To accommodate the increasing number of intermolecular contacts involving the phenyl groups of each rubrene molecule, the molecule itself is forced to increase the torsion angle between the tetracene core and each phenyl group ($\phi - \phi'$ torsion angle), while reducing the opening angle among the two phenyl rings ($\phi - \phi'$ opening angle). This trend can be easily recognized by an-

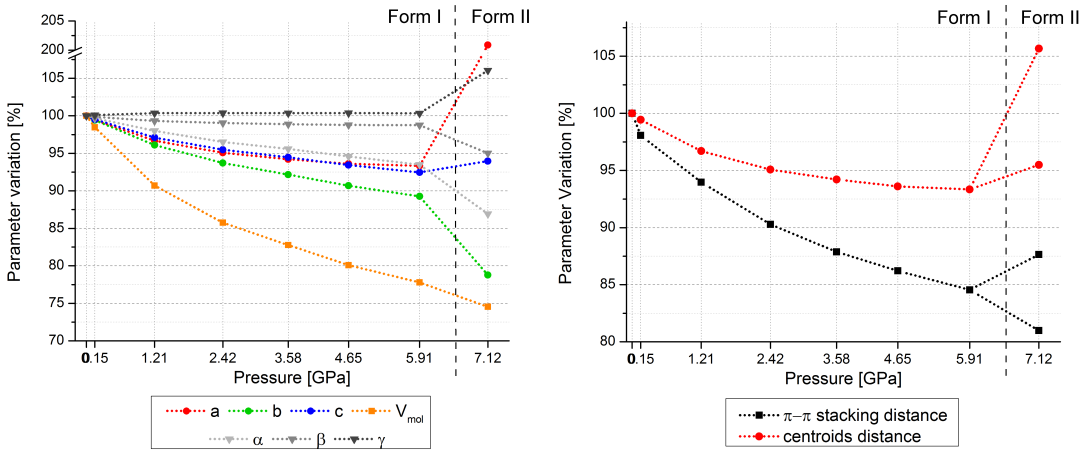

Figure 5.8: Variation of the unit-cell parameters (*left*) and of the selected intermolecular parameters (*right*) of triclinic rubrene as a function of the applied pressure. The dotted lines are guides to the eye.

alyzing the d_{norm} Hirshfeld surface and fingerprint plot at each pressure step depicted in Figure 5.9, and comparing the percentage of intermolecular contacts involving the

Table 5.3: Comparison between the structural parameters of the triclinic rubrene crystal throughout the compression study

	Form I ambient pressure	Form I 0.15 GPa	Form I 1.21 GPa	Form I 2.42 GPa	Form I 3.58 GPa	Form I 4.65 GPa	Form I 5.91 GPa
Space group	$P\bar{1}$	$P\bar{1}$	$P\bar{1}$	$P\bar{1}$	$P\bar{1}$	$P\bar{1}$	$P\bar{1}$
a/Å	7.0883(7)	7.0478(3)	6.8535(4)	6.7392(4)	6.6779(5)	6.6350(3)	6.6162(4)
b/Å	8.5994(8)	8.549(1)	8.264(1)	8.059(1)	7.926(2)	7.799(2)	7.676(2)
c/Å	12.006(1)	11.948(1)	11.657(1)	11.464(1)	11.341(2)	11.218(1)	11.100(1)
α/°	93.486(5)	93.20(1)	91.61(1)	90.27(1)	89.37(2)	88.44(2)	87.40(2)
β/°	105.642(5)	105.501(5)	104.921(5)	104.627(6)	104.460(7)	104.348(7)	104.322(7)
γ/°	95.977(5)	96.079(6)	96.311(7)	96.329(8)	96.321(9)	96.316(8)	96.289(9)
Volume/Å^3	697.9(1)	687.2(1)	633.0(1)	598.4(1)	577.6(2)	559.0(1)	542.8(1)
Z/Z'	1/0.5	1/0.5	1/0.5	1/0.5	1/0.5	1/0.5	1/0.5
Density/g cm^{-3}	1.267	1.287	1.397	1.478	1.531	1.582	1.629
$d_{\pi-\pi}$ stacking†/Å	3.788	3.736	3.557	3.421	3.326	3.263	3.195
Centroids distance†/Å	7.088	7.048	6.853	6.739	6.678	6.635	6.616
$\phi - \phi'$ Torsion angle†/°	22.66	23.46	22.67	25.11	25.30	24.46	24.01
$\phi - \phi'$ Opening angle/°	22.1(1)	20.9(4)	19.3(2)	18.5(4)	17.4(5)	16.8(3)	16.6(3)
$\phi - \pi$ Dihedral angle/°	86.77(6)	86.8(2)	86.3(1)	85.7(2)	84.7(2)	84.1(2)	82.9(2)
$\phi' - \pi$ Dihedral angle/°	84.27(6)	84.3(2)	82.6(1)	80.5(2)	78.9(3)	77.2(2)	75.4(2)
$R[F^2 > 2\sigma(F^2)]$	0.0524	0.0589	0.0431	0.0600	0.0659	0.0639	0.0561

† esd are not given for the value of the parameters calculated by means of the Mercury 3.1 software.

different atom types. A shorter $\pi-$stacking distance, together with smaller displacements of the opposing tetracene cores, give rise to a larger molecular surface involved in the $\pi-\pi$ stacking. The percentage of C$\cdots$C contacts in the crystal, hence, increases with increasing pressure; at the same time, the rearrangement of the phenyl groups reduces the amount of H$\cdots$H contacts, in favor of a larger percentage of C$\cdots$H contacts. The direction of maximum compressibility of the crystal structure have been also calculated and graphically reported in Figure 5.10, together with the median principal compressibility values obtained over the whole pressure data set up to 5.91 GPa. Since the system is triclinic, none of these directions corresponds to a crystallographic axis: the maximum compressibility occurs in a direction very close to that along which the most external aromatic rings of opposing tetracene cores face each other; the minimum compressibility occurs along a direction close to that of the tetracene backbone short molecular axis. The values for the bulk modulus B_0 and its derivative *B'*, calculated by using a Murnaghan-type EoS, are 9.54 $\pm$ 0.34 GPa and 6.47 $\pm$ 0.26, respectively, in good agreement with those calculeted for orthorhombic rubrene. On increasing pressure to 7.12 GPa a phase transition to form II clearly occurs: the rubrene molecule loses its crystallographic $P\bar{1}$ symmetry, as depicted in figure 5.11, with increasing multiple short contacts involving the aromatic core and the four phenyl groups. No change in the space group occurs during the transition but the unit-cell volume doubles. Each of the phenyl groups is forced to twist, increasing independently its torsion angle with the tetracene backbone ($\phi-\pi$ and $\phi'-\pi$ dihedral angles), which is forced to bend and lose its planarity. This bending involves the edges of the tetracene cores of the rubrene molecules, and is perfectly compatible with the direction along which the calculated maximum compressibility occurs in the lower pressure form I. Along with this, the torsion angle between the two phenyl groups, protruding from the same edge of the tetracene ($\phi-\phi'$ torsion angle), undergoes a dramatic decrease from a value close to 25° to a value which is *ca.* 9° on one side and *ca.* 1.5° on the other one. On the contrary, the opening angle for a couple of phenyl groups ($\phi-\phi'$ opening angle) on one side of the tetracene seems to survive the phase transition, while for the other couple undergoes a variation of *ca.* 10°. To accommodate these newly-shaped molecules, the unit cell also undergoes some modifications: in order to maintain a good coherence with the description of the crystal structure at ambient pressure, we describe the new unit cell with b and c axes similar to the ambient pressure cell, and a double length a axis;

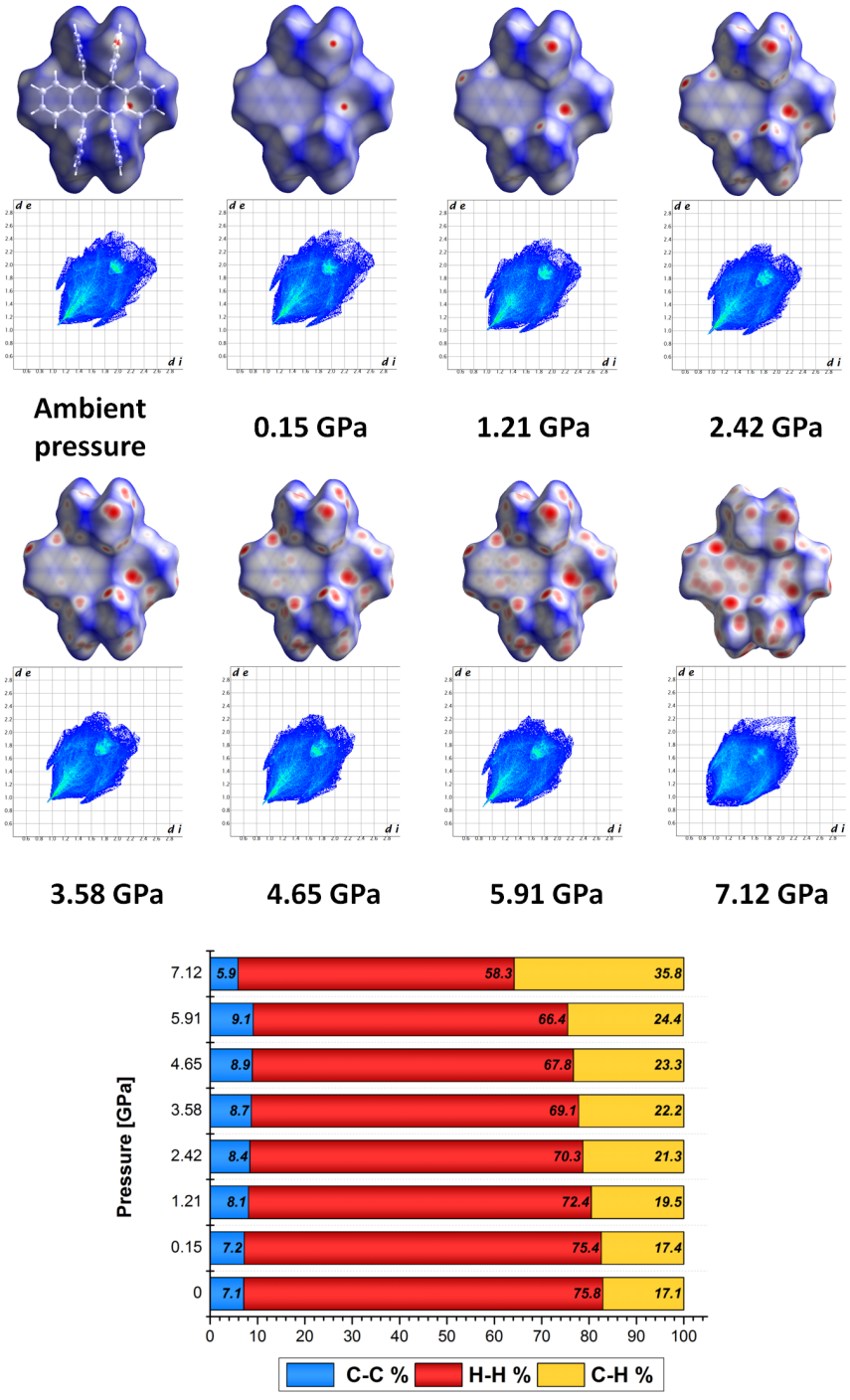

Figure 5.9: d_{norm} HS and FP for the structure of triclinic rubrene at every pressure step (*top*) and corresponding fingerprint breakdown into the single atom-type contributions (*bottom*).

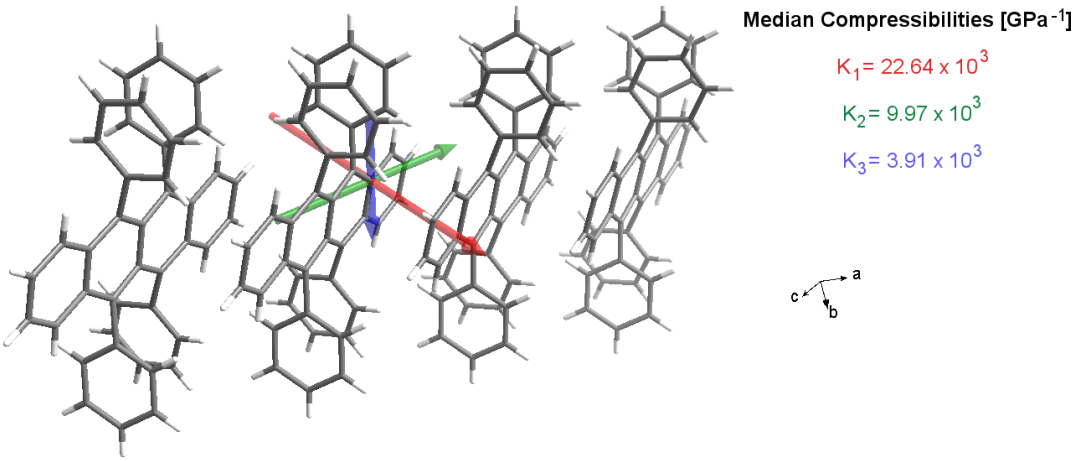

Figure 5.10: Directions of maximum (red), medium (green) and minimum (blue) compressibility and median compressibility values for triclinic rubrene-I, throughout the compression study.

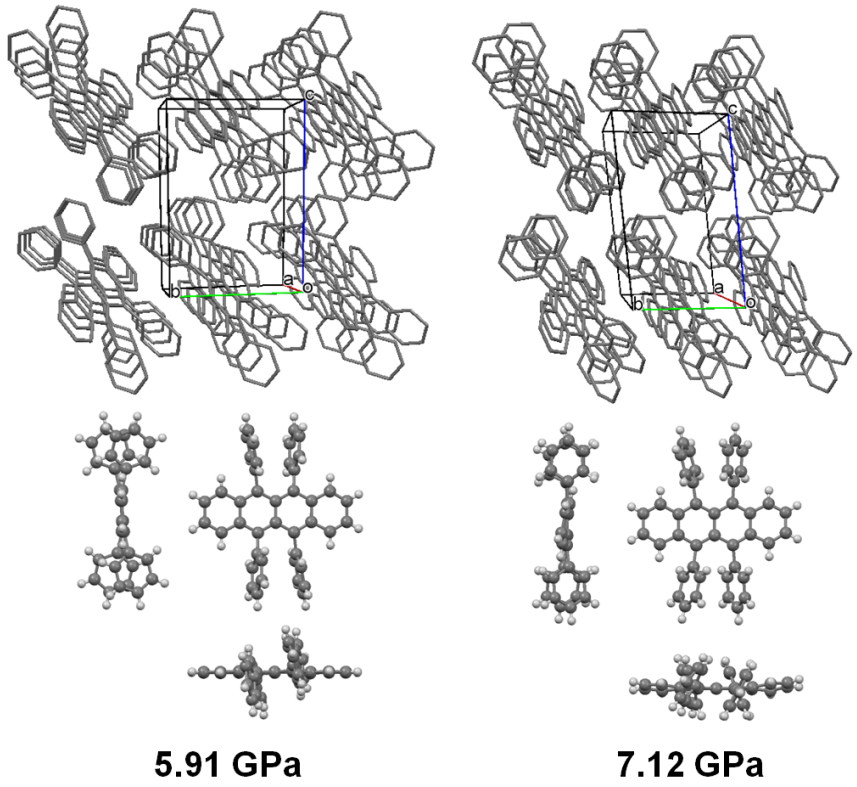

Figure 5.11: Crystal structure and ball-and-stick model of triclinic rubrene form I at 5.91 GPa (*left*) and form II at 7.12 GPa (*right*). Hydrogen atoms have been omitted from the crystal structures for clarity.

Table 5.4: Comparison between the structural parameters of triclinic rubrene forms I and II

	Form I 5.91 GPa	Form II 7.12 GPa
Space group	$P\bar{1}$	$P\bar{1}$
a/Å	6.6162(4)	14.239(2)
b/Å	7.676(2)	6.774(1)
c/Å	11.100(1)	11.281(1)
α/°	87.40(2)	81.26(1)
β/°	104.322(7)	100.38(1)
γ/°	96.289(9)	101.77(1)
Volume/Å^3	542.8(1)	1040.3(3)
V$_{mol}$/Å^3	542.8	520.1
Z/Z'	1/0.5	2/1
Density/g cm^{-3}	1.629	1.700
d$_{\pi-\pi}$ stacking†/Å	3.195	3.103 / 3.039
Centroids distance†/Å	6.616	7.372 / 6.919
$\phi - \phi'$ Torsion angle†/°	24.01	9.21 / 1.42
$\phi - \phi'$ Opening angle/°	75.4(2)	72.74(2) / 63.1(2)
$\phi - \pi$ Dihedral angle/°	82.9(2)	67.5(1) / 60.4(2)
$\phi' - \pi$ Dihedral angle/°	16.6(3)	15.4(1) / 18.3(5)
$R[F^2 > 2\sigma(F^2)]$	0.0561	0.0599

† esd are not given for the value of the parameters calculated by means of the Mercury 3.1 software.

according to our description, both α and β angles shrink, while γ angle widens. The structural parameters of the new triclinic form II are reported in Table 5.4 and compared with those of form I at 5.9 GPa. Hirshfeld surfaces analysis reveals a drastic drop of the percentage of C$\cdots$C contacts (ca. 3.2 %) and H$\cdots$H contacts (ca. 8.1%), which is balanced by an increase of C$\cdots$H contacts of ca. 11.5%: upon the phase transition, the repulsive strain caused by unfavorable super-short contacts is relieved and a new, denser structure is formed. Interestingly, the reverse phase transition to phase I could be simply triggered by decreasing the pressure down to 4.5 GPa, once again without any damage occurring to the crystal. Therefore, this is an interesting and rare example of a fully reversible single-crystal to single-crystal transition induced by pressure.

In order to obtain quantitative information on the intensity of the intermolecular

contacts among the rubrene molecules within forms I and II, and to possibly identify the driving force of the phase transition, we followed the Coulomb - London - Pauli (CLP) theoretical approach for the evaluation of intermolecular potentials inside crystals, using the CLP program package developed by A. Gavezzotti (29). This approach is based on the assumption that any intermolecular potential can be subdivided into a Coulomb-polarization term, a dispersive term (London) and a repulsion term (depending on overlap, Pauli). By means of the *PIXEL* method, intermolecular energies are calculated as a numerical integral over a large number of electron density pixels (20.000 for a typical medium-sized organic molecule), obtained from a standard molecular orbital calculation. In this way, the lattice energy of the crystal and the interaction energies between singled-out molecular pairs within the crystal can be calculated. With this aim, the final refined structures were used to calculate the molecular electron density at each pressure using the program *GAUSSIAN98* (99) with the MP2/6-31G** basis set. Lattice energies calculations employed a cluster of molecules with maximum distance from the central one of 20 Å and, within this cluster, 16 molecular pairs were isolated for being energetically the most significant as indicated by the lattice energy calculations. Between ambient pressure and 5.9 GPa, the disposition of these molecules around the central one reflects the symmetry of the rubrene molecule: as a result, two symmetric sets consisting of 8 dimers have been identified and progressively named with alphabetical letters on the basis of the contact-energy ranking at ambient pressure (See Figure 5.12 for a graphical representation of each molecular pair). The calculated contact energy and the corresponding dimer distance for every molecular pair are reported in Table 5.5 for ambient pressure (E_0 and d_0) and for all pressure steps; the variation trend in the contact-energy and in the dimer-distance are depicted in Figure 5.13, where d/d_0 and $(E\text{-}E_0)/E_0$ have been plotted in percentage for each short contact, as a function of the applied pressure.

As the phase transition mainly affects the conformation of the rubrene molecule, leaving almost unaltered the packing motif of the first-neighbors molecules of the central one, the energy and distance values of form I and form II can be directly compared. At 7.1 GPa, two different values for each dimer distance and contact energy has been plotted, accounting for the loss of symmetry of the rubrene molecule in form II, resulting in 16 independent molecular pairs, instead of the 2 sets of 8 dimers of form I: in this way, the discontinuity between 5.9 and 7.1 GPa corresponding to the phase transition

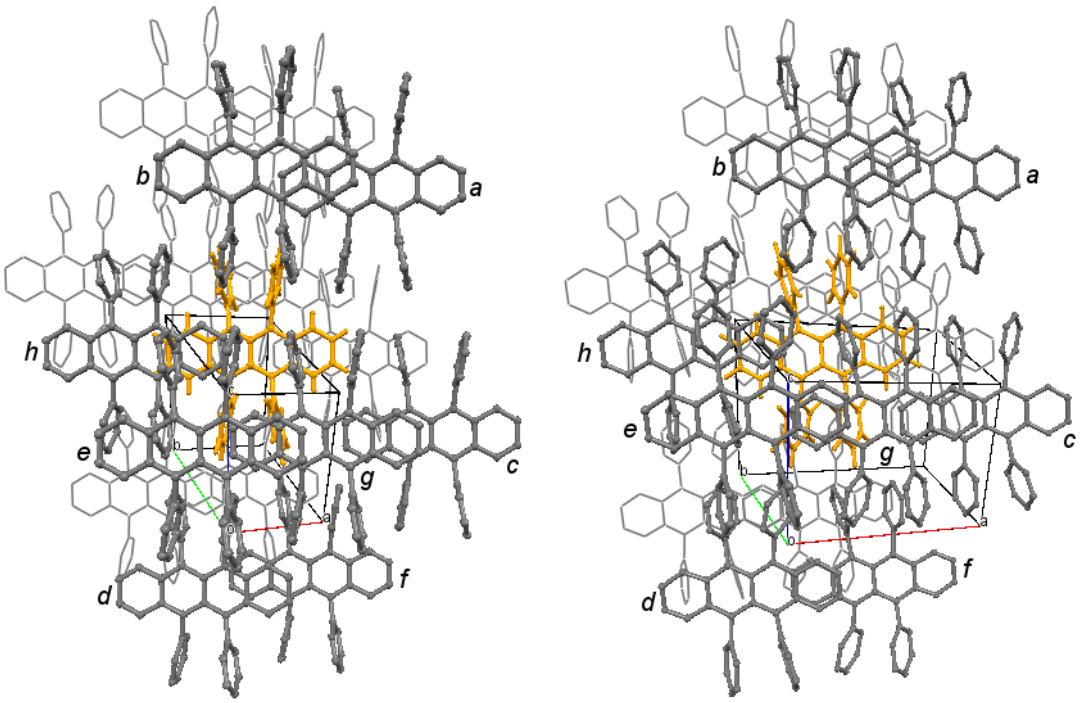

Figure 5.12: Disposition of the energetically most significant 16 molecular pairs isolated from the Pixel calculation, within the form I structure at 5.91 GPa (*left*) and the form II at 7.12 GPa(*right*), with respect to the yellow colored central molecule. Only the 8 molecules which are closer to the observer have been highlighted for clarity.

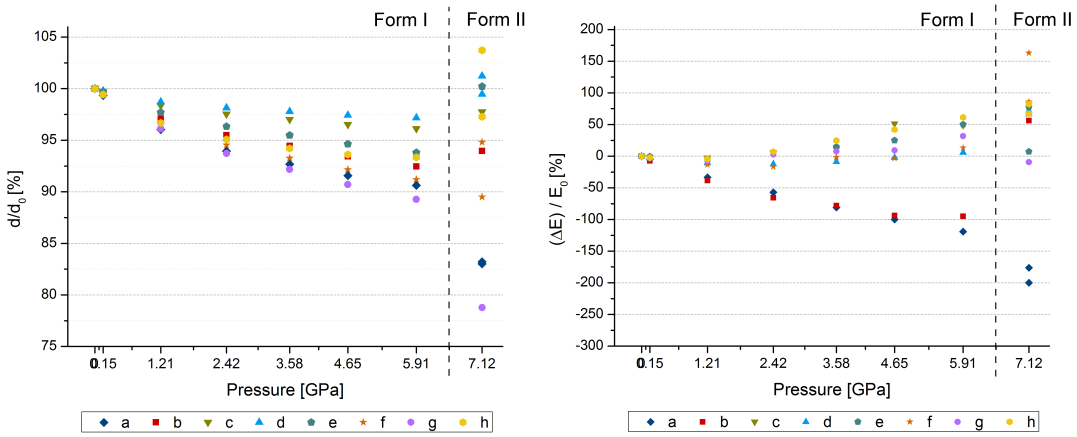

Figure 5.13: Dimer-distance variation d/d_0 (*left*) and interaction energy variation $(E\text{-}E_0)/E_0$(*right*) as a function of pressure, for the first 16 neighbors of a rubrene molecule within the triclinic crystal structure.

Table 5.5: Interaction energy (E, in kJ/mol) and dimer distance (d, in Å) for the first 16 neighbors of a rubrene molecule within the triclinic crystal structure, at different pressures (in GPa).

Contact	*a*		*b*		*c*		*d*		*e*		*f*		*g*		*h*	
d & E	d	E	d	E	d	E	d	E	d	E	d	E	d	E	d	E
Ambient pressure	10.559	-2.1	12.006	-9.6	14.336	-12.7	14.042	-19.3	12.186	-22.0	11.700	-24.1	8.599	-47.2	7.088	-63.2
0.15	10.488	-2.2	11.948	-10.3	14.299	-13.1	14.013	-19.9	12.142	-22.1	11.642	-24.4	8.549	-48.7	7.048	-64.6
1.21	10.140	-2.8	11.657	-13.3	14.099	-13.0	13.862	-21.4	11.905	-23.0	11.301	-27.3	8.264	-50.8	6.853	-66.0
2.42	9.919	-3.3	11.464	-15.9	13.982	-11.9	13.781	-21.7	11.739	-20.7	11.061	-28.1	8.059	-45.9	6.739	-58.7
3.58	9.786	-3.8	11.341	-17.1	13.908	-11.3	13.731	-21.0	11.636	-18.7	10.912	-24.5	7.926	-43.6	6.678	-47.6
4.65	9.668	-4.2	11.218	-18.6	13.836	-6.2	13.681	-19.7	11.532	-16.5	10.782	-24.9	7.799	-42.8	6.635	-36.6
5.91	9.569	-4.6	11.100	-18.7	13.779	-6.5	13.645	-18.2	11.431	-11.0	10.669	-20.9	7.676	-32.3	6.616	-24.5
7.12	8.764	-6.3	11.281	-4.2	14.013	-2.3	13.967	-6.5	12.210	-4.9	11.093	-3.4	6.774	-51.7	7.352	-11.3
	8.786	-5.8					14.213	-5.5	12.213	-20.4	10.472	15.2			6.895	-20.8

becomes even more evident. By inspecting Figure 5.13, it is clear that, apart from contact *a* and *b*, the energies for all contacts are destabilized as pressure is increased and that the rate of this destabilization is similar for certain contacts, but not related with the energy ranking at ambient pressure. The energy ranking itself is changing throughout the compression experiment (see the energy values reported in Table 5.5): at 2.4 GPa contacts ***c*** and ***e*** become more positive in energy than, respectively,***b*** and ***d***. The energy of contact ***b*** becomes also less positive than that of contact ***e*** at 4.6 GPa, and than that of contact ***d*** at 5.9 GPa, while the energy of contact ***h*** becomes more positive than that of ***g*** already at 4.6 GPa. By 7.1 GPa, the ambient pressure energy ranking has been radically altered. In addition, contacts ***a***, ***e*** and ***g*** are significantly less stabilizing after the transition: the trend for ***g*** is actually reversed, with the contact energy firstly becoming more positive as pressure increases, then sharply getting more negative. It is also interesting to note that a large variation of the dimer distance does not necessarily correspond to a huge energy variation: contacts ***a*** and ***b***, for example, undergo a clear relaxation with increasing pressure (the total energy of the interaction gradually reduces) although the relative dimer distance is rapidly decreasing. This trend seems to suggest that the phase transition takes place to relieve the repulsion of the destabilizing interactions, so that after the transition distances between the corresponding dimers are back to being longer.

As the *PIXEL* method only calculates energies of interactions between molecules and any change in the internal energy of the molecule is not taken into account, the conformational changes occurring to the rubrene molecule as a result of the applied pressure have been taken into account in terms of internal energy, as calculated from *GAUSSIAN*. The internal energies were used to calculate an adjusted total energy *(U_{adj})*, which corresponds to the total lattice energy minus the difference in internal energy of the molecule, with respect to the ambient-pressure conformation (100). U_{adj} was used to calculate the lattice enthalpy, $H = U_{adj} + PV$, where P is the applied pressure (in Pa) and V is the molar volume (in m^3). These values are reported in Table 5.6 together with the total lattice energy of each structure and the single energy components. Although the conformational change of the rubrene molecules through the phase transition is substantial - *e.g.* the bending occurring to the tetracene backbone and the anomalous asymmetric torsion of the phenyls - it can be seen that this change is not associated with a decrease in the internal energy of the molecule (total energy - U_{adj}),

Table 5.6: Lattice energy components and total energy as a function of pressure (GPa) for triclinic rubrene, along with adjusted total energy U_{adj} and enthalpy H; energies in kJ/mol.

Pressure	Coulombic	Polarization	Dispersion	Repulsion	Total energy	U_{adj}	H
Ambient	-35.2	-24.1	-268.7	123.7	-204.2	-204.2	-204.2
0.15	-40.5	-28.5	-284.6	143.9	-209.6	-198.0	-135.9
1.21	-84.7	-58.3	-379.7	299.8	-222.8	-217.9	243.4
2.42	-130.8	-94.6	-458.8	472.1	-212.1	-198.3	673.8
3.58	-172.7	-123.7	-514.2	616.9	-193.7	-160.1	1085.4
4.65	-213.8	-160.4	-570.3	768.4	-176.1	-152.2	1413.4
5.91	-269.4	-201.3	-623.9	951.0	-143.6	-105.2	1827.2
7.12	-333.0	-215.3	-685.7	1130.5	-103.5	-33.3	2197.5

as it occurs for example in the case of L-serine, where the energy associated with the conformational change is -40 kJ/mol (100). A distinctive feature of HP transitions is that a reduction of volume always occurs; the molar volume of triclinic rubrene-II (see Figure 5.8) clearly indicates that the structure of the new phase is much denser than would be expected from extrapolation of triclinic rubrene-I trend through the phase transition at 7.1 GPa. In this sense, the transition does not seem to be driven by an optimization of molecular conformation, but more likely by a reduction of the PV term which contributes to the lattice enthalpy. As depicted in Figure 5.14 the lattice enthalpy becomes more positive as pressure increases throughout the experiment for phase I, due to the increasing repulsion term contributing to U_{adj} and the PV term. The value of the lattice enthalpy for phase II seems, instead, to be slightly below the trend line of phase I, suggesting a possible discontinuity in the gradient of the plot between 5.9 and 7.1 GPa: this would be in agreement with the diminution in the PV term as a denser structure with a more efficient packing is formed. Unfortunately, the risk of gasket failure did not allow any additional measurement to be performed above 7.1 GPa and with only a single data point for phase II available, such a conclusion can not be drawn with certainty. Nonetheless, our conclusions are consistent with those drawn by Johnstone *et al.* while investigating the high-pressure polymorphism of L-serine monohydrate (101). In their work, a phase transition involving an evident change in the conformation of the molecules with no decrease of internal energy, was identified above 4.5 GPa: similar changes in the values of U_{adj} were observed and the decrease of lattice enthalpy through

the transition was similarly considered as a result of the smaller (-13 kJ/mol) PV term applying to a more efficiently packed phase-II structure.

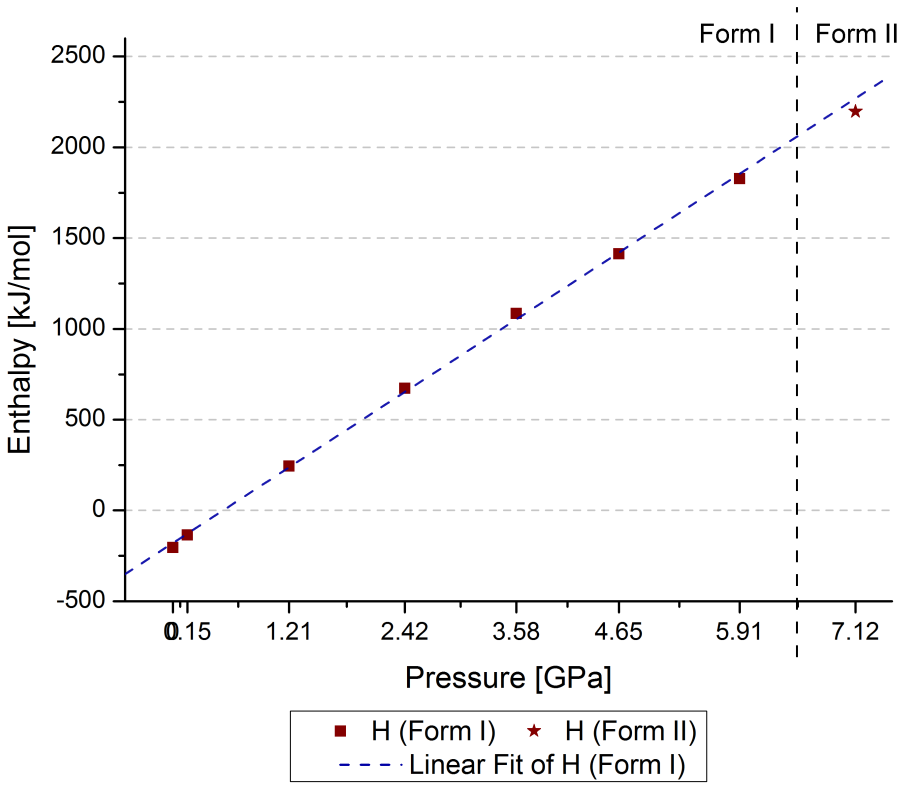

Figure 5.14: Calculated enthalpy as a function of pressure, for triclinic rubrene. The linear fit is calculated on the data points of form I only.

6 | Conclusions and Perspectives

The focus of the present thesis is the organic semiconductor rubrene, a very promising material in the field of organic electronics, due to its outstanding charge transport properties. The crystal structure of the rubrene derivatives synthesized up to now, to improve the poor solubility of the pristine molecule and its low stability towards oxidation, were analyzed; this was done in order to identify a possible synthetic strategy to obtain novel rubrene derivatives with improved chemical properties while preserving the favorable crystal packing of the molecules in the solid state. This analysis was carried out by a systematic evaluation of the Hirshfeld surface properties of the polymorphs of rubrene and of those rubrene derivatives whose structure has been deposited at the Cambridge Structural Database. As a result, the 4-position of the peripheral phenyl rings was identified as a suitable position for the introduction of different chemical modifications in the rubrene molecule, without affecting the intermolecular contacts between first neighbors in the (100) layer of orthorhombic rubrene, the layer mainly involved in the semiconduction process. Following this *crystal engineering* approach, four novel rubrene derivatives were synthesized and characterized: as a consequence of the different nature of the functionalizations introduced, these derivatives were proved to be more stable than the parent rubrene, displaying very different rates of oxidation. Crystals were grown for all derivatives and their growth conditions were optimized to obtain single-crystal samples suitable for X-ray diffraction measurements and physical characterizations; the resolution and refinement of the crystal structures revealed that the obtained monoclinic structures are isostructural with that of orthorhombic rubrene, confirming the soundness of our approach. For some of the derivatives, additional triclinic polymorphs (isostructural with triclinic rubrene) and solvate structures were also identified during the screening process and were not further characterized. The transport properties of the monoclinic crystals were probed by conductive AFM; the results

showed strong variations in the semiconducting behavior of the different derivatives. A link between the interaction with oxygen, the transport properties of these molecules and their oxidation potential seems to exist; on the contrary, a direct role of rubrene endoperoxide in the enhancement of the semiconducting properties of the material when exposed to air, seems to be excluded.

Along with this work, the high-pressure behavior of the polymorphs of rubrene was investigated: while it was not possible to grow new HP phases of rubrene by means of *in-situ* crystallization techniques, a compression study was carried out both for orthorhombic and triclinic rubrene. A different level of anisotropy in the response of the crystals to the applied hydrostatic pressure was noticed, and for the triclinic polymorph a single-crystal to single-crystal reversible phase transition was identified between 5.9 and 7.1 GPa. Structure resolution and refinement of this new form revealed that the transition involves a conformational change in the molecule, consisting in an anomalous rotation of the phenyl groups and a bending of the tetracene core. The evaluation of the intermolecular interactions among the molecules within the crystal, from the energetic point of view offered by the *PIXEL* approach, suggests the possibility that the occurring transition may be density-driven. Additional HP measurements above 7.1 GPa are necessary in order to confirm this.

This research work opens some interesting and promising perspectives: the increase in the ensemble of rubrene derivatives suitable for full physical characterization allows a deeper insight not only in the transport properties of these systems, but also regarding their optical properties and possible related applications. The elucidation of the relationship between the nature of a single specific substituent and the enhancement of the stability of the rubrene molecule could allow to tail and design additional rubrene derivatives with even more specific properties. More in detail, some work will be devoted to a wider study of 5,11-bis(3-thienyl)-6,12-biphenyltetracene, which shows transport properties comparable to those of rubrene while being more stable with respect to endoperoxide formation. A further optimization of the growth conditions of these derivatives may provide crystalline samples of larger size, allowing a full electrical characterization to be performed; the completion of the triclinic series of polymorphs of the derivatives described within this work, and their structural and physical characterization, could contribute to the final rationalization of the different semiconducting

behavior of orthorhombic and triclinic rubrene. In this sense, the analysis of the high-pressure behavior of the polymorphs of rubrene may also provide a valuable contribution, while at the same time providing useful structural information for the construction and validation of intermolecular potentials to be used for computational purposes. Crystal structure prediction or the calculation of structure-property relationships under non-ambient conditions, for example, may be positively affected by this thesis work. The improved understanding of the interplay of intermolecular interactions in the solid state will be of significance to research groups interested in either the synthetic tailoring or in the crystal engineering of new PAHs derivatives. Beneficiaries of the results of this research will also include the organic-based semiconductor industry, where the knowledge of material properties is of primary importance.

A | Appendix A

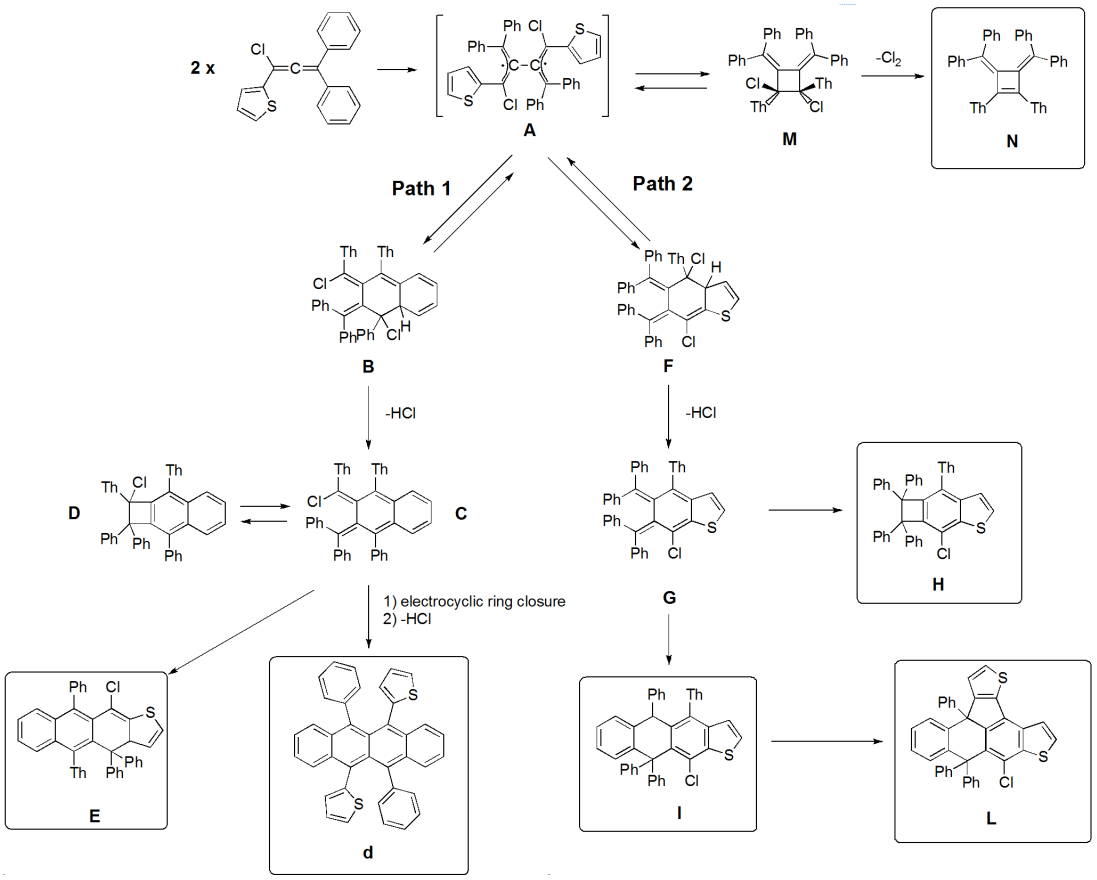

Figure A.1: Extended version of Rigaudy's mechanism accounting for the formation of compounds E, H, I, L, and N.

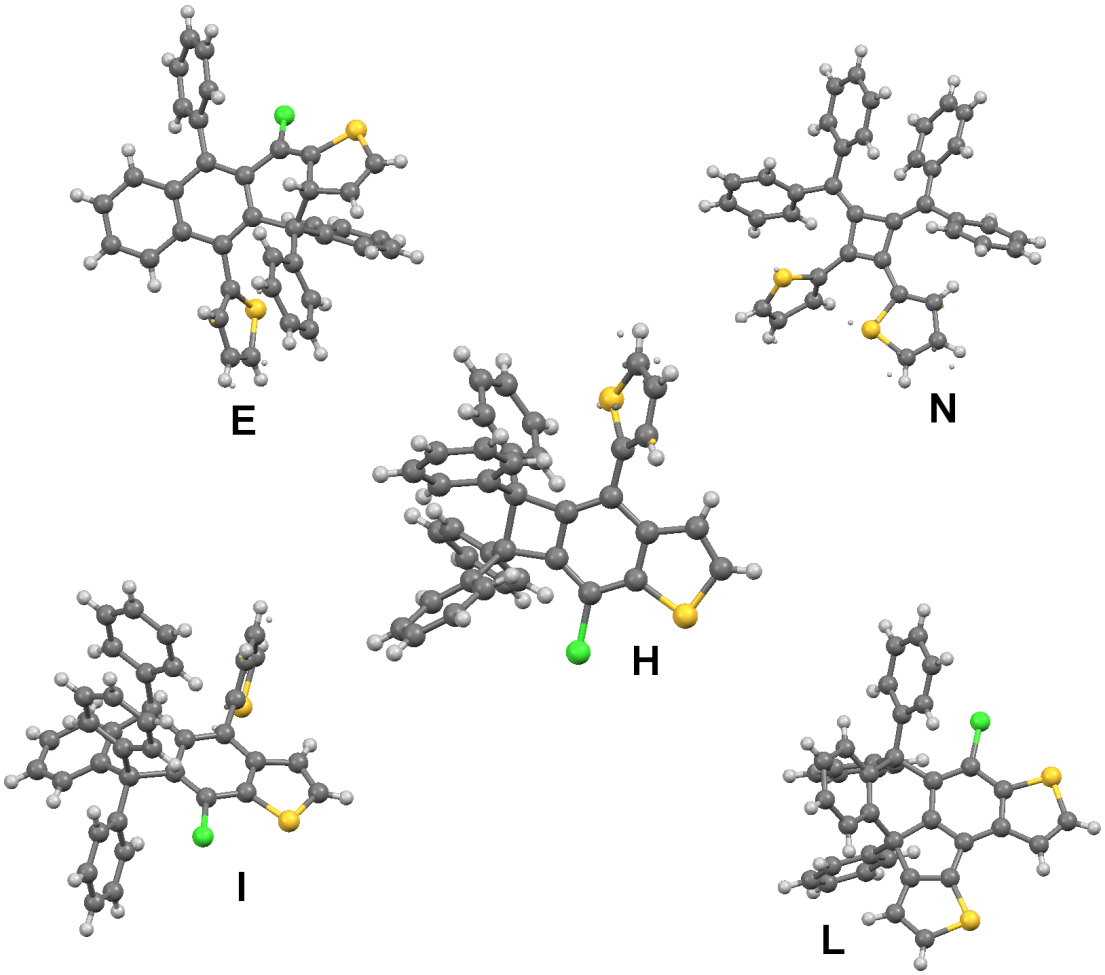

Figure A.2: Ball and stick models of the crystal structure of compounds E, H, I, L, and N, obtained as byproducts of the reaction yielding to derivative Rub-Thio.

Table A.1: Unit-cell parameters and crystal data for the byproducts of reaction yielding to derivative Rub-Thio.

	Compound E	Compound H	Compound I	Compound L	Compound N
Moiety formula	$C_{38}H_{25}ClS_2$	$C_{38}H_{25}ClS_2$	$C_{38}H_{25}ClS_2$	$C_{38}H_{23}ClS_2$	$C_{38}H_{26}ClS_2$
Molecular weight	581.19	581.19	581.19	579.17	546.73
Cell setting	Monoclinic	Triclinic	Monoclinic	Monoclinic	Monoclinic
Space group	$P2_1/c$	$P\bar{1}$	$P2_1/c$	$P2_1/c$	$P2_1$
a/Å	10.5166(2)	9.4762(2)	9.2392(2)	16.386(1)	11.5180(6)
b/Å	17.9901(4)	11.5861(4)	20.2271(3)	8.9089(6)	6.0678(3)
c/Å	15.6600(4)	13.4449(5)	15.5813(4)	19.389(1)	20.843(1)
α/°	90	82.999(9)	90	90	90
β/°	105.549(1)	79.945(8)	103.638(1)	98.168(3)	93.276(3)
γ/°	90	77.745(8)	90	90	90
Volume/Å^3	2854.3(1)	1414.8(1)	2829.8(1)	2801.8(3)	1454.3(1)
Z	4	2	4	4	2
Z'	1	1	1	1	1
Crystal color/shape	Red prism	Colorless prism	Colorless prism	Colorless prism	Yellow needle
Size/mm^3	0.40×0.40×0.24	0.25×0.20×0.10	0.40×0.22×0.12	0.40×0.20×0.18	0.40×0.10×0.08
T/K	253	203	293	253	253
$R[F^2>2\sigma(F^2)]$	0.0459	0.0737	0.0592	0.1477	0.0704

APPENDIX A

References

[1] A. Tsumura, H. Koezuka and T. Ando, "Macromolecular electronic device: Field-effect transistor with a polythiophene thin film", *Applied Physics Letters*, vol. 49, p. 1210–1212, 1986. 1

[2] G. Horowitz, D. Fichou, X. Peng, Z. Xu and F. Garnier, "A field-effect transistor based on conjugated alpha-sexithienyl", *Solid State Communications*, vol. 72, p. 381–384, 1989.

[3] F. Garnier, G. Horowitz, X. Peng and D. Fichou, "An all-organic "soft" thin film transistor with very high carrier mobility", *Advanced Materials*, vol. 2, p. 592–594, 1990. 1

[4] C. Wöll, "Physical and chemical aspects of organic electronics", *Wiley-VCH Verlag GmbH & Co KGaA*, 2009. 1

[5] J. H. Burroughes, D. D. C. Bradley, A. R. Brown, R. N. Marks, K. Mackay, R. H. Friend, P. L. Burns and A. B. Holmes, "Light-emitting diodes based on conjugated polymers", *Nature*, vol. 347, p. 539–541, 1990. 1

[6] S. Chen, L. Deng, J. Xie, L. Peng, L. Xie, Q. Fan and W. Huang, "Recent developments in top-emitting organic light-emitting diodes", *Advanced Materials*, vol. 22, p. 5227–5239, 2010.

[7] N. T. Kalyani and S. J. Dhoble, "Organic light emitting diodes: Energy saving lighting technology - a review", *Renewable and Sustainable Energy Reviews*, vol. 16, p. 2696–2723, 2012.

[8] C. W. Tang and S. A. VanSlyke, "Organic electroluminescent diodes", *Applied Physics Letters*, vol. 51, p. 913–915, 1987. 1

[9] D. A. Bernards, R. M. Owens and G. G. Malliaras, "Organic semiconductors in sensor applications", *Springer Series in Materials Science, Springer London, Limited*, vol. 107, 2008. 1

[10] C. W. Tang, "Two-layer organic photovoltaic cell", *Applied Physics Letters*, vol. 48, p. 183–185, 1986. 1

[11] C. Deibel and V. Dyakonov, "Polymer-fullerene bulk heterojunction solar cells", *Reports on Progress in Physics*, vol. 73, p. 096401, 2010.

[12] A. Mishra and P. Bäuerle, "Small molecule organic semiconductors on the move: Promises for future solar energy technology", *Angewandte Chemie International Edition*, vol. 51, p. 2020–2067, 2012. 1

[13] S. Chènais and S. Forget, "Recent advances in solid-state organic lasers", *Polymer International*, vol. 61, p. 390–406, 2012. 1

[14] J. E. Anthony, "The larger acenes: versatile organic semiconductors", *Angewandte Chemie International Edition*, vol. 46, p. 2, 2007. 2

[15] V. Podzorov, E. Menard, A. Borissov, V. Kiryukhin, J. A. Rogers and M. E. Gershenson, "Intrinsic charge transport on the surface of organic semiconductors", *Physical Review Letters*, vol. 93, p. 086602, 2004. 3

[16] M. Yamagishi, J. Takeya, Y. Tominari, Y. Nakazawa, T. Kuroda, S. Ikehata, M. Uno, T. Nishikawa and T. Kawase, "High-mobility double-gate organic single-crystal transistors with organic crystal gate insulators", *Applied Physics Letters*, vol. 90, p. 182117, 2007. 3

[17] H. Najafov, B. Lyu, I. Biaggio and V. Podzorov, "Investigating the origin of the high photoconductivity of rubrene single crystals", *Physical Review B*, vol. 77, p. 125202, 2008. 3

[18] V. Podzorov, S. E. Sysoev, E. Loginova, V. M. Pudalov and M. E. Gershenson, "Single-crystal organic field effect transistors with the hole mobility ~ 8 cm^2/Vs", *Applied Physics Letters*, vol. 83, p. 3504–3506, 2003. 3

[19] D. Käfer and G. Witte, "Growth of crystalline rubrene films with enhanced stability", *Physical Chemistry Chemical Physics*, vol. 7, p. 2850, 2005. 3

[20] S.-W. Park, J.-M. Choi, K. H. Lee, H. W. Yeom, S. Im and Y. K. Lee, "Amorphous-to-crystalline phase transformation of thin film rubrene", *The Journal of Physical Chemistry B*, vol. 114, p. 5661–5665, 2010.

[21] W. S. Hu, S. Z. Weng, Y. T. Tao, H. J. Liu and H. Y. Lee, "Oriented growth of rubrene thin films on aligned pentacene buffer layer and its anisotropic thin-film transistor characteristics", *Organic Electronics*, vol. 9, p. 385–395, 2008. 3

[22] M. Kytka, A. Gerlach, F. Schreiber and J. Kovác, "Real-time observation of oxidation and photo-oxidation of rubrene thin films by spectroscopic ellipsometry", *Applied Physics Letters*, vol. 90, p. 131911, 2007. 3

[23] E. Fumagalli, L. Raimondo, L. Silvestri, M. Moret, A. Sassella and M. Campione, "Oxidation dynamics of epitaxial rubrene ultrathin films", *Chemistry of Materials*, vol. 23, p. 3246, 2011. 3

[24] D. Braga, A. Jaafari, L. Miozzo, M. Moret, S. Rizzato, A.Papagni and A. Yassar, "The rubrenic synthesis: The delicate equilibrium between tetracene and cyclobutene", *European Journal of Organic Chemistry*, vol. 22, p. 4160, 2011. 3, 23

[25] Y. Hou, X. Chi, X. Wan and Y. Chen, "Synthesis and crystal structure of 5, 12-diphenyl-6,11-bis(thien-2-yl)tetracene", *Journal of Molecular Structure*, vol. 889, p. 265, 2008.

[26] A. S. Paraskar, A. R. Reddy, A. Patra, Y. H. Wijsboom, O. Gidron, L. Shimon, G. Leitus and M. Bendikov, "Rubrenes: Planar and twisted", *Chemistry European Journal*, vol. 14, p. 10639, 2008. 21, 23, 25, 47

[27] G. Schuck, S. Haas, A. F. Stassen, H. Kirnerc and B. Batlogg, "5,12-bis(4-tert-butylphenyl)-6,11- diphenylnaphthacene", *Acta Crystallographica E*, vol. 68, p. o2893, 2007.

[28] S. Haas, A. F. Stassen, G. Schuck, K. P. Pernstich, D. J. Gundlach and B. Batlogg, "High charge-carrier mobility and low trap density in a rubrene derivative", *Physical Review B*, vol. 76, p. 1, 2007. 3, 26, 27

[29] A. Gavezzotti, "Calculation of intermolecular interaction energies by direct numerical integration over electron densities. 2. an improved polarization model and the evaluation of dispersion and repulsion energies", *Journal of Physics Chemistry*, vol. B107, p. 2344–2353, 2003. 4, 90

[30] M. Charles, D. Charles and P. Dean, "Sur un hydrocarbure coloré: le rubrène", *Comptes Rendue*, vol. 182, p. 1440– 1443, 1926. 7

[31] E. A. Chandross, J. Longworth and R. E. Visco, "Excimer formation and emission via the annihilation of electrogenerated aromatic hydrocarbon radical cations and anions", *Journal of the American Chemical Society*, vol. 87, p. 3259–3260, 1965. 7

[32] T. Matsukawa, Y. Takahashi, T. Tokiyama, K. Sasai, Y. Murai, N. Hirota, Y. Tominari, N. Mino, M. Yoshimura, M. Abe, J. Takeya, Y. Kitaoka, Y. Mori, S. Morita and T. Sasaki, "Solution growth of rubrene single crystals using various organic solvents", *Japanese Journal of Applied Physics*, vol. 47, pp. 8950–8954, 2008. 7

[33] S. Uttiya, L. Raimondo, M. Campione, L. Miozzo, A. Yassard, M. Moret, E. Fumagalli, A. Borghesi and A. Sassella, "Stability to photo-oxidation of rubrene and fluorine-substituted rubrene", *Synthetic Metals*, vol. 161, p. 2603– 2606, 2012. 8

[34] L. Huang, Q. Liao, Q. Shi, H. Fu, J. Ma and J. Yao, "Rubrene micro-crystals from solution routes: their crystallography, morphology and optical properties", *Materials Chemistry*, vol. 20, p. 159–166, 2010. 10

[35] O. D. Jurchescu, A. Meetsma and T. T. M. Palstra, "Low-temperature structure of rubrene single crystals grown by vapor transport", *Acta Crystallographica B*, vol. 62, p. 330–334, 2006. 11

[36] K. K. Zhang, K. Tan, C. Zou, M. Wikberg, L. E. McNeil, S. G. Mhaisalkar and C. Kloc, "Control of charge mobility in single-crystal rubrene through surface chemistry", *Organic Electronics*, vol. 11, p. 1928–1934, 2010. 11, 12

[37] H. Najafov, D. Mastrogiovanni, E. Garfunkel, L. C. Feldman and V. Podzorov, "Photon-assisted oxygen diffusion and oxygen-related traps in organic semiconductors", *Advanced Materials*, vol. 23, p. 981–985, 2011. 11, 12

[38] O. Mitrofanov, D. V. Lang, C. Kloc, J. M. Wikberg, T. Siegrist, W.-Y. So, M. A. Sergent and A. P. Ramirez, "Oxygen-related band gap state in single crystal rubrene", *Physical Review Letters*, vol. 97, p. 16601, 2006. 11

[39] A. J. Maliakal, J. Y.-C. Chen, W.-Y. So, S. Jockusch, B. Kim, M. F. Ottaviani, A. Modelli, N. J. Turro, C. Nuckolls and A. P. Ramirez, "Oxygen-enhanced photoconductivity in rubrene: Electron transfer doping", *Chemistry of Materials*, vol. 21, p. 5519–5526, 2009. 11, 69

[40] D. A. da Silva Filho, E. G. Kim and J. L. Brèdas, "Transport properties in the rubrene crystal: electronic coupling and vibrational reorganization energy", *Advanced Materials*, vol. 17, p. 1072–1076, 2005. 12, 63

[41] V. Sundar, J. Zaumseil, V. Podzorov, E.Menard, R. E. Willett, T. Someya, M. E. Gershenson and J. A. Rogers, "Elastomeric transistor stamps: reversible probing of charge transport in organic crystals", *Science*, vol. 303, p. 1644–1646, 2004. 13

[42] Z. Rang, M. I. Nathan, P. P. Ruden, V. Podzorov, M. E. Gershenson, C. R. Newman and C. D. Frisbie, "Hydrostatic pressure dependence of charge carrier transport in single-crystal rubrene devices", *Applied Physics Letters*, vol. 86, p. 123501, 2005. 13

[43] T. Matsukawa, M. Yoshimura, M. Uchiyama, M. Yamagishi, A. Nakao, Y. Takahashi, J. Takeya, Y. Kitaoka, Y. Mori and T. Sasaki, "Polymorphs of rubrene crystal grown from solution", *Japanese Journal of Applied Physics*, vol. 49, p. 085502, 2010. 14

[44] A.Nangia and G. R. Desiraju, *Design of Organic Solids*, vol. 198. E.Weber and Springer-Verlag, Berlin Heidelberg Edition, 1998. 15

[45] M. A. Spackman and P. G. Byrom, "A novel definition of a molecule in a crystal", *Chemical Physics Letters*, vol. 267, p. 215–220, 1997. 16

[46] F. Hirshfeld, "Bonded-atom fragments for describing molecular charge densities", *Theoretica Chimica Acta*, vol. 44, p. 129, 1977. 16

[47] J. J. McKinnon, D. Jayatilaka and M. A. Spackman, "Towards quantitative analysis of intermolecular interactions with hirshfeld surfaces", *Chemical Communications*, vol. 37, p. 3814–3816, 2007. 17

[48] M. A. Spackman, J. J. McKinnon and A. S. Mitchell, "Novel tools for visualizing and exploring intermolecular interactions in molecular crystals", *Acta Crystallographica B*, vol. 60, p. 627–68, 2004. 18

[49] M. A. Spackman and J. J. McKinnon, "Fingerprinting intermolecular interactions in molecular crystals", *CrystEngComm*, vol. 4, p. 378, 2002. 18, 21

[50] S. K. Wolff, D. J. Grimwood, J. J. McKinnon, D. Jayatilaka and M. A. Spackman, "Crystalexplorer", vol. University of Western Australia: Crawley, Australia, 2007. 19

[51] F. H. Allen, "The cambridge structural database: a quarter of a million crystal structures and rising", *Acta Crystallographica B*, vol. 58, p. 380–388, 2002. 21

[52] C. Kloc, P. G. Simpkins, T. Siegrist and R. A. Laudise, "Physical vapor growth of centimeter-sized crystals of α-hexathiophene", *Journal of Crystal Growth 182*, vol. 182, p. 416–427, 1997. 30, 31

[53] R. A. Laudise, C. Kloc, P. G. Simpkins and T. Siegrist, "Physical vapor growth of organic semiconductors", *Journal of Crystal Growth*, vol. 187, p. 449–454, 1998. 30

[54] W. L. Bragg, "The structure of some crystals as indicated by their diffraction of x-rays", *Proceedings of the Royal Society A*, vol. 89, p. 248–277, 1913. 32

[55] A. W. Lawson and T. Y. Tang, "A diamond bomb for obtaining powder pictures at high pressures", *Review of Scientific Instruments*, vol. 21, p. 815, 1950. 34

[56] L. Merrill and W. A. Bassett, "Miniature diamond anvil pressure cell for single crystal x-ray diffraction studies", *Review of Scientific Instruments*, vol. 45, p. 290–294, 1974. 34

[57] A. Dawson, D. R. Allan, S. Parsons and M. Ruf, "Use of a ccd diffractometer in crystal structure determinations at high pressure", *Journal of Applied Crystallography*, vol. 37, pp. 410–416, 2004. 34, 37

[58] K. V. Kamenev, S. Tancharakorn, N. Robertson and A. Harrison, "Long symmetric high-pressure cell for magnetic measurements in superconducting quantum interference device magnetometer", *Review of Scientific Instruments*, vol. 77, p. 073905, 2006.

[59] C. Murli, S. M. Sharma, S. Karmakar and S. Sikka, "α-glycine under high pressures: a raman scattering study", *Physica B*, vol. 339, p. 23–30, 2003. 34

[60] S. A. Moggach, D. R. Allan, S. Parsons and J. E. Warren, "Incorporation of a new design of backing seat and anvil in a merrill–bassett diamond anvil cell", *Journal of Applied Crystallography*, vol. 41, p. 249–251, 2008. 34, 35

[61] R. Böhler and K. D. Hantsetters, "New anvil designs in diamond-cells", *High Pressure Research*, vol. 24, p. 391–396, 2004. 35

[62] R. Böhler, "New diamond cell for single-crystal x-ray diffraction", *Review of Scientific Instruments*, vol. 77, p. 115103, 2006. 35

[63] G. J. Piermarini, S. Block, J. D. Barnett and R. A. Forman, "Calibration of the pressure dependence of the r_1 ruby fluorescence line to 195 kbar", *Journal of Applied Physics*, vol. 46, p. 2774–2780, 1975. 36

[64] Bruker-AXS, "Saint, bruker-axs", *Madison, WI*, 2012. 37

[65] S. Parsons, "Shade, program for empirical absorption corrections to high pressure data", *The University of Edinburgh, UK*, 2004. 37

[66] G. M. Sheldrick, "Sadabs", *University of Göttingen, Germany*, 2012. 38

[67] G. M. Sheldrick, "Twinabs", *University of Göttingen, Germany*, 2012. 38

[68] J. Rigaudy and P. Capdevielle, "Dimerisation des polyphenyl-allenes: Chloropolyphenyl-allenes: mecanisme de la reaction "rubrenique"", *Tetrahedron*, vol. 33, p. 767–773, 1977. 41, 53

[69] R. A. Pascal, "Twisted acenes", *Chemical Reviews*, vol. 106, p. 4809–, 2006. 44

[70] J. Lu, D. M. Ho, N. J. Vogelaar, C. M. Kraml, S. Bernhard, N. Byrne, L. R. Kim, and R. A. Pascal, "Synthesis, structure and resolution of exceptionally twisted pentacenes", *Journal of the American Chemical Society*, vol. 128, p. 17043–17050, 2006. 44

[71] D. Veldman, S. C. J. Meskers and R. A. J. Janssen, "The energy of charge-transfer states in electron donor–acceptor blends: Insight into the energy losses in organic solar cells", *Advanced Functional Materials*, vol. 19, p. 1939–1948, 2009. 44

[72] K. Okumoto, H. Kanno, Y. Hamada, H. Takahashi and K. Shibata, "Organic light-emitting devices using polyacene derivatives as a hole-transporting layer", *Journal of Applied Physics*, vol. 100, p. 044507, 2006. 44

[73] G. M. Sheldrick, "A short history of shelx", *Acta Crystallographica A*, vol. 64, p. 112–122, 2008. 46

[74] C. B. Hübschle, G. M. Sheldrick and B. Dittrich, "Shelxle: a qt graphical user interface for shelxl", *Journal of Applied Crystallography*, vol. 44, p. 1281–1284, 2011. 46

[75] B. Chapman, A. Checco, R. Pindak, T. Siegrist and C. Kloc, "Dislocations and grain boundaries in semiconducting rubrene single-crystals", *Journal of Crystal Growth*, vol. 290, p. 479–484, 2006. 47

[76] K. A. McGarry, W. Xie, C. Sutton, C. Risko, Y. Wu, V. G. Young, J. Brèdas, C. D. Frisbie and C. J. Douglas, "Rubrene-based single-crystal organic semiconductors: Synthesis, electronic structure and charge-transport properties", *Chemistry of Materials*, vol. 25, p. 2254–2263, 2013. 63, 69

[77] O. Reid, K. Munechika and D. Ginger, "Space charge limited current measurements on conjugated polymer films using conductive atomic force microscopy", *NanoLetters*, vol. 8, p. 1602–1609, 2008. 66

[78] J. L. Z. Bao and J. J. Locklin, "Organic field-effect transistors", *Optical Science And Engineering Series, CRC Press*, 2007. 66

[79] P. W. Bridgman, "The physics of high pressure", *The Physics of High Pressure. London: Bell and Sons*, 1931. 71

[80] R. Miletich, D. R. Allan and W. F. Kuhs, "High-pressure single-crystal techniques", *Reviews in Mineralogy and Geochemistry*, vol. 41, p. 445–520, 2001. 71

[81] E. V. Boldyreva, "High-pressure diffraction studies of molecular organic solids: a personal view", *Acta Crystallographica A*, vol. 64, p. 218–231, 2008. 72

[82] F. P. A. Fabbiani, *High-Pressure Crystallography: From fundamental Phenomena to Technological Applications*, vol. 545. Eds. E. V. Boldyreva and P. Dera, Springer, 2010. 71

[83] F. P. A. Fabbiani, D. R. Allan, S. Parsons and C. R. Pulham, "Exploration of the high-pressure behaviour of polycyclic aromatic hydrocarbons: naphthalene, phenanthrene and pyrene", *Acta Crystallographica B*, vol. 62, p. 826–842, 2006. 71

[84] F. P. A. Fabbiani, D. R. Allan, W. I. F. David, S. A. Moggach, S. Parsons and C. R. Pulham, "High-pressure recrystallisation - a route to new polymorphs and solvates", *CrystEngComm*, vol. 6, p. 504–511, 2004.

[85] M. Oehzelt, R.Resel and A. Nakayama, "High-pressure structural properties of anthracene up to 10 gpa", *Physical Review B*, vol. 66, p. 174104, 2002. 71

[86] G. Heimel, K. Hummer, C. Ambrosch-Draxl, W. Chunwachirasiri, M. Winokur, M. Hanfland, M. Oehzelt, A. Aichholzer and R.Resel, "Phase transition and electronic properties of fluorene: A joint experimental and theoretical high-pressure study", *Physical Review B*, vol. 73, p. 024109, 2006. 72

[87] F. P. A. Fabbiani and C. R. Pulham, "High-pressure studies of pharmaceutical compounds and energetic materials", *Chemical Society Reviews*, vol. 35, p. 932–942, 2006. 72

[88] R. J. Angel, M. Bujak, J. Zhao, G. D. Gatta and S. D. Jacobsen, "Effective hydrostatic limits of pressure media for high-pressure crystallographic studies", *J Appl Crystallogr*, vol. 40, p. 26–32, 2007. 74

[89] A. Tripathi, M. Heinrich, T. Siegrist and J. Pflaum, "Growth and electronic transport in 9,10-diphenylanthracene single crystals - an organic semiconductor of high electron and hole mobility", *Advanced Materials*, vol. 19, p. 2097–2101, 2007. 74

[90] V. Langer and H. D.Becker *Zeitschrift für Kristallographie*, vol. 199, p. 313, 1992. 75

[91] Y. Imai, K. Kawaguchi, T. Sato, N. Tajima, R. Kuroda and Y. Matsubara, "Guest inclusion style of 9,10-diphenylanthracene", *Molecular Crystals and Liquid Crystals*, vol. 487, p. 153–159, 2008. 75

[92] T. T. Nakashima and H. W. Offen, "Crystal spectra of tetracene and rubrene under pressure", *Journal of Chemical Physics*, vol. 48, p. 4817–4821, 1968. 79

[93] M. Cliffe and A. Goodwin, "Pascal: a principal axis strain calculator for thermal expansion and compressibility determination", *Journal of Applied Crystallography*, vol. 45, p. 1321–1329, 2012. 81

[94] F. D. Murnaghan, "The compressibility of media under extreme pressures", *Proceedings of the National Academy of Sciences*, vol. 30, p. 244–247, 1944. 83

[95] G. Heimel, P. Puschnig, M. Oehzelt, K. Hummer, B. Koppelhuber-Bitschnau, F. Porsch, C. Ambrosch-Draxl and R. Resel, "Chain-length-dependent intermolecular packing in polyphenylenes: a high pressure study", *Journal of Physics: Condensed Matter*, vol. 15, p. 3375–3389, 2003. 83

[96] M. Oehzelt, G. Heimel, R. Resel, P. Puschnig, K. Hummer, C. Ambrosch-Draxl, K. Takemura and A. Nakayama, "High pressure x-ray study on anthracene", *Journal of Chemical Physics*, vol. 119, p. 1078–1084, 2003. 83

[97] R. J. Angel, "Eos-fit v5.2", *Department of Geological Sciences. Virginia Tech., Blacksburg, VA*, 2001. 83

[98] M. Oehzelt, A. Aichholzer, R. Resel, G. Heimel, E. Venuti and R. D. Valle, "Crystal structure of oligoacenes under high pressure", *Physical Review B*, vol. 74, p. 104103, 2006. 83

[99] M. J. Frisch, G. W. Trucks, H. B. Schlegel, G. E. Scuseria, M. A. Robb, J. R. Cheeseman, V. G. Zakrzewski, J. A. J. Montgomery, R. E. Stratmann, J. C. Burant, S. Dapprich, J. M. Millam, A. D. Daniels, K. N. Kudin, M. C. Strain, O. Farkas, J. Tomasi, V. Barone, M. Cossi, R. Cammi, B. Mennucci, C. Pomelli, C. Adamo, S. Clifford, J. Ochterski, G. A. Petersson, P. Y. Ayala, Q. Cui, K. Morokuma, D. K. Malick, A. D. Rabuck, K. Raghavachari, J. B. Foresman, J. Cioslowski, J. V. Ortiz, B. B. Stefanov, G. Liu, A. Liashenko, P. Piskorz, I. Komaromi, R. Gomperts, R. L. Martin, D. J. Fox, T. Keith, M. A. Al-Laham, C. Y. Peng, A. Nanayakkara, C. Gonzalez, M. Challacombe, P. M. W. Gill, B. G. Johnson, W. Chen, M. W. Wong, J. L. Andres, M. Head-Gordon, E. S. Replogle and A. J. A. Pople, "Gaussian 98 revision a.7", *Gaussian Inc., Pittsburgh, PA, USA.*, 1998. 90

[100] P. A. Wood, D. Francis, W. G. Marshall, S. A. Moggach, S. Parsons, E. Pidcock and A. L. Rohlde, "A study of the high-pressure polymorphs of L-serine using *ab initio* structures and pixel calculations", *CrystEngComm*, vol. 3, p. 1154–1166, 2008. 93, 94

[101] R. D. L. Johnstone, D. Francis, W. G. Marshall, A. R. Lennie, S. A. Moggach, S. Parsons, E. Pidcock and J. E. Warren, "High-pressure polymorphism in L-serine monohydrate: identification of driving forces in high pressure phase transitions and possible implications for pressure-induced protein denaturation", *CrystEngComm*, vol. 10, p. 1758–1769, 2008. 94